Enabling Technologies for Nano Air Vehicles
Final Report
Reporting Period: 8/10/2007 – 2/10/2009

Defense Advaneed Research Projeets Agency (DOD)
Defense Seienees Offiee
ARPA Order No. AI09/00

Issued by
U.S. Army Aviation and Missile Research Development and Engineering Center
Under
Grant No.: W31P4Q-07-1-0005

Submitted by: Oklahoma State University
Principal Investigator: Jamey D. Jacob
Business Address: 218 EN, Stillwater OK 74078
Phone Number: 405-744-5900
Effective Date of Grant: 8/10/2007
Grant Expiration Date: 2/10/2009

DISCLAIMER

20090511314

ABSTRACT

This project investigated several areas with the aim of improving performance and operational use of nano air vehicles (NAVs) by understanding fundamental operating principles and developing key technologies. The project developed plasma actuators for thrust and maneuvering control and examined flapping flight through the development of a high speed videogrammetry system and a gust/shear tunnel to replicate flow fields seen as the NAV scale. In the first portion of the research effort, we developed plasma actuators for use as control surfaces, stall mitigation devices and propulsive units for NAVs. Both of these concepts leverage the relevant low speed flow physics experienced at the NAV scale. A secondary objective of this project was to investigate the physics of low speed flow over various biologically inspired aerodynamic configurations, from both numerical and experimental perspectives, and use this information to develop novel yet practical concepts for NAVs. The primary focal points of biological inspiration for this project were the exploration of low speed aerodynamics – particularly separation phenomena – and the physical mechanisms used by nature to optimize performance in this flight regime, including the use of novel plasma actuators, aeroelastic behavior and its effect on gust response and alleviation, and the impact of unsteady motions (flapping) on the flow, especially for the reduction of drag and separation. This was related to the primary objectives of the proposal since plasma actuators are particularly useful as laminar separation control devices.

This report is divided into 3 parts. Parts Ia and Ib detail the investigations of jet vectoring plasma actuators and plasma micro-thrusters. Part II discusses flapping wing aerodynamics using high speed videogrammetry. Finally, Part III details the development of the gust/shear tunnel.

ORDER OF REPORT CONTENTS

FINANCIAL AND REPORTING DOCUMENTS

MATERIAL INSPECTION AND RECEIVING REPORT

The public reporting burden for this collection of information is estimated to average 30 minutes per response, including the time for reviewing instructions, searching existing data sources, gathering and maintaining the data needed, and completing and reviewing the collection of information. Send comments regarding this burden estimate or any other aspect of this collection of information, including suggestions for reducing the burden, to the Department of Defense, Executive Services and Communications Directorate (0704-0248). Respondents should be aware that notwithstanding any other provision of law, no person shall be subject to any penalty for failing to comply with a collection of information if it does not display a currently valid OMB control number.

PLEASE DO NOT RETURN YOUR COMPLETED FORM TO THE ABOVE ORGANIZATION.
SEND THIS FORM IN ACCORDANCE WITH THE INSTRUCTIONS CONTAINED IN THE DFARS, APPENDIX F-401.

1. PROCUREMENT INSTRUMENT IDENTIFICATION (CONTRACT) NO. W31P4Q-07-1-0005	ORDER NO.	6. INVOICE NO./DATE	7. PAGE 1 OF 1	8. ACCEPTANCE POINT

2. SHIPMENT NO.	3. DATE SHIPPED	4. B/L TCN	5. DISCOUNT TERMS

9. PRIME CONTRACTOR CODE OU784	10. ADMINISTERED BY CODE
Oklahoma State University Dr. JD Jacob 402 Whitehurst Stillwater, OK 74078	ONR San Diego 140 Sylvester Road Bldg 140/Room 225 San Diego, CA 92106

11. SHIPPED FROM (If other than 9) CODE FOB:	12. PAYMENT WILL BE MADE BY CODE
	DFAS Columbus Center HQ0339 DFAS-CO/West Entitlement Operations P. O. Box 182381 Columbus, OH 43218-2381

13. SHIPPED TO CODE	14. MARKED FOR CODE
US Army Aviation & Missile Command Special Contracts & Support Division AMSAM-AC-RD-RA Redstone Arsenal, AL 35898-5280	

15. ITEM NO.	16. STOCK/PART NO. DESCRIPTION (Indicate number of shipping containers - type of container - container number.)	17. QUANTITY SHIP/REC'D*	18. UNIT	19. UNIT PRICE	20. AMOUNT
	Supplies/Services Enabling Technologies for Nano Air Vehicles				

21. CONTRACT QUALITY ASSURANCE

a. ORIGIN

☐ CQA ☐ ACCEPTANCE of listed items

has been made by me or under my supervision and they conform to contract, except as noted herein or on supporting documents.

DATE _____ SIGNATURE OF AUTHORIZED GOVERNMENT REPRESENTATIVE

TYPED NAME:

TITLE:

MAILING ADDRESS:

COMMERCIAL TELEPHONE NUMBER:

b. DESTINATION

☐ CQA ☐ ACCEPTANCE of listed items has

been made by me or under my supervision and they conform to contract, except as noted herein or on supporting documents.

DATE _____ SIGNATURE OF AUTHORIZED GOVERNMENT REPRESENTATIVE

TYPED NAME:

TITLE:

MAILING ADDRESS:

COMMERCIAL TELEPHONE NUMBER:

22. RECEIVER'S USE

Quantities shown in column 17 were received in apparent good condition except as noted.

DATE RECEIVED _____ SIGNATURE OF AUTHORIZED GOVERNMENT REPRESENTATIVE

TYPED NAME:

TITLE:

MAILING ADDRESS:

COMMERCIAL TELEPHONE NUMBER:

* If quantity received by the Government is the same as quantity shipped, indicate by (X) mark; if different, enter actual quantity received below quantity shipped and encircle.

23. CONTRACTOR USE ONLY

DD FORM 250, AUG 2000   PREVIOUS EDITION IS OBSOLETE.

FINANCIAL STATUS REPORT

(Short Form)

(Follow instructions on the back)

1. Federal Agency and Organizational Element to Which Report Is Submitted Office of Naval Research	2. Federal Grant or Other Identifying Number Assigned By Federal Agency W31P4Q0710005		OMB Approval No. 0348-0038	Page of 1 1 pages

3. Recipient Organization (Name and complete address, including ZIP code)

Oklahoma State University, 401 Whitehurst, Stillwater, OK 74078

4. Employer Identification Number 1-736017987-E2	5. Recipient Account Number or Identifying Number AA-5-20228	6. Final Report ☑ Yes ☐ No	7. Basis ☑ Cash ☐ Accrual

8. Funding/Grant Period (See Instructions)		9. Period Covered by this Report	
From: (Month, Day, Year) 8/10/2007	To: (Month, Day, Year) 2/10/2007	From: (Month, Day, Year) 8/10/2007	To: (Month, Day, Year) 2/10/2009

10. Transactions:	I Previously Reported	II This Period	III Cumulative
a. Total outlays	0.00	202,499.00	202,499.00
b. Recipient share of outlays		0.00	0.00
c. Federal share of outlays	0.00	202,499.00	202,499.00
d. Total unliquidated obligations			0.00
e. Recipient share of unliquidated obligations			0.00
f. Federal share of unliquidated obligations			0.00
g. Total Federal share (Sum of lines c and f)			202,499.00
h. Total Federal funds authorized for this funding period			202,499.00
i. Unobligated balance of Federal funds (Line h minus line g)			0.00

11. Indirect Expense	e. Type of Rate (Place "X" in appropriate box) ☐ Provisional ☑ Predetermined ☐ Final ☐ Fixed			
	b. Rate 47.7%	c. Base 96404.94	d. Total Amount 45,842.06	e. Federal Share 45,842.06

12. Remarks: Attach any explanations deemed necessary or information required by Federal sponsoring agency in compliance with governing legislation.

13. Certification: I certify to the best of my knowledge and belief that this report is correct and complete and that all outlays and unliquidated obligations are for the purposes set forth in the award documents.

Typed or Printed Name and Title Donna Byram, Grant Accountant	Telephone (Area code, number and extension) 405-744-8242
Signature of Authorized Certifying Official *Donna Byram*	Date Report Submitted May 6, 2009

REQUEST FOR ADVANCE OR REIMBURSEMENT *(See instructions on back)*	OMB APPROVAL NO. 0348-0004		PAGE 1	OF 2 PAGES

REQUEST FOR ADVANCE OR REIMBURSEMENT	1. TYPE OF PAYMENT REQUESTED	a. "X" one or both boxes ☐ ADVANCE ☑ REIMBURSE-MENT b. "X" the applicable box ☑ FINAL ☐ PARTIAL	2 BASIS OF REQUEST ☑ CASH ☐ ACCRUAL

3. FEDERAL SPONSORING AGENCY AND ORGANIZATIONAL ELEMENT TO WHICH THIS REPORT IS SUBMITTED Office of Naval Research	4. FEDERAL GRANT OR OTHER IDENTIFYING NUMBER ASSIGNED BY FEDERAL AGENCY W31P4Q0710005	5. PARTIAL PAYMENT REQUEST NUMBER FOR THIS REQUEST 010

6. EMPLOYER IDENTIFICATION NUMBER 1-736017987-E2	7. RECIPIENT'S ACCOUNT NUMBER OR IDENTIFYING NUMBER AA-5-20228	8. PERIOD COVERED BY THIS REQUEST	
		FROM *(month, day, year)* 12/01/2008	TO *(month, day, year)* 02/10/2009

9. RECIPIENT ORGANIZATION *Name:* Oklahoma State University *Number end Street:* 401 Whitehurst *City, State and ZIP Code:* Stillwater, OK 74078	10. PAYEE *(Where check is to be sent if different than item 9)* *Name:* Oklahoma State University *Number end Street:* P. O. Box 645 *City, State and ZIP Code:* Stillwater, OK 74076

11. COMPUTATION OF AMOUNT OF REIMBURSEMENTS/ADVANCES REQUESTED

PROGRAMS/FUNCTIONS/ACTIVITIES ►	(a)	(b)	(c)	TOTAL
a. Total program outlays to date *(As of date)*	$ 202,499.00	$	$	$ 202,499.00
b. *Less:* Cumulative program income				0.00
c. Net program outlays *(Line a minus line b)*	202,499.00	0.00	0.00	202,499.00
d. Estimated net cash outlays for advance period				0.00
e. Total *(Sum of lines c & d)*	202,499.00	0.00	0.00	202,499.00
f. Non-Federal share of amount on line e	0.00			0.00
g. Federal share of amount on line e	202,499.00			202,499.00
h. Federal payments previously requested	202,499.00			202,499.00
i. Federal share now requested *(Line g minus line h)*	0.00	0.00	0.00	0.00
j. Advances required by month, when requested by Federal grantor agency for use in making prescheduled advances — 1st month	0.00			0.00
2nd month				0.00
3rd month				0.00

12. ALTERNATE COMPUTATION FOR ADVANCES ONLY

a. Estimated Federal cash outlays that will be made during period covered by the advance	$
b. *Less:* Estimated balance of Federal cash on hand as of beginning of advance period	
c. Amount requested *(Line a minus line b)*	$ 0.00

AUTHORIZED FOR LOCAL REPRODUCTION   *(Continued on Reverse)*   STANDARD FORM 270 (Rev. 7-97)
Prescribed by OMB Circulars A-102 and A-110

13.	**CERTIFICATION**		
I certify that to the best of my knowledge and belief the data on the reverse are correct and that all outlays were made in accordance with the grant conditions or other agreement and that payment is due and has not been previously requested.	SIGNATURE OR AUTHORIZED CERTIFYING OFFICIAL *Donna Byram*		DATE REQUEST SUBMITTED May 6, 2009
	TYPEO OR PRINTEO NAME AND TITLE Donna Byram Grant Accountant		TELEPHONE (AREA CODE, NUMBER, EXTENSION) 405-744-8242

This space for agency use

Public reporting burden for this collection of information is estimated to average 60 minutes per response, including time for reviewing instructions, searching existing data sources, gathering and maintaining the data needed, and completing and reviewing the collection of information. Send comments regarding the burden estimate or any other aspect of this collection of information, including suggestions for reducing this burden, to the Office of Management and Budget, Paperwork Reduction Project (0348-0004), Washington, DC 20503.

PLEASE DO NOT RETURN YOUR COMPLETED FORM TO THE OFFICE OF MANAGEMENT AND BUDGET. SEND IT TO THE ADDRESS PROVIDED BY THE SPONSORING AGENCY.

INSTRUCTIONS

Please type or print legibly. Items 1, 3, 5, 9, 10, 11e, 11f, 11g, 11I, 12 and 13 are self-explanatory; specific instructions for other items are as follows:

Item	Entry

2 Indicate whether request is prepared on cash or accrued expenditure basis. All requests for advances shall be prepared on a cash basis.

4 Enter the Federal grant number, or other identifying number assigned by the Federal sponsoring agency. If the advance or reimbursement is for more than one grant or other agreement, insert N/A; then, show the aggregate amounts. On a separate sheet, list each grant or agreement number and the Federal share of outlays made against the grant or agreement.

6 Enter the employer identification number assigned by the U.S. Internal Revenue Service, or the FICE (Institution) code if requested by the Federal agency.

7 This space is reserved for an account number or other identifying number that may be assigned by the recipient.

8 Enter the month, day, and year for the beginning and ending of the period covered in this request. If the request is for an advance or for both an advance and reimbursement, show the period that the advance will cover. If the request is for reimbursement, show the period for which the reimbursement is requested.

Note: The Federal sponsoring agencies have the option of requiring recipients to complete items 11 or 12, but not both. Item 12 should be used when only a minimum amount of information is needed to make an advance and outlay information contained in item 11 can be obtained in a timely manner from other reports.

11 The purpose of the vertical columns (a), (b), and (c) is to provide space for separate cost breakdowns when a project has been planned and budgeted by program, function, or

activity. If additional columns are needed, use as many additional forms as needed and indicate page number in space provided in upper right; however, the summary totals of all programs, functions, or activities should be shown in the "total" column on the first page.

11a Enter in "as of date," the month, day, and year of the ending of the accounting period to which this amount applies. Enter program outlays to date (net of refunds, rebates, and discounts), in the appropriate columns. For requests prepared on a cash basis, outlays are the sum of actual cash disbursements for goods and services, the amount of indirect expenses charged, the value of in-kind contributions applied, and the amount of cash advances and payments made to subcontractors end subrecipients. For requests prepared on an accrued expenditure basis, outlays are the sum of the actual cash disbursements, the amount of indirect expenses incurred, and the net increase (or decrease) in the amounts owed by the recipient for goods and other property received and for services performed by employees, contracts, subgrantees and other payees.

11b Enter the cumulative cash income received to date, if requests are prepared on a cash basis. For requests prepared on an accrued expenditure basis, enter the cumulative income earned to date. Under either basis, enter only the amount applicable to program income that was required to be used for the project or program by the terms of the grant or other agreement.

11d Only when making requests for advance payments, enter the total estimated amount of cash outlays that will be made during the period covered by the advance.

13 Complete the certification before submitting this request.

STANDARD FORM 270 (Rev. 7-97) Back

REPORT OF INVENTIONS AND SUBCONTRACTS
(Pursuant to "Patent Rights" Contract Clause) (See Instructions on Reverse Side.)

Public reporting for this collection of information is estimated to average 1 hour per response, including the time for reviewing instructions, searching existing data sources, gathering and maintaining the data needed and completing and reviewing the collection of information. Send Comments regarding this burden estimate or any other aspect of the collection of information, including suggestions for reducing this burden to Washington Headquarters Services, Directorate for Information Operations and Reports, 1215 Jefferson Davis Highway, suite 1204, Arlington, VA 22203-4302, and to the Office of Management and Budget Paperwork Reduction Project (9000-0095), Washington, DC 20503.

PLEASE DO NOT RETURN YOUR COMPLETED FORM TO EITHER OF THESE ADDRESSES. RETURN COMPLETED FORM TO THE CONTRACTING OFFICER.

1a. NAME OF CONTRACTOR/SUBCONTRACTOR	1c. CONTRACT NUMBER	2a. NAME OF GOVERNMENT PRIME CONTRACTOR	2c. CONTRACT NUMBER	3. TYPE OF REPORT (X one)	
Oklahoma State University	W31P4Q-07-1-0005	US Army Aviation & Missile Command	W31P4Q-07-1-0005	a. INTERIM	b. FINAL X
1b. ADDRESS (Include ZIP Code)	1d. AWARD DATE (YYMMDD)	2b. ADDRESS (Include ZIP Code)	2d. AWARD DATE (YYMMDD)	4. REPORTING PERIOD (YYMMDD)	
401 Whitehurst	9/14/2007		9/14/2007	a. FROM	8/10/2007
Stillwater, OK 74078-1031	AA-5-20228		AA-5-20228	b. TO	2/10/2008

SECTION I - SUBJECT INVENTIONS

5. "SUBJECT INVENTIONS" REQUIRED TO BE REPORTED BY CONTRACTOR/SUBCONTRACTOR (If "None," so state)

a. NAME(S) OF INVENTOR(S) (Last, First, MI)	b. TITLE OF INVENTION(S)	c. DISCLOSURE NO. PATENT APPLICATION SERIAL NO. OR PATENT NO.	d. ELECTION TO FILE PATENT APPLICATIONS			CONFIRMATORY INSTRUMENT OR ASSIGNMENT FORWARDED TO CONTRACTING OFFICER	
			(1) United States		(2) Foreign	e. (1) Yes	(2) No
			(a) Yes	(b) No	(a) Yes	(b) No	

None

f. EMPLOYER OF INVENTOR(S) NOT EMPLOYED BY CONTRACTOR/SUBCONTRACTOR

(1)(a) Name of Inventor (Last, First, MI)	(2)(a) Name of Inventor (Last, First, MI)
(b) Name of Employer	(b) Name of Employer
(c) Address of Employer (Include ZIP Code)	(c) Address of Employer (Include ZIP Code)

g. ELECTED FOREIGN COUNTRIES IN WHICH A PATENT APPLICATION WILL BE FILED

(1) Title of Invention	(2) Foreign Countries of Patent Application

SECTION II - SUBCONTRACTS (Containing a "Patent Rights" clause)

6. SUBCONTRACTS AWARDED BY CONTRACTOR/SUBCONTRACTOR (If "None," so state)

a. NAME OF SUBCONTRACTOR(S)	b. ADDRESS (Include ZIP Code)	c. SUBCONTRACT NUMBERS	d. DFAR "PATENT RIGHTS"		e. DESCRIPTION OF WORK TO BE PERFORMED UNDER SUBCONTRACT(S)	f. SUBCONTRACT DATES (YYMMDD)	
			(a) Clause Number	(b) Date (YYMMDD)		(1) Award	(2) Estimated Completion

SECTION III - CERTIFICATION

7. CERTIFICATION OF REPORT BY CONTRACTOR/SUBCONTRACTOR (Not required if   Small Business or   X   Non-Profit organization.) (X appropriate box).

c. I certify that the reporting party has procedures for prompt identification and timely disclosure of "Subject Inventions," that such procedures have been followed and that all "Subject Inventions" have been reported.

a. NAME OF AUTHORIZED CONTRACTOR/SUBCONTRACTOR OFFICIAL (Last, First, MI)	b. TITLE	d. SIGNATURE	e. DATE SIGNED
McKeever, Stephen W.S.	Vice President for Research & Technology Transfer	*[signature]*	

PI SIGNATURE _____ DATE 5/7/09
JD Jacob

DD From 882

Part Ia

Development of Jet Vectoring Plasma Actuators

I. Goals

The goal of this portion of the project is to investigate the use of thrust vectoring flow control using plasma actuators for nano air vehicles. Aerodynamic flow control is vitally important, particularly at low Re and high angles of attack, where separation over airfoils causes a significant increase in drag and decrease in lift. Flow control may reduce separation, thus changes in lift and drag can be minimized while aerodynamic noise produced by the aircraft and the engines can also be reduced. Popular applications consist of laminar separation control with leading edge devices, dynamic stall or separation control of low-pressure turbine blades arising from operation at low Re. Similarly, for μavs and $n$avs, the range of Re is very small and the relevant physics are hard to predict. Thus, flow control is important in terms of the fact that it improves the aerodynamic performance and enhances the flight envelope of these vehicles. Most flow control is achieved by modifying the boundary layer with devices such as vortex generator jets, synthetic jets and plasma actuators, the latter to be addressed in detail herein.

Plasma actuators are zero-net mass flux (ZNMF) devices that use atmospheric pressure electrical discharges, a class which includes corona discharges, dielectric barrier discharges (DBDs), glow discharges and arc discharges. Single DBD plasma actuators typically consist of an arrangement of two horizontally offset electrodes separated by dielectric material. Under input of a high voltage, high frequency AC or pulsed DC signal, a region of dielectric barrier discharge plasma is created in the interfacial air gap that generates a body force on the surrounding air. This results in the formation of a wall jet within the near wall boundary layer that can be used in applications such as separation control in low Re flows through the generation of near-wall momentum and turbulence.[1-7] The geometric arrangement of the actuators determines the type of the jet while the induced body force or the intensity of the jet is dependent upon the input power, dielectric material, dielectric thickness, the separation distance between the electrodes and the electrode thickness.

Plasma actuators have a wide range of use, all of which depend on the configuration of the actuator. For applications such as separation flow control, a single linear plasma actuator works well, but this configuration can be modified wherein the actuator has a significantly higher impact. Counter-flow actuators have been found to be more efficient in eliminating separation in certain cases, especially when used as leading edge devices to trip the flow. Nonlinear configurations that would suit the needs of a micro jet with two actuators in annular configuration and zero-net mass flux injection can also be considered.[8,9] Similar to other plasma actuators, each of the two actuators are driven by a high voltage, high frequency signal, keeping in mind that the two inner electrodes should be of the same voltage potential to prevent arcing between the two actuators. The actuators are arranged such that they act

in the same streamwise direction as one another, thus directing flow outward and producing a jet.

To increase the effectiveness that plasma actuators can have on flow fields, various actuator geometries that leverage the plasma induced jet is investigated, most notably synthetic jet like flows with vectoring capability. These configurations can be used to generate cross-stream vortices similar to pulsed vortex generator jets, shown in Fig. 1. Other potential uses of these actuators include a single actuator design that can be used for co-flow, counter-flow and the jet vectoring synthetic jet flow control just mentioned, which can also be used as flaps when placed along the trailing edge. Coupled with an intelligent flow monitoring system, these actuators would have the ability to modify their behavior to best suit the requirements for flow control and/or maneuvering, particularly well suited for aerodynamics flow control at the $\mu AV/nAV$ scale.
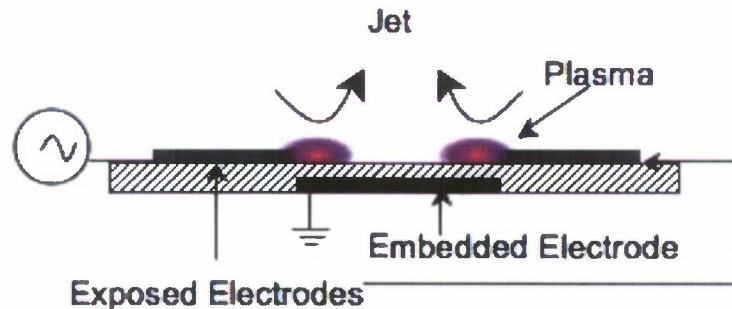
Figure 1. Jet vectoring plasma actuator.

II. Background

A. Previous Work

Studies on flow control devices have primarily been focused on adding momentum to the boundary layer or using trips to initiate transition with leading edge devices. Thus in general, manipulation of the boundary layer has been the main objective for control. In order to achieve this, certain devices such as vortex generator jets (VGJs) or zero-net mass flux synthetic jets and plasma actuators in various configurations have been used. There are many parameters affecting the performance of plasma actuators, thus characteristics of these have been investigated in detail to get better results, while different configurations such as the plasma synthetic jet actuators and the thrust vectoring plasma actuators have

been considered. Only a small fraction of the vast amount of flow control device research is discussed here.

Vortex generation is commonly used in the boundary layer to reattach flow and eliminate separation. Pulsed and steady vortex generator jets on a low pressure turbine blade cascade model were investigated by Mcquilling *et al.*[10] They conducted tests at Re=30,000 to Re=300,000 and PIV measurements indicated that for the uncontrolled case, separation occurred between 63.4% and 67.6% of the suction side length regardless of the Re, turning angle and the free stream turbulence intensity. The use of steady and pulsed VGJs at 46% of the suction side length with a 50% duty cycle however, suppressed separation for almost every case.

McQuilling and Jacob further studied pulsed vortex generator jets for separation control purposes.[11] They placed this geometry on two low pressure turbine blades at different locations of the suction surface length, one close to the leading edge at 10.5% and the other near the trailing edge at 69%. Both steady and pulsed jets with varying duty cycles were investigated and the results indicate that for the 69% location, the VGJs had the most significant effect in eliminating separation. Steady operation controlled separation at all times while the 50% and 10% duty cycles were also very effective. The 10.5% location near the leading edge, however, only eliminated separation at steady cases and was found to be ineffective for either duty cycles for pulsed blowing. It was also seen that the vortical interaction and diameter of the vorticies at the 69% location was larger than the ones at 10.5% location.

Extensive research has been conducted on synthetic jets foe use as flow control devices (e.g. Glezer *et al.*[12]) Synthetic jets are zero-net momentum flux jets like the plasma driven micro thrusters in discussion that successively suck in and blow air out from a cavity in which an oscillating diaphragm is mounted. Although synthetic jets are like pulsed jets in terms of the fact that they are both produced by the advection and interaction of discrete vortical structures, they differ from them, being formed from the working fluid and transferring linear momentum without net mass injection across the flow boundary. The interaction between a synthetic jet and a cross flow was observed and flow control was achieved on scales that are one to two orders of magnitude larger than the characteristic length scale of the jet itself. Use of high actuation frequencies result in the decoupling of the aerodynamic forces from the frequency of the actuators.

Smith and Glezer investigated the interaction between a primary conventional rectangular air jet and a high-aspect-ratio co-flowing synthetic jet using PIV measurements.[13] It was seen that an entrainment region occurs, causing a low pressure region near the flow boundary and allowing the primary jet to deflect towards the synthetic jet. The volume flow rate of the conventional jet imparted into the synthetic jet and hence the vectoring force is dependent

upon the driving frequency and the amount of entrainment for a given synthetic jet strength, duty cycle and primary jet speed. Both the vectoring time and angle increase monotonically as the primary jet speed is decreased while the vectoring angle oscillates at the actuation frequency for stepped modulation. The velocity within the orifice is also increased with stepped modulation of the driving frequency A stagnation point in the interaction region between the jets was observed during the suction stroke and the stagnation streamlines divided the flow into four quadrants, including of the previously mentioned low pressure region. This region becomes time-independant when the actuation frequency is relatively higher than the characteristic jet interaction relaxation time.

The control of separation on a half-cylindrical hump using a synthetic jet has been studied by Suzuki.[14] Direct numerical simulation (DNS) was performed for compressible, unsteady and laminar flow over the hump and the vorticity flux balance at the wall and its centroid were considered. It was found that the periodic actuation reduces the rate of vorticity production, breaking large-scale vortices into smaller ones and also moves the centroid upstream, delaying separation. Thus, performance in terms of lift and drag coefficients, which can be expressed as functions of the vorticity production rate and centroid position, is greatly enhanced. Individually, the lift depends on the horizontal position of the vorticity centroid while the drag is dependent on both the vertical position and the rate of production of vorticity. The forcing frequency controls the the detachment point of the separation vortex, which is determined by the centroids of the vortices produced, found to be $F^+ = f_{act}D/u_\infty \approx 1$ for minimum drag where f_{act} is the forcing frequency of the actuator, D is the chord length and u_∞ is the freestream velocity. It was also concluded that the lift decreases monotonically with the frequency. The other parameter affecting the vorticity centroid was found to be the actuator position at which the clockwise vorticity is created.

The plasma synthetic jet actuator (PSJA) configuration studied by Santhanakrishnan and Jacob consists of an exposed annular electrode and a circular embedded electrode.[15] These differ from the rest of the research conducted on plasma flow control in that the actuator is not used inside the boundary layer but rather outside it. Results indicate that the induced normal jet is very similar to that of the synthetic jet and a maximum velocity of 1 m/s can be obtained. It was also observed that the actuator decreased in effectiveness as the *Re* number was increased. Continued studies on plasma synthetic actuators, which are zero net mass flux devices consisting of annular electrode arrays, have been made for use on flow control and thrust generation.[8,9] It was found that unlike synthetic jets, this configuration can be reversed to be used for suction. The actuator was mounted on a plate and pulsed with modulation frequencies of 1 Hz, 10 Hz & 100 Hz. It was found that pulsed actuation creates a starting vortex ahead of the induced jet while a secondary vortex ring is trapped, and a tertiary ring near the surface is observed as a result of entrainment in the boundary layer.

This starting vortex was seen to be important in determining the maximum velocity and streamwise extent of the jet. When the forcing frequency was varied, it was observed that multiple vortex rings were formed and the interaction of the primary vortex rings resulted in an increase of the peak velocity, a value of $O(1 \text{ m/s})$ at a frequency of 10 Hz found in previous research. The effect of a crossflow was also investigated where the jet penetrates into the mean flow, thereby acting like a conventional jet with reduced effectiveness on the flow and boundary layer characteristics as the mean velocity is increased.

A number of thrust vectoring applications using plasma actuators were investigated recently by Porter et al.,[16] Benard et al.[17] and Bolitho and Jacob.[18] The variation of spanwise force in a plasma actuator was observed by Porter et al.[16] This was done by changing the shape of the embedded electrode so that the volume of the plasma created could be controlled, which in turn directly affects the body force produced. PIV measurements showed that steady jets with varying force along the actuator span could be generated by changing the width of the embedded electrode. Steady jet vectoring was also achieved wherein two linear actuators facing each other were used and their strengths were varied asymmetrically via changes in the applied voltage. Results showed that the jet can be controlled 180 degrees with small voltage variations. A similar study was made by Benard et al.[17] They also used two opposite single DBD actuators to create two impacting wall jets that result in a wall normal jet of maximum velocity of 1.9 m/s. This configuration was then used to control separation at the leading edge of a NACA 0015 airfoil at a freestream of 15 m/s. Lift and drag force measurements showed that a significant increase in lift and a reduction in drag occurred when the jet was normal to the wall or at a pitch angle of $+18$ degrees. Steady and unsteady vectoring of flow in a linear dielectric barrier discharge plasma synthetic jet actuator for a number of flow control applications were examined by Bolitho and Jacob.[18] It was shown that the direction of the steady jet produced could be controlled by varying the strength of the continuous dielectric barrier discharge. Similar to the current study in this report, unsteady jet vectoring was also investigated wherein the duty cycle and the plasma frequency of the actuators was varied asymmetrically. The results obtained showed that the latter was more effective. It was also seen that the pulsing frequency controlled the type of jet produced; near wall jets, standing vortices, or wall normal jets were obtained. Further discussion can be found in Bolitho.[19]

B.   Current Work

Various actuator configurations are investigated in order to enhance the capability of the plasma induced jet for flow control applications. Specific emphasis is made on the linear plasma synthetic jet actuators for vectoring purposes and a parametric analysis is carried out to determine the capability best used in flow control and maneuvering applications.

III. Experimental Setup

The jet vectoring configuration, also referred to as the linear plasma synthetic jet actuator (linear PSJA), is similar to the linear case wherein a single embedded electrode is separated from two exposed electrodes on either side by the dielectric, shown previously in Fig. 1. For the experiments conducted with these vectoring actuators, alumina and teflon plates with respective thicknesses of 0.0635 cm and 0.16 cm were used as the dielectric materials.

All tests with the jet vectoring actuators were conducted in a low speed wind tunnel. An input signal in the form of a square wave and frequency range of 5-9 kHz is generated by a program in Labview with a block diagram for two channels. The signals are then provided to the actuator by a data acquisition unit. A power input of about 5 V is connected to the actuators through two CMI 5012 transformers and a QSC RMX 1450 amplifier with an amplification ratio of 1/60, which results in an output power of about 10 kV and 12 W.

Current and voltage measurements for several cases were made with a NK Technologies AC current transducer and a North Star PVM-11 1000:1 high voltage probe, respectively. An oscilloscope was employed to obtain these readings and plot them, later to be used in power calculations.

The induced velocity of the jet was measured with a PIV system with components including a monochrome Kodak Megaplus ES 1.0 CCD camera with a resolution of 1008 x 1018 pixels and a double exposure capability to capture an image pair within a small period of time, a dual-head Nd:YAG laser from Big Sky Lasers with 45 mJ of output energy, wavelength of 532 nm, pulse width of 6 ns and beam diameter of 2.8 mm, a Quantum Composer timing box that controls and synchronizes the camera and laser heads, an oscilloscope to monitor timing of the laser pulses, a Turbofog fog generator to introduce particles into the flow field, optics for laser sheet generation, a computer with frame grabber hardware (PIXCI D) and software (XCAP) for image acquisition and finally, PIV processing software as discussed below.

To acquire PIV measurements, the wind tunnel containing the actuator is seeded with smoke particles on the order of 1 micron in diameter. A 2-D light sheet of about 2 mm thickness is projected in the vertical plane through the center of the circular tube using the Nd:YAG laser. The set of optics consists of three lenses that create the laser sheet. The laser first goes through a converging lens, is focused, then passes from a diverging lens placed at the focal length of the first lens and becomes more concentrated. Finally, the last circular lens diffuses the beam and the 2-D laser sheet is formed. The timing control unit is used to pulse the lasers in synchronization with the CCD camera. The vertical field of view is approximately 4 to 6 cm with a resolution ranging from 97 pixels/cm to 269 pixels/cm. Epix frame grabbing hardware and software is used to acquire binary image pairs. For each run,

63 image pairs were captured at a rate of approximately 10 Hz with 50 microseconds of delay between the laser pulses and these images were processed using the algorithm given below. The velocity and vorticity fields obtained in post-processing were then averaged over the data set.

The PIV algorithm utilizes the wall adaptive Lagrangian particle-tracking algorithm (WaLPT) developed by Sholl and Savaş.[20] This algorithm treats the seeding as fluid particles and determines their translations and deformations. Fluid parcels registered by CCD pixels are advected with individually estimated velocities and total accelerations. A standard DPIV algorithm is employed to determine the initial velocity field, and the routines in WaLPT allow for highly accurate measurement of the velocities near surfaces by mirroring the flow about the wall using an image parity exchange routine.[21] Velocity and vorticity are calculated as part of the PIV algorithm and scaled accordingly; vorticity is determined spectrally and does not suffer from typical numerical differentiation problems.

For the streamwise measurements, the actuator was placed inside the 30.5 cm x 30.5 cm test section. The camera was mounted perpendicular to the laser sheet passing through the centerline of the tube exit cross section. For the cross flow measurements, however, a prism was placed just downstream of the actuator so that the CCD camera, the laser and optics could all be mounted outside the wind tunnel. The vertical field of view was about 10 cm with resolution values between 97 pix/cm and 269 pix/cm.

IV.   Results

Both average and transient velocity measurements for the jet vectoring plasma actuator shown in Fig. 1 were acquired with the PIV system. Experiments were conducted with varying parameters such as the duty cycle and wind tunnel speed to observe their effect on the induced flow field where the actuator acts as a vortex generator jet. No quiescent measurements were made and the duty cycle was the only input parameter varied throughout the tests. This is mainly due to the fact that changing the duty cycle has a greater sensitivity to the angle change and allows less power input. Extensive information on the parametric study for jet vectoring actuators in quiescent flow can be found in Bolitho.[19] where steady vectoring was also considered. The volume and thus the strength of the plasma was varied by changing the driving frequency of the two sides with variations in the jet angle shown in Fig. 2. It can be seen that by decreasing the operating frequency of one side of the actuator away from its optimum, and holding the other side at a constant frequency, the angle of jet is changed. The relationship between the angle of the jet and the frequency differential, over the span studied, is approximately linear. The effect of varying the duty cycles is also shown in Fig. 3 where one can control the angle at which the jet is produced while decreasing the

input power. Fig. 3 shows the relationship between the approximate angle, measured from the normal to the wall, and the duty cycle of the second channel, while the first is held at 50%. Near symmetric operation, there are large changes in the angle of jet produced with any change in duty cycle, but lowering the duty cycle beyond about 40% shows very little change in the angle of jet created. Further results are presented in this section.

Flow visualization was employed to observe the detailed structure of the induced flow. A smokewire was placed at the entrance of the tunnel test section to seed the flow. The actuator in Fig. 4 is built on the alumina plates and pulsed at 250 Hz while the duty cycles are at 50% and 30% for the left and right channels, respectively. From the streamlines close to the actuator surface, it can be seen that similar to a linear actuator, the flow is being pulled in and pushed back out. However, even though it is not apparent in this figure, the streamlines are not straight, but tend to lean towards the left strip. This results from the fact that the left side is pulsed at a higher duty cycle of 50%, causing the plasma to be stronger and to pull the flow to itself. The behavior of the flow after being directed inwards can also be seen clearly where the streamlines closer to the plate surface are directed in and out around the leading edge while the upper streamlines are directed inwards at a further downstream distance. This causes braiding of the streamlines and this corkscrew structure propagates downstream with time.
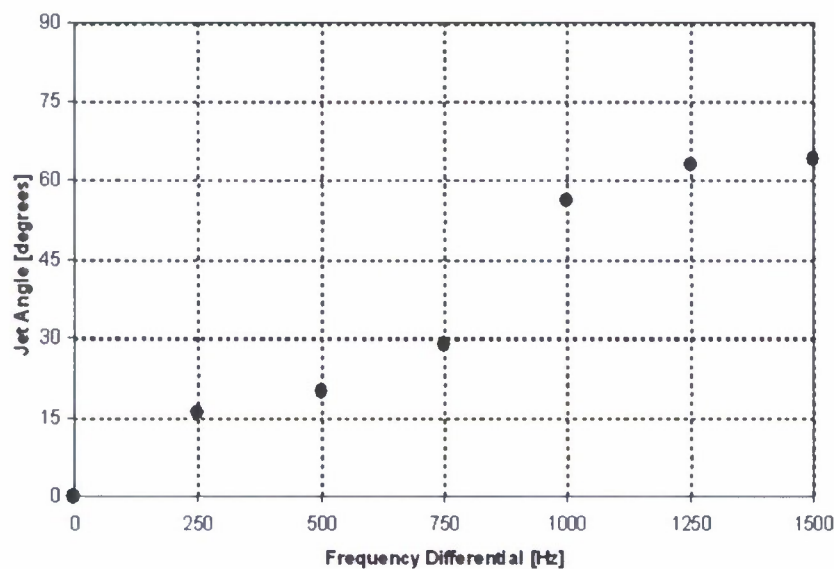
Figure 2. **Variation in angle of jet by decreasing the operating frequency of one side of the jet vectoring plasma actuator.**

For the first set of experiments, the jet vectoring actuator on the alumina plate was employed at constant plasma and modulation frequencies of 9000 Hz and 250 Hz, respectively, with a phase angle of 180 degrees between the two channels and tunnel speed of 1.28 m/s.
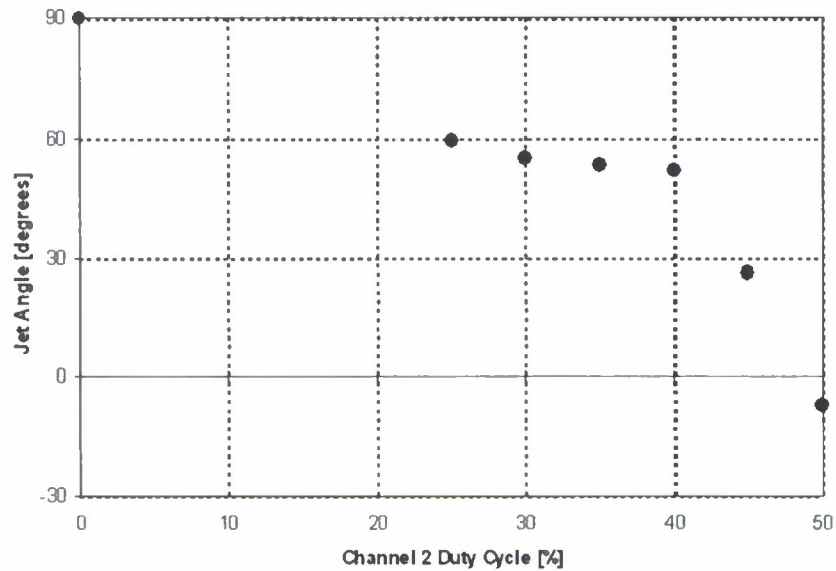
Figure 3. Variation of jet angle with duty cycle.
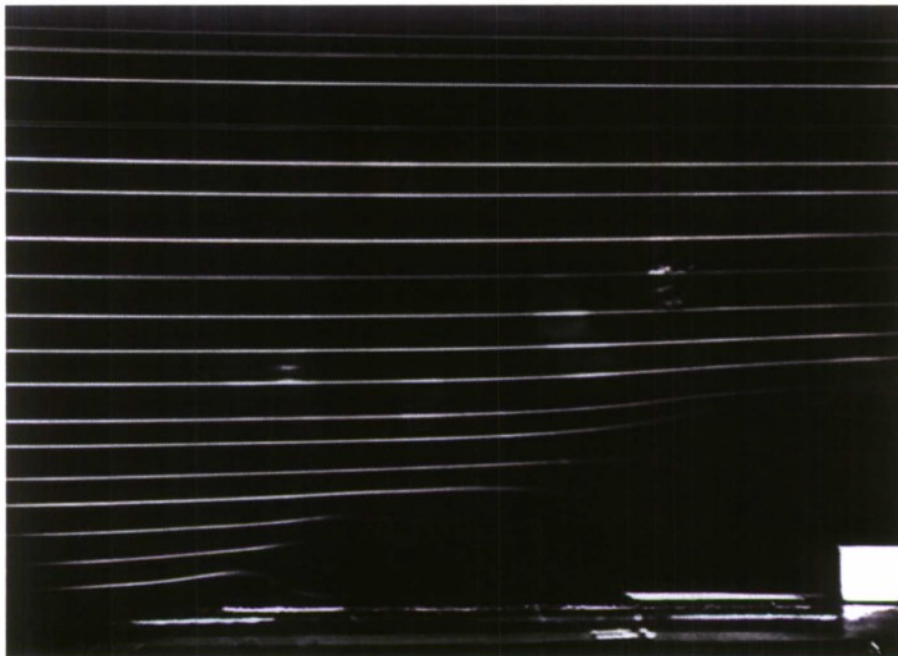
Figure 4. Smokewire flow visualization in freestream for the jet vectoring plasma actuator.

The forcing frequency of 250 Hz was chosen regarding the fact that it is above the critical frequency required to produce a jet in quiescent flow.[19] This is also verified by hotwire measurements obtained at different forcing frequencies, where it could be seen in Fig. 5(a) that the velocities for the 100 Hz case are significantly lower than the others. As the frequency is increased above the critical forcing frequency, the increase in the mean velocity is reduced

while the amount of deviation from the mean is larger due to the turbulent fluctuations, shown in Fig. 5(b). The duty cycles of the channels were varied to observe the effect on the flow field; one side was kept at a 50% DC while the other was varied from 0% to 50%. Then, the opposite case was observed where the initially constant duty cycle actuator was varied from 50% to 0% and the other was kept constant at 50%. Fig. 6 shows the absolute maximum vorticity values for each of these cases. It can be seen that for the cases of 0%/50% and 50%/0% duty cycles, which are simply linear actuators without vectoring, there is a significant amount of drop in the maximum vorticity. This could also be observed for the cases with a 40%, 30% and 20% DC for one side and 50% DC on the other. This is due to the fact that the plasma strengths on the two sides are not equal. For the first five vectoring cases, where the left side is kept at 50% DC, the vorticity values are significantly higher, implying that this side produces stronger plasma. The 50%/50% case should normally yield a lower vorticity if the plasma strengths were equal since both sides would tend to cancel each other out. This is seen in the 40%/50% case where the vorticity reaches a minimum, changes sign and starts to increase again, which is expected with increasing discrepancy between the duty cycles of the two channels. These values would be as high as the case with the left side at 50% DC but since there is an asymmetry, the vorticity is dominated by the left side and is kept at lower values.

Even though it is not investigated in the experiments here, the effect of the yaw angle on the vortex strength is also significant and should be mentioned.[19] When there exists a yaw angle between the freestream and the actuators, the vortex from the boundary layer over the plate tends to increase the strength of the vortex produced by one side while decreasing the one created by the other side. This is illustrated in Fig. 7 where it could be seen that for the case with the yaw angle, ω_z adds to the cross stream component of the vortex created by the left side, ω_1.

The circulation distribution is plotted against the radius in Fig. 8 for all cases and it can be seen that the higher the strength of the vortex created is, the larger the circulation values are for that case. As expected, the circulation values start increasing at the outer radius of the vortex, reach a maximum at the center and start decreasing again. Note that after the 40%/50% DC case where the vortex changes direction, the circulation values are negative.

In order to observe and track the position of the vortices for these cases, a hodograph was used where the coordinates of the vortex centers were plotted relative to the actuator, shown in Fig. 9. Note that the 0%/50% and 50%/0% cases are on opposite sides of the actuator since they are positioned in the direction of the near wall jet that is induced with a linear actuator. The near wall jet also explains the fact that these two cases yield the smallest vertical distance from the actuator. As the right side is varied and the left side is kept at 50% DC, it could be seen on the right side of the figure that as a result of vectoring,

the jet and hence the vortex center starts moving away from the wall. The same phenomena occurs on the left, but after the 10%/50% case, as just mentioned, the asymmetry in plasma strengths causes a certain randomness in the position of the vortex centers. If it were not for the asymmetry, the hodograph would appear as shown in Fig. 10. Streamlines and vorticity contours obtained from the PIV measurements are also shown in Fig. 11. As mentioned previously, the motion of the vortex can be observed in going from the 50%/0% case to the 0%/50% case; 180 degrees of vectoring from a near wall jet on the left side of the actuator to a near wall jet on the right side. The changes in the locations of the vortex is not as clear as in the hodograph since the range of the cross stream x-axis was varied to capture all of the vortex for each of the cases while the vertical position of the plate was also changed once during the experiments. The change in the sign of the the vorticity can also be observed in cases after the 40%/50% DC case in Fig. 11(g). This would be expected to be seen after the case where both channels are operated at 50% DC if the two sides were symmetric. For most of the cases with the right side kept at 50% DC, the asymmetry is very apparent where since the left side is stronger, the vortex resulting from actuation is visible along with the vortex of the right side rather than showing up as a single vortex on the right.

(a) Velocity vs. time.

(b) Velocity vs. forcing frequency.
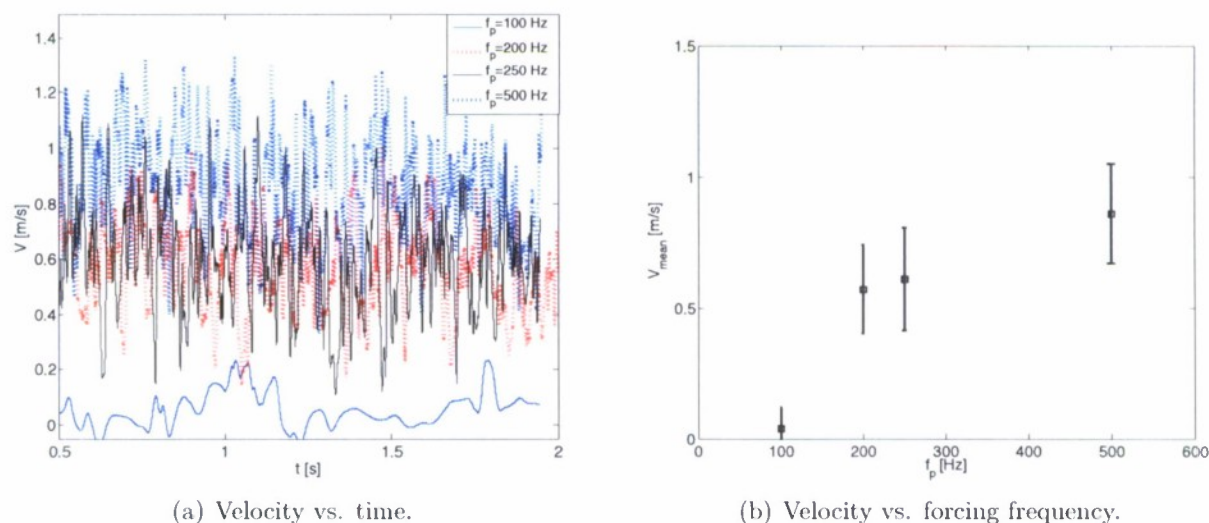
Figure 5. Hotwire measurements for the jet vectoring actuator with both sides at 50% DC.

A second set of tests were conducted to observe the evolution of the vortex structures that form upon actuation. The jet vectoring actuator was pulsed once more at the same parameters; plasma and modulation frequencies of 9000 Hz and 250 Hz, 180 degrees of phase angle and a tunnel speed of 1.28 m/s. PIV data was acquired along the streamwise direction, at 0%, 25%, 50%, 75% and 100% chord locations. Fig. 12 shows the case for both channels pulsed at 50% DC where Fig. 12(a) is the variation of the maximum vorticity values with chordwise position. It is clear that the vortex is strongest around the mid-chord location
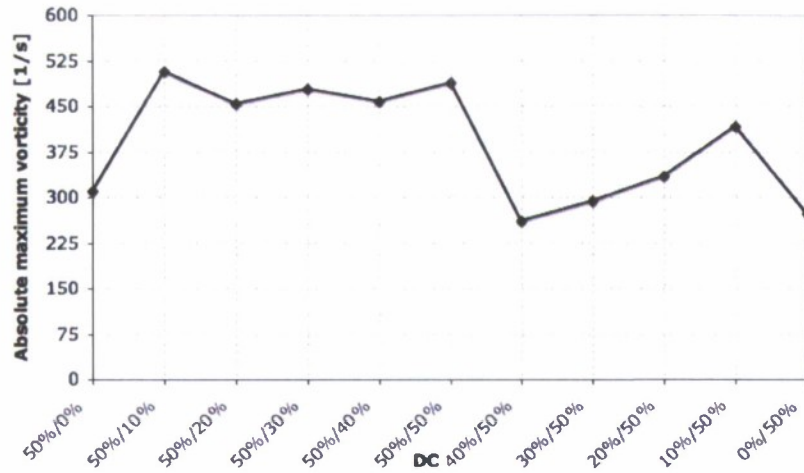
Figure 6. Variation of absolute maximum vorticity with changing duty cycles in both channels.
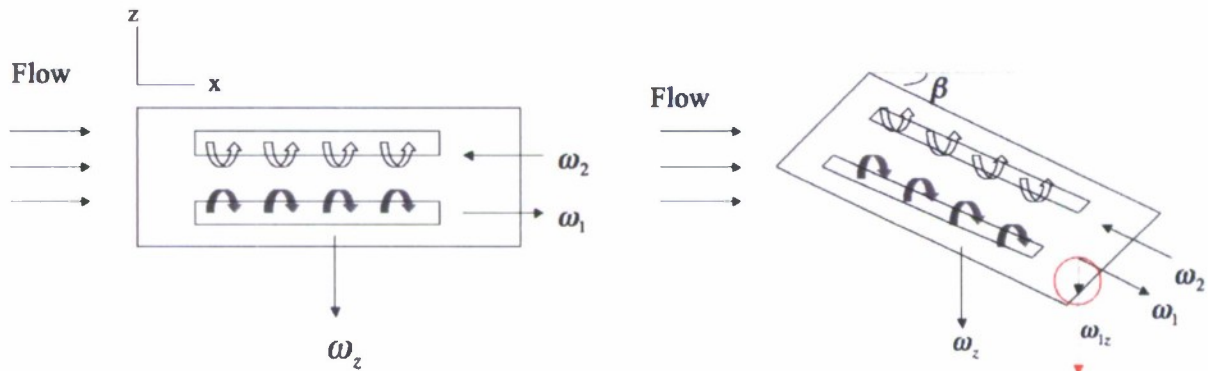
Figure 7. Effect of yaw angle on vortex strength.

(mid-chord for this case) and weakest at the leading edge. The circulation variation with radius is also plotted in Fig. 13(a) where it can be seen that as going downstream, circulation is added continuously. Note that, however, the bulk of it is introduced around the mid-chord region, also seen in Fig. 13(b), where the strongest vortex is observed. This is because further downstream, the vortex generated by the actuator is subsumed in the boundary layer and is unable to add to the strength of the initial vortex advecting downstream and moving away from the plate. Thus, the increase in the circulation is limited after mid-chord and separate vortices will be formed as in Fig. 14, meaning that there is no need for a large streamwise length for these actuators. The hodograph in Fig. 12(b) illustrates the motion of the vortex along the chord. Looking back at Fig. 9, it can be seen that the 50%/50% case at mid-chord location yields a vortex to the left of the actuator, which is consistent with these locations to the left of the actuator. Note that this motion resembles that of the one previously seen in the flow visualizations in Fig. 4, resulting in the braiding of the streamlines as they move downstream. Similar to the previous experiments, streamlines were plotted to show these
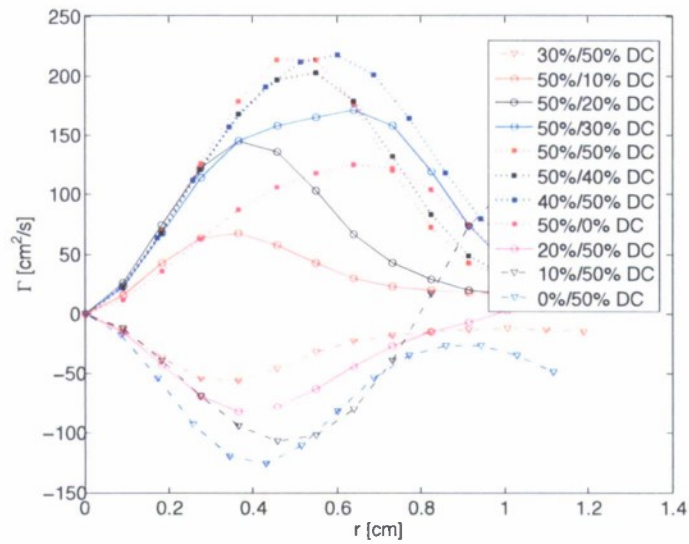
Figure 8. Circulation vs. radius for varying duty cycles in both channels.
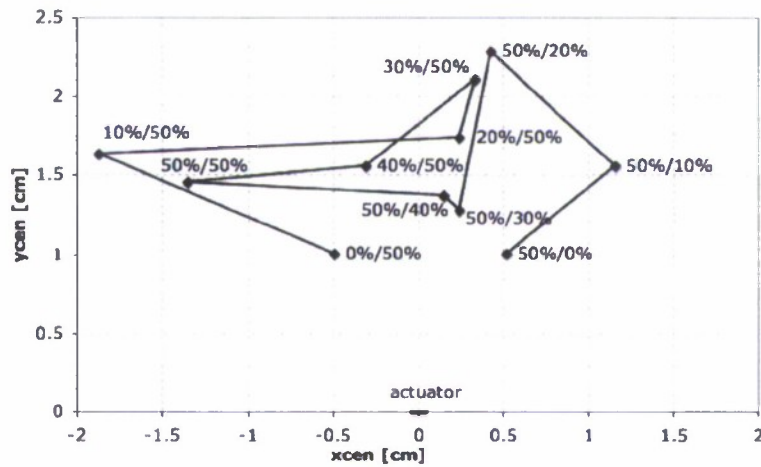
Figure 9. Hodograph for jet vectoring actuator with varying duty cycles in both channels.
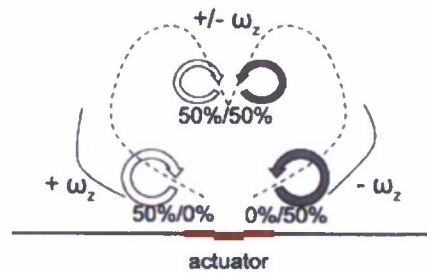
Figure 10. Expected hodograph for jet vectoring actuator with equal plasma strength on both sides.

effects on the location of the vortex illustrated in the hodograph. Observe in Fig. 15 that the vortex is barely visible and low in strength at the leading edge, after which it starts to grow in size and becomes the largest at the trailing edge with the highest strength at the mid-chord location. As previously explained, the vortex starts moving away from the wall and the plasma actuator is incapable of increasing the strength of the detached vortex. The increasing size can also be observed in the flow visualizations with the growing boundary layer along the chord.

Similarly, for the case with the left side held at 10% DC and the right at 50% DC the maximum vorticity variation and the vortex locations were plotted as seen in Fig. 16(a) and (b). Note that the peak value of the maximum vorticity occurs around mid-chord again (at the 25% chord location this time), with a similar circulation distribution in Fig. 17(a) to the previous case, again implying that the circulation is mainly added in these regions, also illustrated in Fig. 17(b) while the hodograph is very clear in terms of the braiding motion just explained for the previous case. Although not shown here, the 2-D plots of streamlines illustrate this motion and the growth of the vortex along the streamwise direction. Thus, for these tests in the streamwise direction, it can be said that the motion and evolution of the vortex along the chord is basically the same regardless of the duty cycle of the two channels.

For the last set of runs, the jet vectoring actuator was placed in the chordwise direction on a NACA 0012 airfoil with a chord of 15.24 cm, span of 30.48 cm and an angle of attack of 10 degrees. Instead of the alumina, the teflon plate of 0.16 cm thickness was used as the dielectric in order to have the flexibility to embed the actuator on the wing. Streamwise PIV measurements were taken for two different tunnel speeds of 0.62 m/s and 1.28 m/s with the same forcing frequency of 250 Hz, phase angle of 180 degrees and plasma frequency of 9000 Hz as in the previous tests. Fig. 18 illustrates the effect of the actuator on separation and stall control at the lower tunnel speed using reverse flow probability. The red color represents flow that is opposite the direction of freestream while the blue is flow in the freestream direction. The colors in between are the cases where some of the flow is upstream and the rest is downstream, yellow for example, means half of the velocity vectors are in the freestream direction while the other half is in the opposite direction. It can be seen that in Fig. 18(a) where the actuator is turned off, the separation region is very apparent while for any of the other three cases in Fig. 18(b), (c) and (d), the actuator acts as a vortex generator, energizes the boundary layer and suppresses separation. It could also be observed that the any of the two vectoring cases are more effective in controlling the separation than the linear case, while the 50%/50% DC case yields better control than the 30%/50% DC, resulting from the fact that the vortex in the previous case is stronger than the latter. For the higher speed of 1.28 m/s, however, it can be observed in Fig. 19 that the 0%/50% DC case is actually more efficient than the vectoring cases while the 50%/50% DC case still

yields better results than the 30%/50% DC case, which is also consistent with the maximum vorticity values in Fig. 6. The effectiveness of all the actuators decrease with increasing tunnel speed, although it is possible that the upstream motion observed in the RFP plots could be the vortex generated by the actuators mounted on the airfoil. Although it has not been done in this case, boundary layer profiles would be useful to verify whether there is separation or not for these higher speeds with the actuators on.

V. Conclusions

Tests with the jet vectoring actuator show that the jet direction can be controlled 180 degrees by changing the duty cycle of the channels with respect to one another. The maximum vorticity values for the linear cases with 0%/50% and 50%/0% duty cycles are less than any vectoring case with different duty cycles on each channel. As for these vectoring cases, the tests with a 40%, 30% and 20% DC for one side and 50% DC on the other yield low vorticity as well, resulting from the asymmetry of plasma strength on the two channels. Because of this asymmetry, while the least amount of vorticity is expected for both channels at 50% DC, this occurs for the 40%/50% case where the vorticity reaches a minimum, changes sign and starts to increase again with increasing discrepancy between the duty cycles of the two channels. This increase, however does not reach the values for the cases with the left side at 50% DC since the weaker right side is the main contributor to the vorticity now. A hodograph with the coordinates of the vortices illustrates that their movement is in the direction of the vectoring. Streamwise PIV measurements show that there is a significant amount of growth in the vortex along the chord from the leading edge to the trailing edge while the location of the vortex centers via hodographs and velocity vectors illustrate the braiding motion along the chord. The maximum strength is observed at 50% chord for the case with both sides at 50% DC and at 25% chord for the left side at 10% DC and the right at 50%. The values do not vary drastically between the quarter-chord and mid-chord for each case though, meaning that the maximum strength is achieved around the mid-chord regions in general. As the radial circulation distributions illustrate, the circulation is mainly introduced in this region, and its continuous increase is less as the vortex is subsumed inside the boundary layer at further downstream distances. Regarding results above, it is evident that the jet vectoring actuator can be used for rapid change of the vortex sign, location and distribution, which is an improvement over a linear configuration for flow control.

The jet vectoring actuator placed on the wing proves to be effective in controlling separation, where at the lower speed of 0.62 m/s, appreciable separation control is achieved for all three cases of 0%/50%. 30%/50% and 50%/50% duty cycle values for the left and right channels, respectively. However, pulsing the actuator with 50% DC on both sides yields the

best results since it generates the strongest vortex, followed by the 30%/50% and 0%/50% cases. This proves that the jet vectoring actuator is more efficient than a simple linear one, but at higher tunnel speeds the actuator decreases in efficiency and employing a linear actuator results in better flow control. Overall, though, it has been shown that the jet vectoring plasma actuator can be used as a vortex generator device to provide flow control.

VI.   Acknowledgements

References

[1] T. C. Corke, E. J. Jumper, M. Post, D. Orlov, and T. E. McLaughlin, "Application of weakly-ionized plasmas as wing flow-control devices," AIAA Paper 2002–0350, 40th AIAA Aerospace Sciences Meeting and Exhibit, Reno, NV, Jan. 2002.

[2] L. S. Hultgren and D. E. Ashpis, "Demonstration of separation delay with glow-discharge plasma actuators," AIAA Paper 2003–1025, 41 st AIAA Aerospace Sciences Meeting and Exhibit, Reno, NV, Jan. 2003.

[3] M. L. Post and T. C. Corke, "Separation control using plasma actuators – dynamic stall control on an oscillating airfoil," AIAA Paper 2004–2517, 2nd AIAA Flow Control Conference, Portland, OR, June 2004.

[4] T. E. McLaughlin, M. D. Munska, J. P. Vaeth, T. E. Dauwalter, J. R. Goode, and S. G. Siegal, "Plasma-based actuators for cylinder wake vortex control," AIAA Paper 2004–2129, 2nd AIAA Flow Control Conference, Portland, OR, June 2004.

[5] J. D. Jacob, R. Rivir, C. Carter, and J. Estevadeordal, "Boundary layer flow control using ac discharge plasma actuators," AIAA Paper 2004–2128, 2nd AIAA Flow Control Conference, Portland, OR, June 2004.

[6] J. D. Jacob, K. Ramakumar, R. Anthony, and R. B. Rivir, "Control of laminar and turbulent shear flows using plasma actuators," TSFP 4-225, 4th International Symposium on Turbulence and Shear Flow Phenomena, Williamsburg, VA, June 2005.

[7] J. Huang, T. C. Corke, and F. O. Thomas, "Plasma actuators for separation control of low-pressure turbine blades," *AIAA Journal*, vol. 44, no. 1, pp. 51–57, 2006.

[8] A. Santhanakrishnan and J. D. Jacob, "On plasma synthetic jet actuators," AIAA Paper 2006–0317, 44th AIAA Aerospace Sciences Meeting and Exhibit, Reno, NV, Jan. 2006.

[9] A. Santhanakrishnan and J. D. Jacob, "Flow control with plasma synthetic jet actuators," *J. Phys. D: Appl. Phys.*, vol. 40, 2007.

[10] M. McQuilling, B. Hollon, and J. D. Jacob. "Active separation flow control in a low pressure turbine

blade cascade model," AIAA Paper 2003–0615, 41st Aerospace Sciences Meeting and Exhibit, Reno, NV, Jan. 2003.

[11]M. McQuilling and J. D. Jacob, "Effect of chord location on separation control with vortex generator jets on low pressure turbine blades," AIAAaper 2004–2205, 2nd AIAA Flow Control Conference, Portland, OR, June 2004.

[12]A. Glezer and M. Amitay, "Synthetic jets," *Annual Rev. of Fluid Mech.*, vol. 34, pp. 503–529, 2002.

[13]B. L. Smith and A. Glezer, "Jet vectoring using synthetic jets," *J. Fluid Mech.*, vol. 458, pp. 1–34, 2002.

[14]T. Suzuki, "Effects of a synthetic jet acting on a separated flow over a hump," *J. Fluid Mech.*, vol. 547, pp. 331–359, 2006.

[15]A. Santhanakrishnan, K. Ramakumar, and J. D. Jacob, "Characteristics of a plasma synthetic jet," ORAL PRESENTATION, Bulletin of the American Physical Society Fluid Dynamics Division, Annual Meeting, Nov. 2005.

[16]C. Porter, A. Abbas, K. Cohen, T. McLaughlin, and C. Enloe, "Spatially distributed forcing and jet vectoring with a dielectric barrier discharge plasma actuator," AIAA Paper 2008–1374, 46th Aerospace Sciences Meeting and Exhibit, Reno, NV, Jan. 2008.

[17]N. Benard, J. Jolibois, G. Touchard, and E. Moreau, "A directional plasma-jet device generated by double dbd actuators - an active vortex generator for aerodynamic flow control," AIAA Paper 2008–3763, 4th Flow Conference, Seattle, WA, 2008.

[18]M. Bolitho and J. Jacob, "Thrust vectoring flow control using plasma synthetic jet actuators," AIAA Paper 2008–1429, 46th Aerospace Sciences Meeting and Exhibit, Reno, NV, Jan. 2008.

[19]M. Bolitho, "Jet vectoring and vorticity generation using plasma actuators," Master's thesis, Oklahoma State University, Stillwater, Oklahoma, May 2008.

[20]M. Sholl and Ö. Savaş, "A fast lagrangian PIV method for study of general high-gradient flows," AIAA Paper 1997–0493, 35th AIAA Aerospace Sciences Meeting, Reno, NV, Jan. 1997.

[21]L. Tsuei and Ö. Savaş, "Treatment of interfaces in particle image velocimetry," *Experiments in Fluids*, vol. 29, pp. 203–214, 2000.

(a) 50%/0% DC

(b) 50%/10% DC

(c) 50%/20% DC

(d) 50%/30% DC

(e) 50%/40% DC

(f) 50%/50% DC

(g) 40%/50% DC

(h) 30%/50% DC

(i) 20%/50% DC

(j) 10%/50% DC

(k) 0%/50% DC
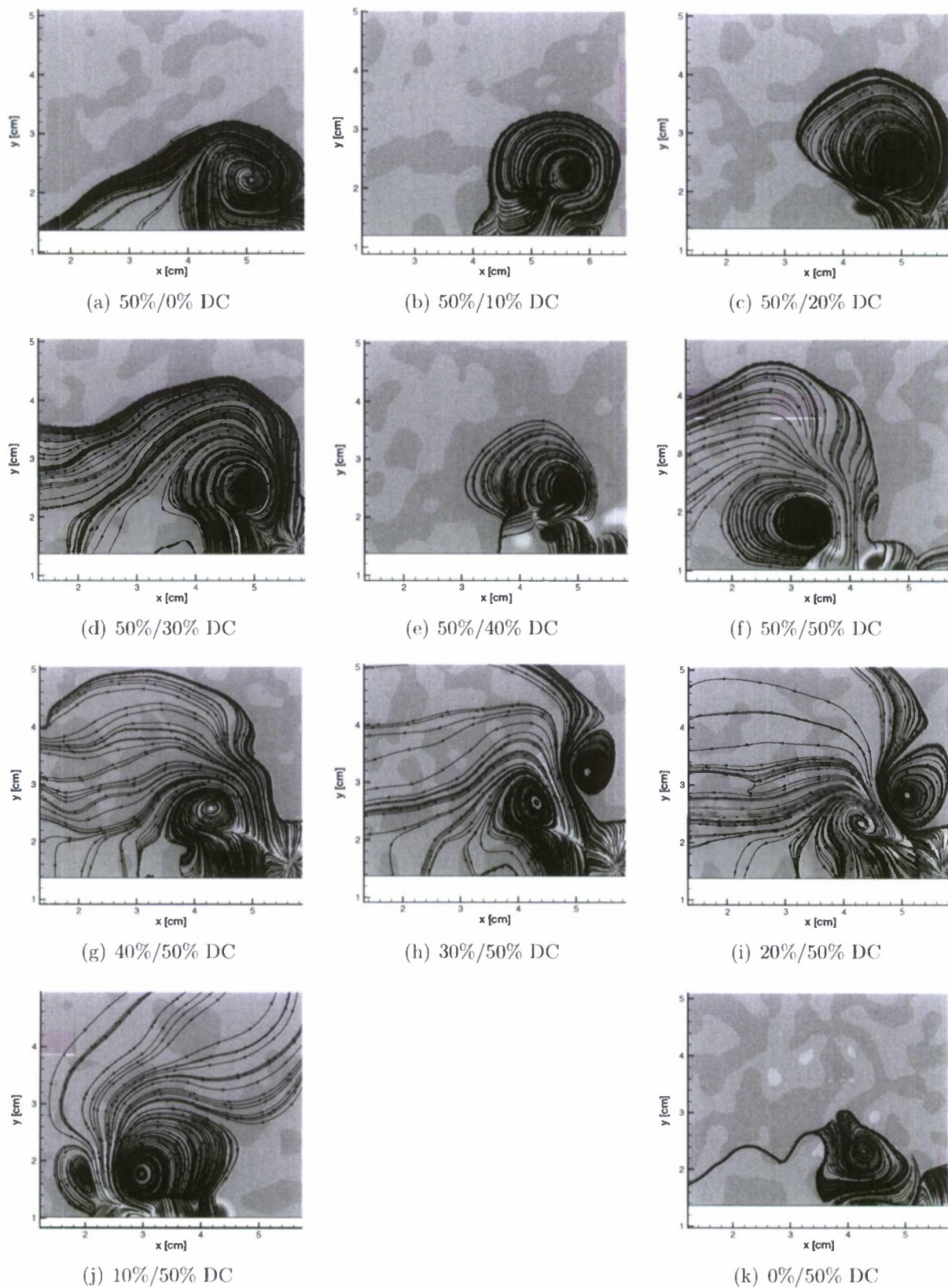
Figure 11. Streamlines and vorticity contours for the jet vectoring actuator with duty cycle discrepancy between the left and right channels.
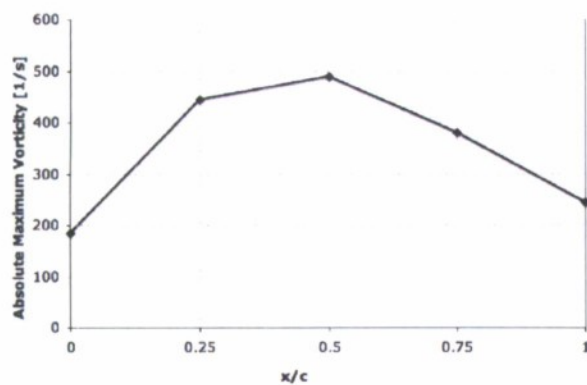
(a) Absolute maximum vorticity vs. chord location.
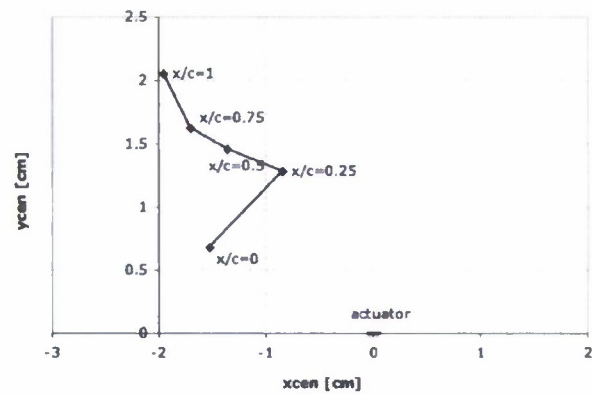
(b) x vs. y-coordinates of vortex centers.

Figure 12. Variation of vortex strength and position with chord location for both channels at 50% DC.
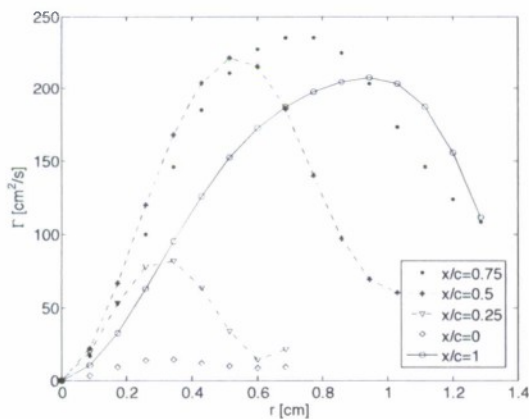
(a) Circulation vs. radius.
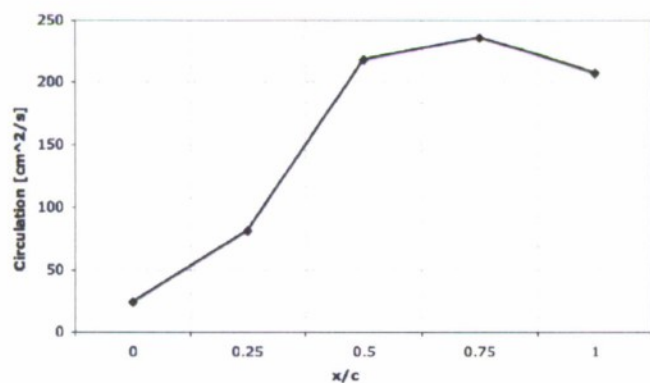
(b) Circulation vs. chord location.

Figure 13. Circulation variation with radius and chord location for both channels at 50% DC.
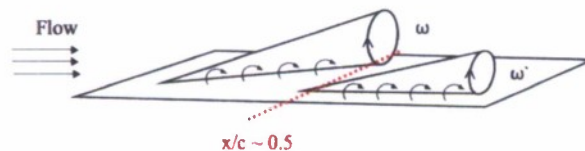
Figure 14. Formation of separate vortices along the streamwise direction.
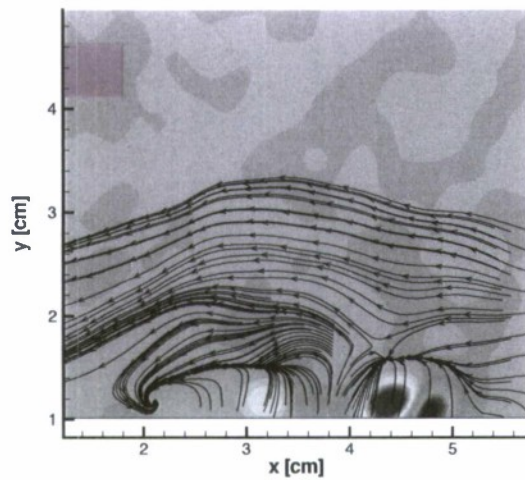
(a) x/c=0
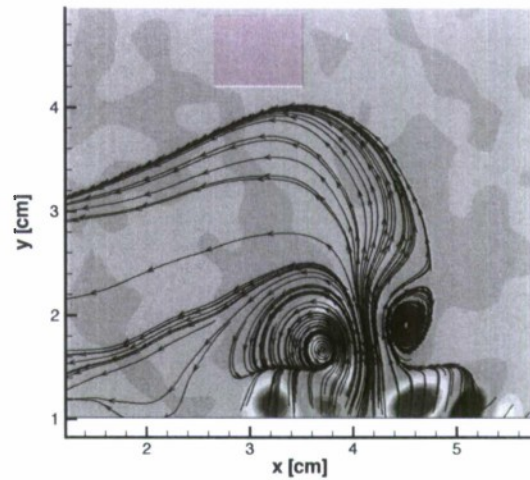
(b) x/c=0.25
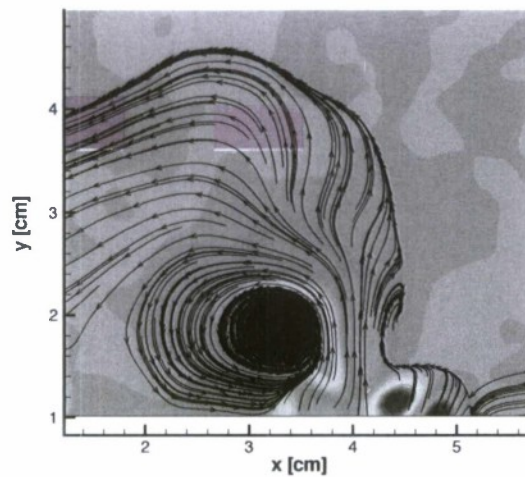
(c) x/c=0.5
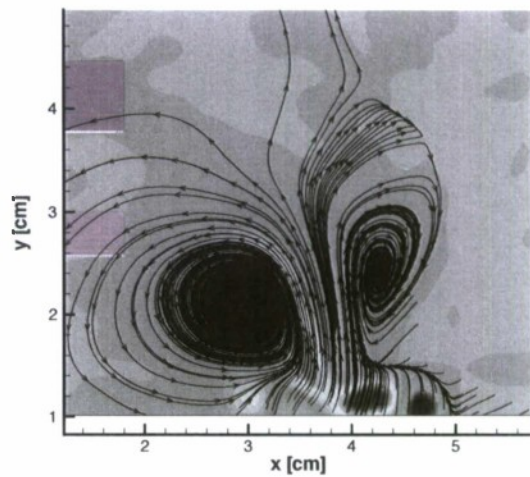
(d) x/c=0.75
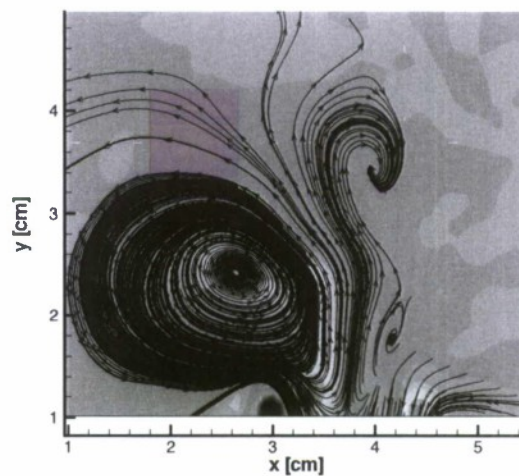
(e) x/c=1

Figure 15. Evolution of the vortex structure along the chord length for both channels at 50% DC.
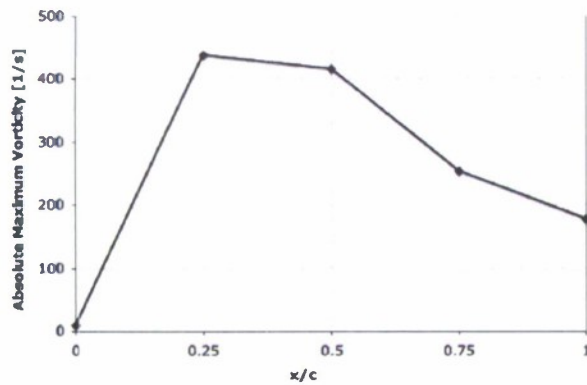
(a) Absolute maximum vorticity vs. chord location.
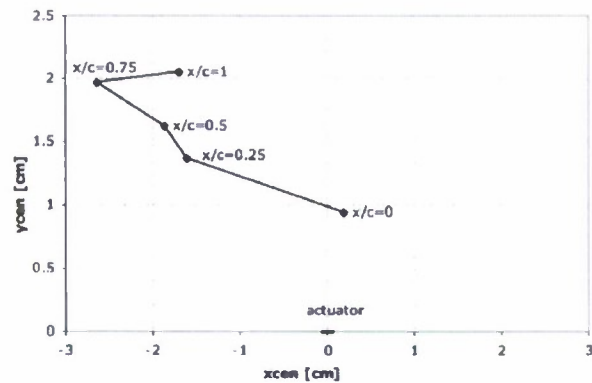
(b) x vs. y-coordinates of vortex centers.

Figure 16. Variation of vortex strength and position with chord location for one channel at 10% DC and the other at 50% DC.
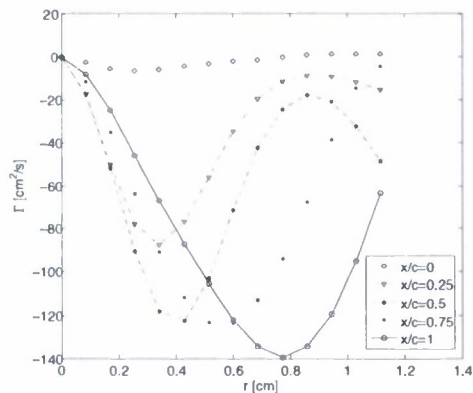
(a) Circulation vs. radius.
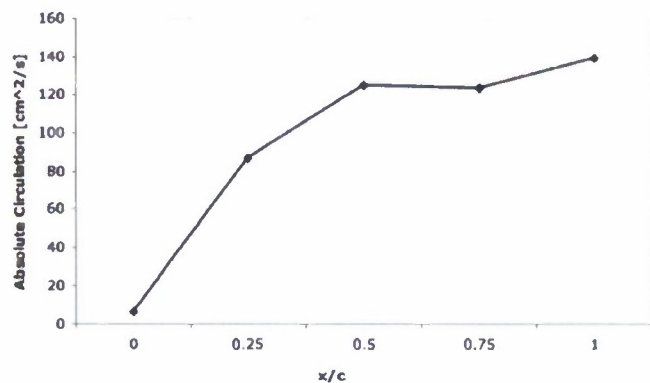
(b) Circulation vs. chord location.

Figure 17. Circulation variation with radius and chord location for one channel at 10% DC and the other at 50% DC.

(a) actuator off

(b) 0%/50% DC

(c) 30%/50% DC

(d) 50%/50% DC

Figure 18. Reverse flow probability on the NACA 0012 airfoil with 0.62 m/s tunnel speed and a.o.a=10 degrees.
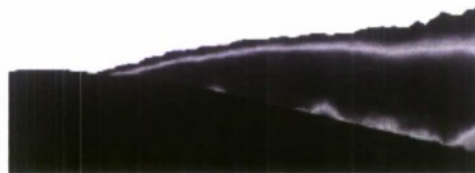
(a) actuator off

(b) 0%/50% DC

(c) 30%/50% DC

(d) 50%/50% DC

Figure 19. Reverse flow probability on the NACA 0012 airfoil with 1.28 m/s tunnel speed and a.o.a=10 degrees.

Part Ib

Development of Plasma Micro Thrusters

I. Goals

This portion of the study examines the use of plasma actuators discussed in §Ia of the report for use as propulsion devices at the nAV scale. Plasma actuators have a wide range of use, all of which depend on the configuration of the actuator. For applications such as separation flow control, a single linear plasma actuator works well, but this configuration can be modified to suit the needs of a micro thruster utilizing the two dimensional version of a micro jet with two actuators in annular configuration and zero-net mass flux injection.[1,2] Similar to other plasma actuators, each of the two actuators are driven by a high voltage, high frequency signal, keeping in mind that the two inner electrodes should be of the same voltage potential to prevent arcing between the two actuators. The actuators are arranged such that they act in the same streamwise direction as one another, thus directing flow outward and producing a jet.

The use of plasma actuators in small thrusters for micro and nano aerial vehicles (μAVs and nAVs, respectively) is examined here. The range of Re is very small and the subsequent aerodynamics are in a region of relatively unknown physics. Development of suitable propulsion systems will involve the integration of a reliable power source with sufficient energy and power density to carry out a mission. The propulsion system must be capable of demonstrating highly efficient conversion of stored energy to thrust to propel the vehicle in both hover and forward flight. Thus, highly efficient actuators are required for nano air vehicle designs.

This paper consists of the extended use of plasma actuators in a thruster configuration to produce a micro jet. An annular plasma actuator wherein the external electrode takes the place of the conventional embedded electrode is used to drive an internal flow, as can be seen in Fig. ??. This results in a zero-net mass flux micro thruster with no moving parts.

II. Experimental Arrangement

The plasma actuator configuration investigated here is used to produce a jet shown in Fig. 2. Teflon tubes of various diameters and thicknesses were used with 1.27 cm thick copper tape to create these actuators. A schematic of this configuration can be seen in Fig. 1. A power supply with about 50 W and 30 V input is connected to the actuator through a series of transmitters and capacitors on a Minipuls2 Circuit Board by Electrofluid Systems. An input signal in the form of a square wave and frequency range of 5-30 kHz is generated by a program in Labview and provided to the actuator by a data acquisition unit. Fig. 2 shows the end view of the actuator and the plasma ring created on the interior during actuation.

(a) Side view
(b) Front view
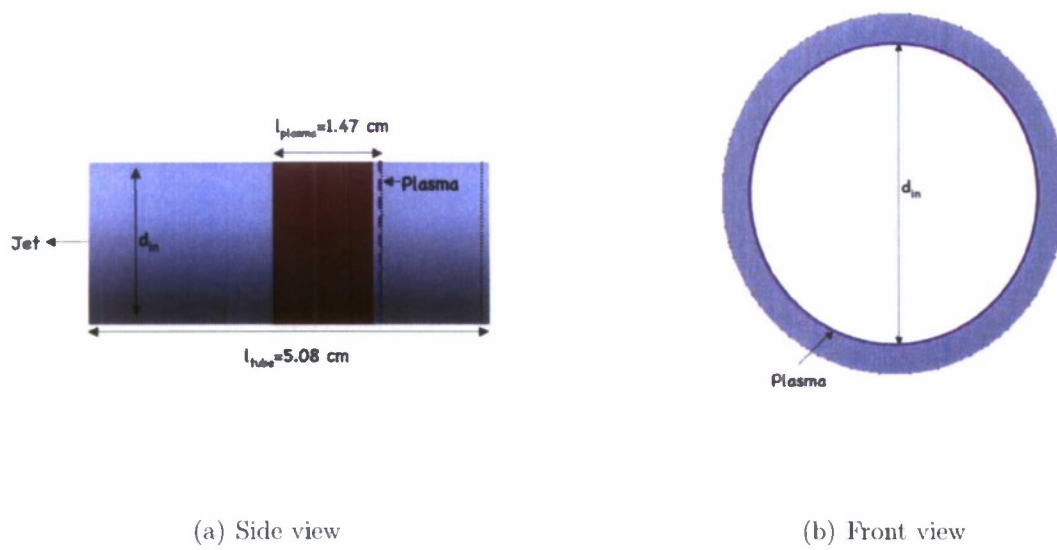
Figure 1. Front & side views of the plasma thruster.
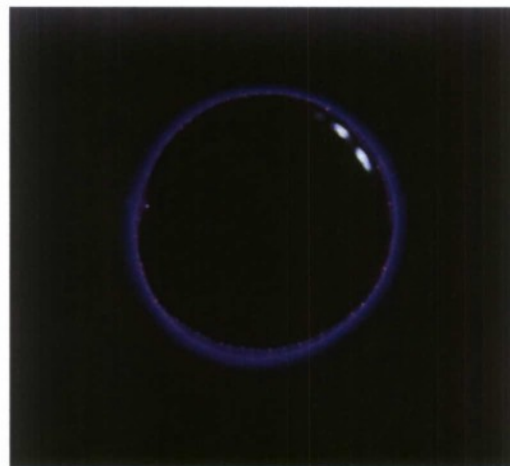
Figure 2. End view of the plasma on the interior duct wall.

The induced velocity of the jet was measured in a quiescent environment with a PIV system, shown in Fig. 3. Components include a monochrome Kodak Megaplus ES 1.0 CCD camera with a resolution of 1008 x 1018 pixels and a double exposure capability to capture an image pair within a small period of time, a dual-head Nd:YAG laser from Big Sky Lasers, a Quantum Composer timing box that controls and synchronizes the camera and laser heads, an oscilloscope to monitor timing of the laser pulses, a fog generator to introduce particles into the flow field, optics for laser sheet generation, a computer with frame grabber hardware (PIXCI D) and software (XCAP) for image acquisition and finally, PIV processing software

as discussed below.
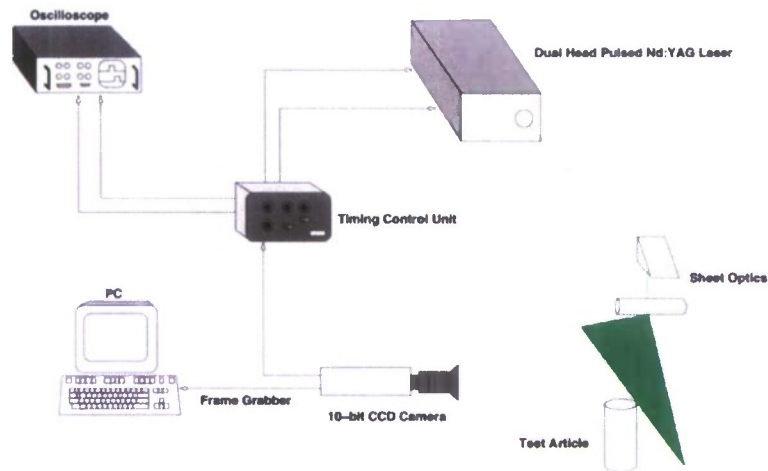
Figure 3. Schematic of PIV setup.
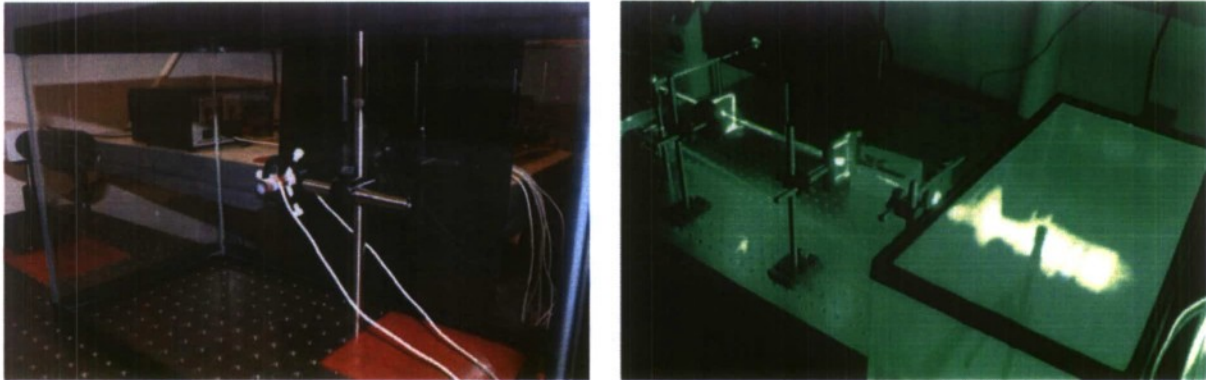
Figure 4. PIV setup.

To acquire PIV measurements, a transparent box containing the actuator is seeded with smoke particles on the order of 1 micron in diameter. A 2-D light sheet is projected in the vertical plane through the center of the circular tube using the Nd:YAG laser as seen below in Fig. 4. The timing control unit is used to pulse the lasers in synchronization with the CCD camera. The vertical field of view is approximately 6.225 cm with a resolution ranging from 150 pixels/cm to about 175 pixels/cm. Epix frame grabbing hardware and software is used to acquire binary image pairs. For each run, 191 image pairs were captured at a rate of approximately 15 Hz and these images were processed using the algorithm given below. The velocity and vorticity fields obtained in post-processing were then averaged over the data set. The PIV algorithm utilizes the wall adaptive Lagrangian particle-tracking algorithm (WaLPT) developed by Sholl and Savaş.[14] This algorithm treats the seeding as fluid particles and determines their translations and deformations. Fluid parcels registered

by CCD pixels are advected with individually estimated velocities and total accelerations. A standard DPIV algorithm is employed to determine the initial velocity field, and the routines in WaLPT allow for highly accurate measurement of the velocities near surfaces by mirroring the flow about the wall using an image parity exchange routine.[15] Velocity and vorticity are calculated as part of the PIV algorithm and scaled accordingly; vorticity is determined spectrally and does not suffer from typical numerical differentiation problems.

III.   Results & Discussion

The micro thruster capabilities of the plasma actuator configuration shown in Fig. 2 were investigated by varying several important parameters in the tests: the inner diameter, forcing frequency and the duty cycle. The thrust obtained is dependent upon the area of the jet, density of the air and the square of the velocity. Thus, the velocity induced by the actuator was measured by PIV in order to get transient & averaged results. Laser flow visualization was also utilized to observe detailed flow structure. In Fig. 5(a), multiple vortex rings immediately after pulsed actuation can be seen. During this pulsed plasma actuation, the vortex rings evolve into a turbulent jet as in Fig. 5(b) and (c).

The first set of runs were carried out using three cylindrical tubes of d_i=0.635 cm, d_i=1.016 cm and d_i=1.27 cm inner diameters having the same length of ℓ=5.08 cm and t=0.127 cm thickness. This thruster configuration was tested for 50% DC at plasma waveform frequencies of 5000 Hz and different modulation frequencies of 1 Hz, 2 Hz, 5 Hz, 10 Hz, 100 Hz and 500 Hz for a single diameter. The same procedure was repeated for the other two thrusters with all other parameters identical. One other set of runs consisted of varying only the duty cycle to observe its effect on the velocities induced. All three tubes of different diameters were tested for DC values of 100%, 90%, 50% and 10% for several cases of constant forcing frequency. The data obtained for the induced velocity was used to calculate the thrust for these tubes. Then, the thrust, maximum velocity and mean velocity were plotted against the forcing frequencies for 50% and 10% duty cycles. Three larger tubes of diameters d_i=1.524 cm, d_i=2.159 cm and d_i=3.048 cm were included in the analysis of the velocity profiles so that the influence of the (ℓ/d_i) ratio could be observed more clearly. Note that even though the length of these tubes are the same, the thickness varies for the largest three.

Downstream variation of the maximum and mean velocities for steady runs and different diameters is shown in Fig. 6. The effect of pulsing with different forcing frequencies on these velocities can be seen in Fig.freq. Note that the curves for different diameters are offset for clarity. The velocities increase, reach their peak value, then decrease for all three tubes. However, it is observed that the maximum velocity changes in the range of 50 cm/s
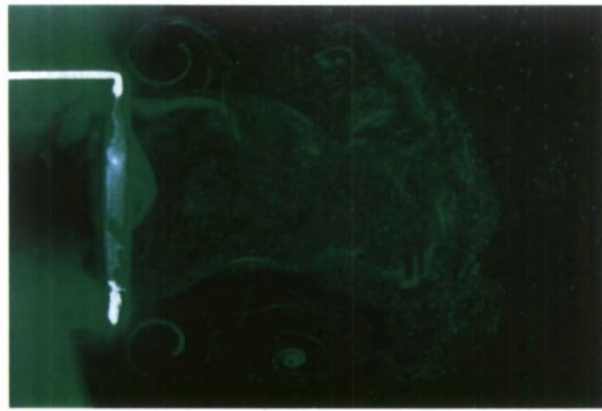
(a) Vortex rings following pulsed actuation
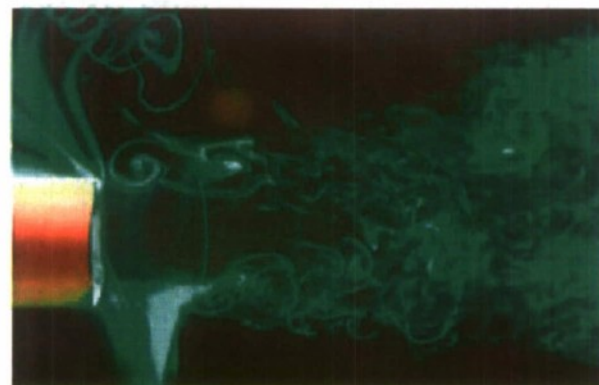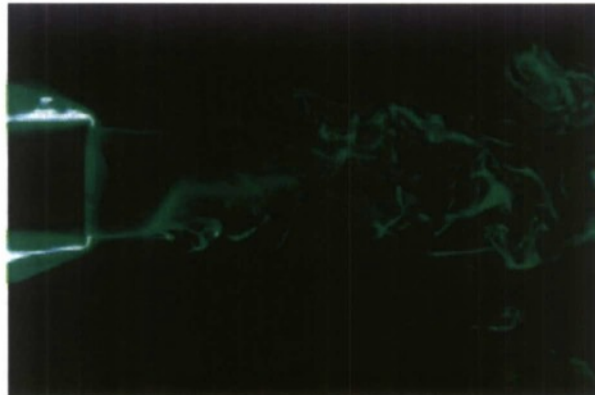
(b) Formation of the turbulent jet as vortex rings
evolve

Figure 5. Qualitative flow visualization of the flow structure using laser sheet illuminated smoke particles.

and 120 cm/s for the 1.27 cm diameter tube for all frequencies whereas for the 1.016 cm diameter tube, the limits of the range have decreased; they are between about 15 cm/s and 45 cm/s. What is interesting to note is that the maximum velocity distribution of the 0.635 cm diameter tube differs significantly from the other two. The values are in the range of 20 cm/s and 100 cm/s and are much higher than that of the 1.016 cm diameter. The average

velocity distribution for all three tubes follow the same trend but the limits are the highest for the 1.27 cm, 0.635 cm and 1.016 cm diameter tube respectively.
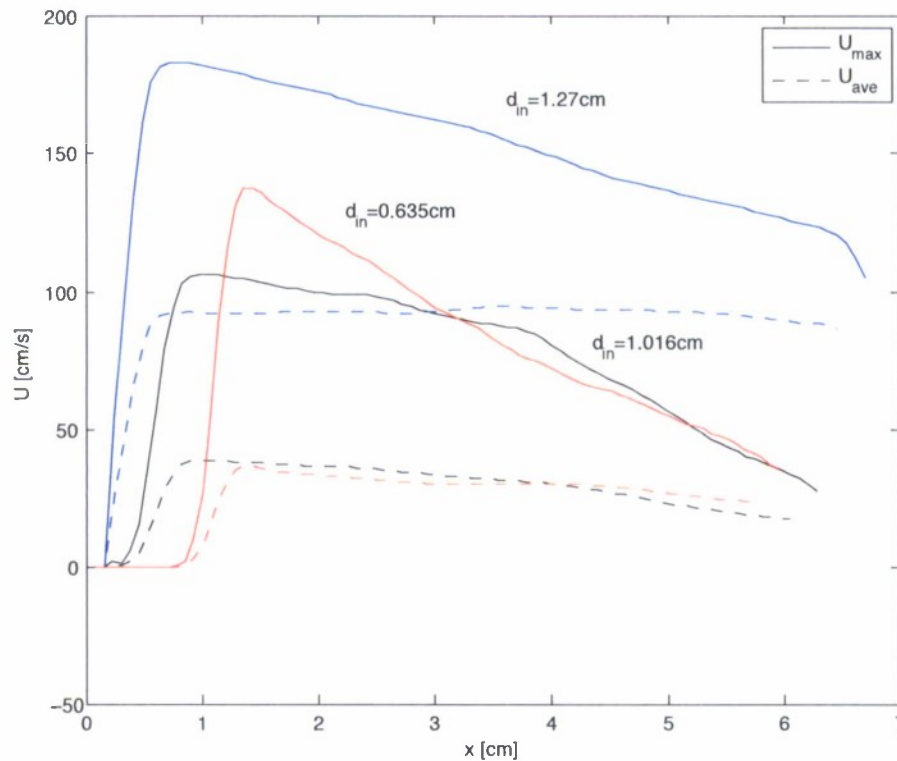
Figure 6. Maximum & mean velocities for tubes of inner diameter 1.27 cm, 1.016 cm and 0.635 cm with 100% DC.

Fig. 8 reveals the effect of changing the duty cycle on the maximum and mean velocity. It is clear that increasing the duty cycle results in higher velocities. In Fig. 8(a) and (b), it can be seen that all plots are similar. This suggests that the distribution of the velocities are dependent upon the (ℓ/d_i) ratio. A considerable increase in the maximum velocity for the 50% DC case can be observed. It can then be said that the effect of the forcing frequency is reduced at higher duty cycles. Fig. 8(c) presents the effect of 10% DC, the resulting velocities are very low relative to the 50% and steady cases. It could also be seen from Fig. 8(d) that the values of both the maximum and the average velocities increase for the 1.27 cm diameter tube.

Comparisons for the thrust, maximum velocity and mean velocity distributions for the three diameters at 50% DC can be observed in Fig. 9. The 1.27 cm diameter tube provides the largest thrust; a peak value of 1.174 mg at 100 Hz. The maximum thrust value for the 1.016 cm diameter tube is 0.284 mg at 5 Hz, while for the smallest diameter of 0.635 cm, this value goes down to 0.00977 mg at 100 Hz. It can be seen that there is a considerable
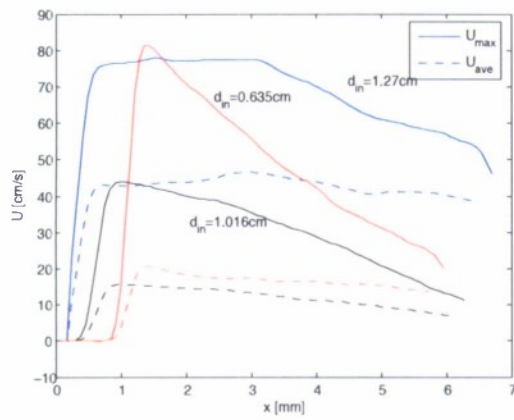
(a) f_p=1 Hz
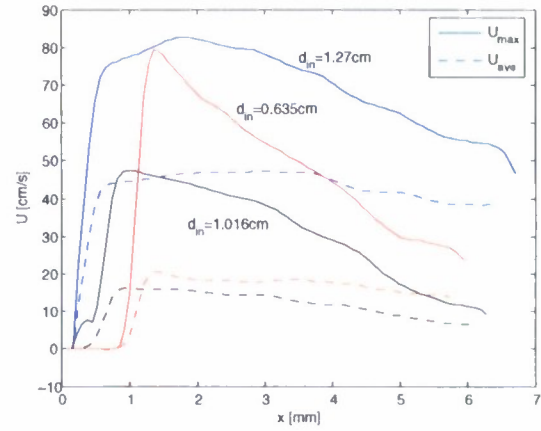
(b) f_p=2 Hz
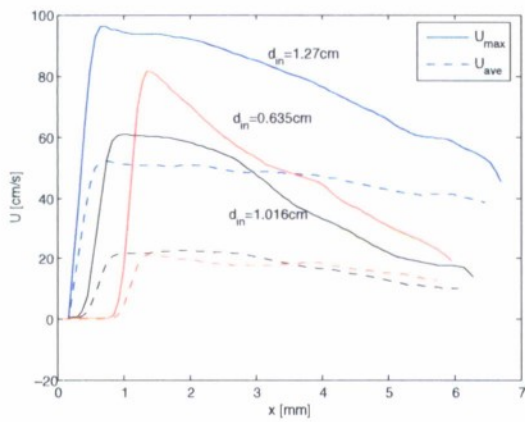
(c) f_p=5 Hz
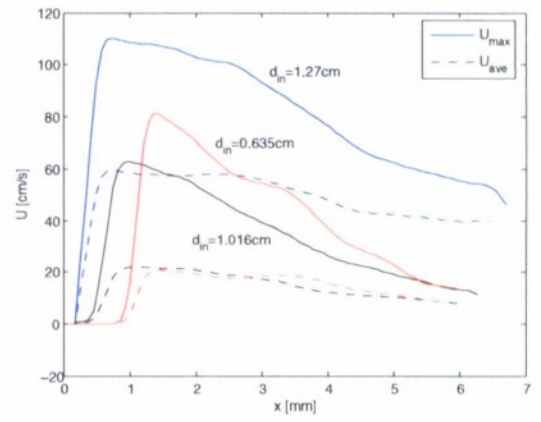
(d) f_p=10 Hz
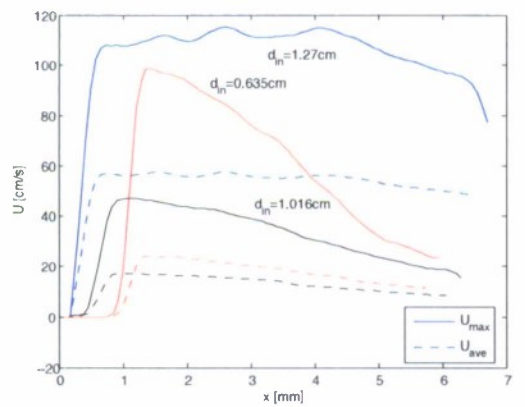
(e) f_p=100 Hz
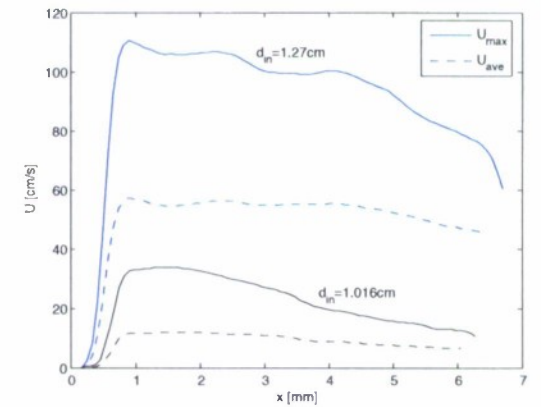
(f) f_p=500 Hz

Figure 7. Maximum & mean velocities for tubes of inner diameter 1.27 cm, 1.016 cm and 0.635 cm.
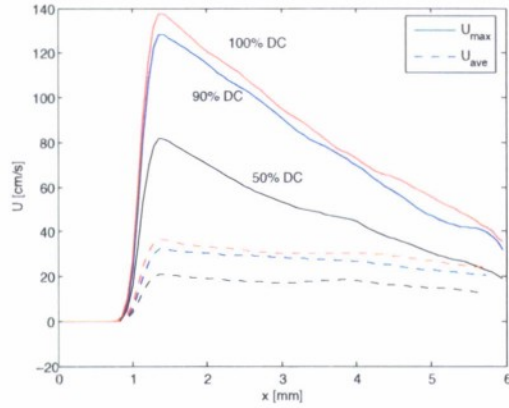
(a) d_i=0.635 cm; fp=5 Hz
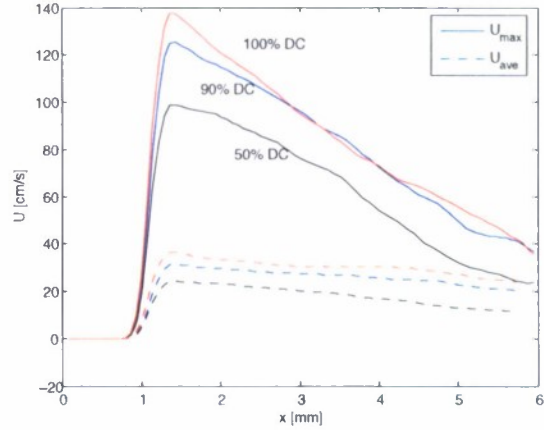
(b) d_i=0.635 cm; fp=100 Hz
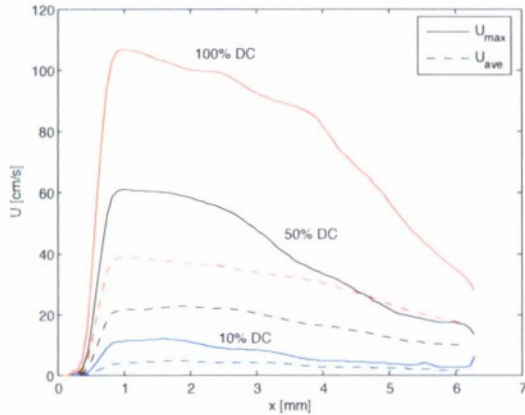
(c) d_i=1.016 cm; fp=5 Hz
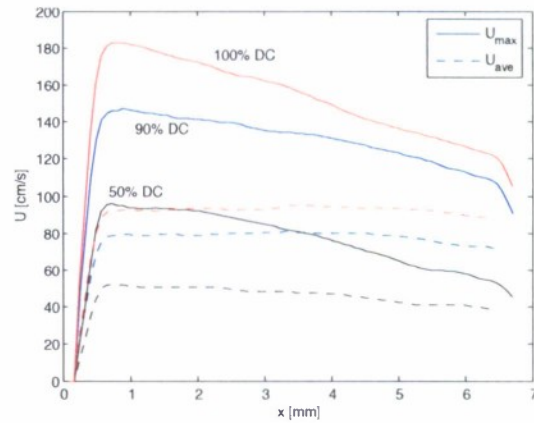
(d) d_i=1.27 cm; fp=5 Hz

Figure 8. Effect of DC on the maximum & mean velocity distribution.

amount of drop in the thrust as the (ℓ/d_i) ratio increases. This is not the case for the velocity distributions though, as the maximum velocity for the 0.635 cm diameter tube is greater than that of the 1.016 cm diameter tube; having values of 98.66 cm/s and 62.92 cm/s respectively. The average velocities of these two diameters are very close, which can be explained by the fact that the smaller diameter has a "peakier" velocity profile while the larger diameter tube has a broader profile.

Fig. 10, 11 and 12 consist of these distributions at 50% DC for each diameter separately. For the 0.635 cm diameter tube in Fig. 10, the peak values of thrust, maximum and mean velocity occur at 100 Hz; 0.00977 mg, 98.66 cm/s and 15.77 cm/s respectively. Even though the maximum values occur at the same point, the distribution of the thrust, maximum and mean velocity with the frequency differs. Similarly, the values obtained for the 1.016 cm diameter tube are as in Fig. 11 with 0.284 mg of maximum thrust and 16.76 cm/s of peak
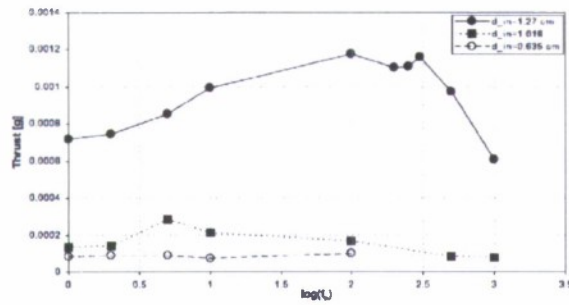
(a) Thrust vs. forcing freq.
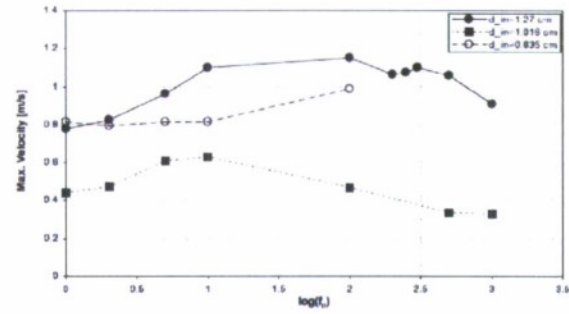
(b) Max velocity vs forcing freq.
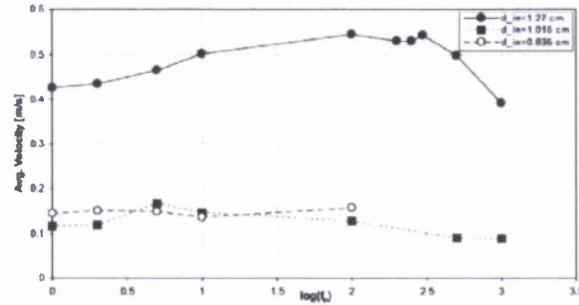
(c) Avg. velocity vs. forcing freq.

Figure 9. Thrust, maximum velocity and mean velocity distribution with forcing frequency at 50% DC.

average velocity at 5 Hz, whereas the peak for maximum velocity is 62.92 cm/s at 10 Hz. Fig. 12 reveals the 1.27 cm diameter tube and its distribution for the thrust, maximum and mean velocities. The peak values are found to be 1.174 mg, 115.12 cm/s and 54.48 cm/s respectively at 100 Hz.

The velocity profiles for all six tubes were plotted for different downstream values and compared to one another to see the effect of the (ℓ/d_i) ratio. For tests conducted at a forcing frequency of 5 Hz and 100% DC, it can be seen that the effect of the inner diameter is significant. In the first three cases, Fig. 13(a), (b) and (c), where the diameters are smaller, the profile is nearly parabolic with the maximum velocities occurring near the centerline. As the diameter is increased, high velocities are observed in the near wall regions and the centerline velocities are reduced, although they are still considerably large. These profiles at Fig. 13(d) occur at downstream locations close to the actuator; the flow starts to develop at further downstream locations. For the last case in Fig. 13(e) and (f), the velocities are highest near the walls, leaving the centerline velocity very low throughout the flow field. Note that for the largest diameter examined, a recirculation region with negative velocity is seen at the center of the tube.[16]

Velocity contours and streamlines obtained via PIV detail the difference in the flow field for decreasing the length-to-diameter (ℓ/d_i) ratio from the tube of 1.27 cm inner diameter
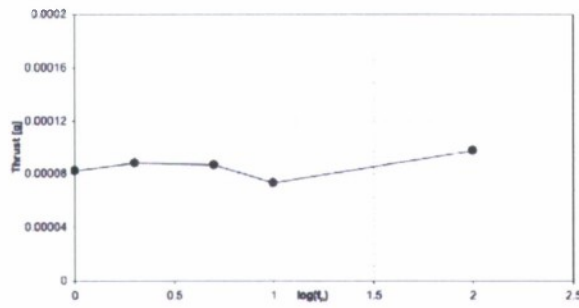
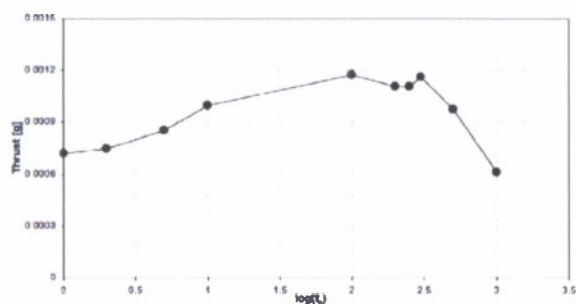(a) Thrust vs. forcing freq.
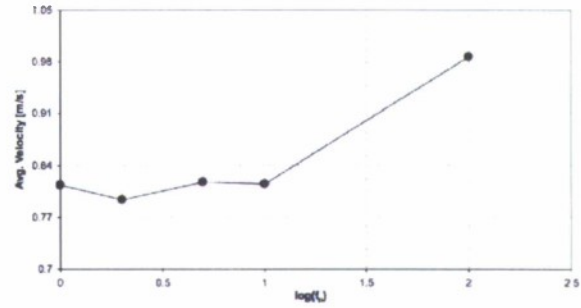
(b) Max velocity vs forcing freq.
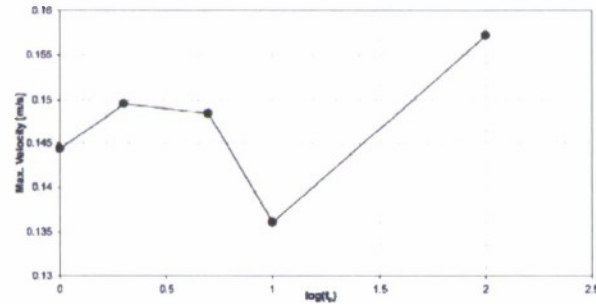
(c) Avg. velocity vs. forcing freq.

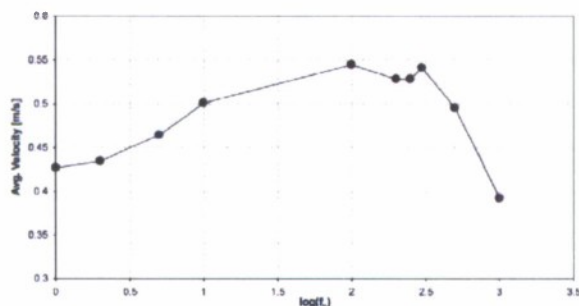**Figure 10. Thrust, maximum velocity and mean velocity distribution for d_i=0.635 cm.**

to the largest 3.048 cm diameter tube, shown in Fig. 14. The formation of the vortex ring during the initial jet stage and the evolution of the trailing jet for a given inner diameter can also be observed, shown in Fig. 15. To investigate how the jet is formed near the plasma, 2D models of the thrust configuration were generated using parallel plates since the teflon tubes are not transparent. While the ranges of values for aspect ratio are expected to be different between the 2D and axisymmetric cases, the formation of the basic structure is expected to be similar. Fig. 16 shows the results for 3 different plate gap widths (aspect ratios). In each case, one can easily see that the duct jet is formed by the characteristic plasma wall jet. For small distances between the plates (Fig. 16a correlating to high aspect ratio), the jets nearly interact directly with one another, even creating a small region of reverse flow immediately downstream of the wall jets. However, the main flow quickly develops into a parabolic profile. As the channel width increases, the jets become distinct from one another (Fig. 16b), resulting in a flow field similar to an annular jet. As the duct length increases, the flow field's double hump profile transitions to a single peak. At high channel widths (Fig. 16c), the wall jets become essentially independent and a reverse flow region forms in the interior region between the two.
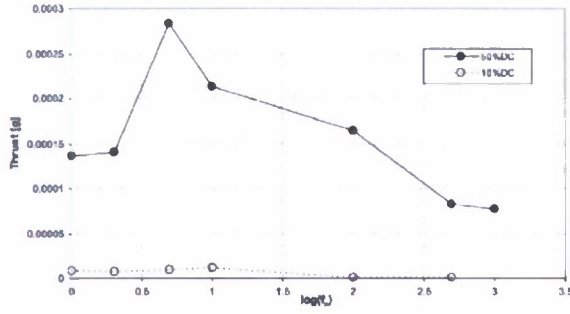
(a) Thrust vs. forcing freq.
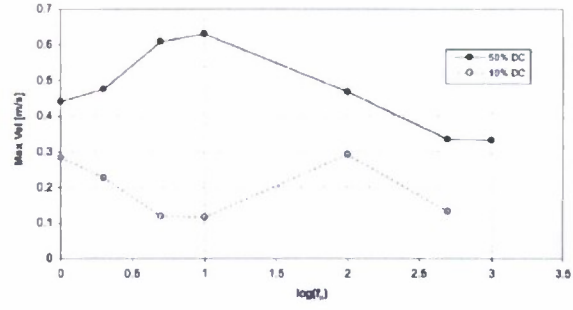
(b) Max velocity vs forcing freq.
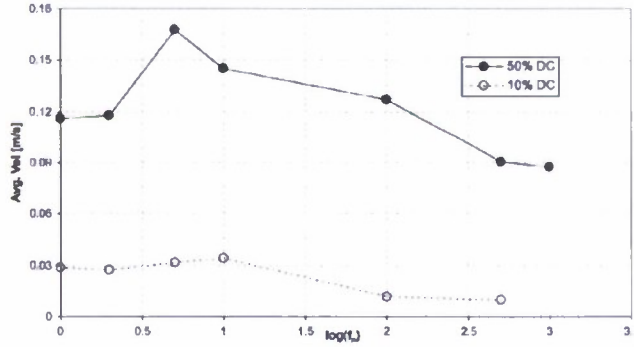
(c) Avg. velocity vs. forcing freq.

Figure 11. Thrust, maximum velocity and mean velocity distribution for d_i=1.016 cm.

IV.   Conclusions

Regarding initial tests, it could be concluded that the plasma actuator configuration investigated here can be used as a micro thruster. The results indicate that there should be optimum values to the varied parameters to obtain the most evenly distributed velocity profile and the maximum thrust. Of the three tubes of different ℓ/d_i ratios, it is observed that the tube with the largest diameter of d_i=1.27 cm induces the highest velocities although the 0.635 cm diameter tube does have greater maximum velocities then the 1.016 cm diameter tube. The average velocity distribution for these tubes are also very similar which shows that the flat profile of the smaller tube and the broader profile of the larger tube yield close average velocities. The thrust is the maximum for the 1.27 cm diameter tube and decreases with decreasing diameter, unlike the velocity. The effect of the duty cycle was investigated for each tube at different modulation frequencies. It was found that the velocities do increase with the duty cycle, but it was also seen that this effect decreases with increasing frequency. Peak values for thrust, maximum and average velocities all occur at different frequencies for each different diameter tube. For the 1.016 cm diameter tube, it was also observed that the peak for the maximum velocity occurs at a different forcing frequency than that of the thrust and average velocity raising a question to be answered with future work. The velocity

(a) Thrust vs. forcing freq.
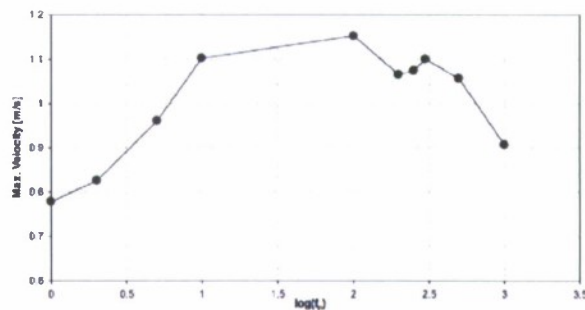
(b) Max velocity vs forcing freq.

(c) Avg. velocity vs. forcing freq.

Figure 12. Thrust, maximum velocity and mean velocity distribution for d_i=1.27 cm.

profiles for all six tubes of different diameters for a constant frequency and DC demonstrate the influence of the (ℓ/d_i) effect clearly, shown in Fig. 17. The profiles are nearly parabolic for the smaller diameter cases; the maximum velocities occur near the centerline. As the diameter increases, the centerline velocities are reduced and higher velocities can be seen in the near wall regions. For the largest diameters, the near wall velocities are the largest leaving very low centerline velocities in the flow field.
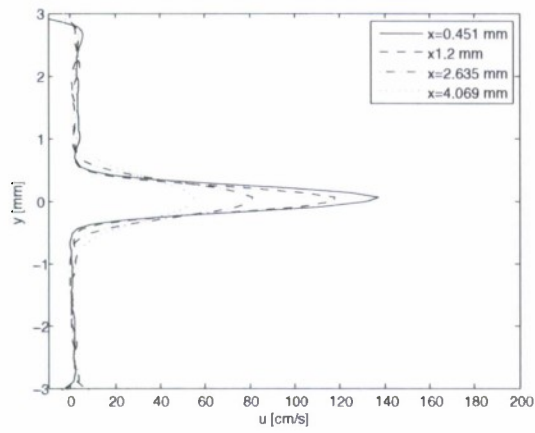
(a) d_i=0.635 cm
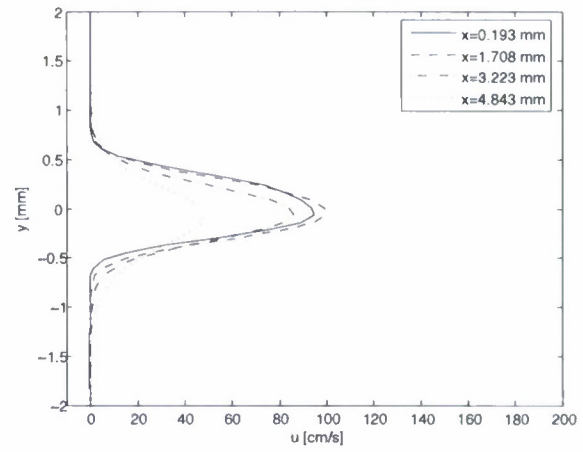
(b) d_i=1.016 cm
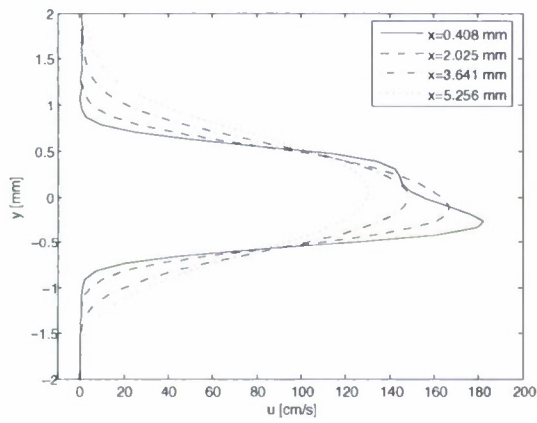
(c) d_i=1.27 cm
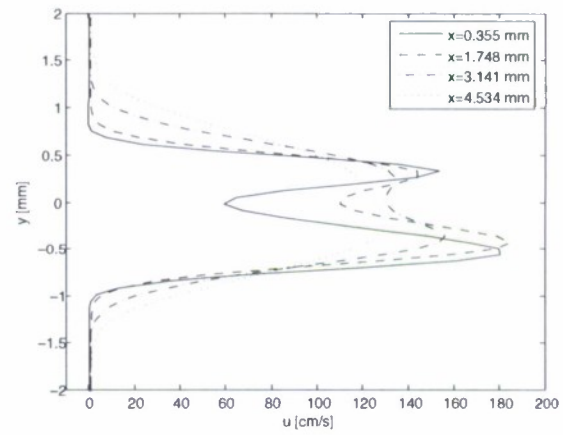
(d) d_i=1.524 cm
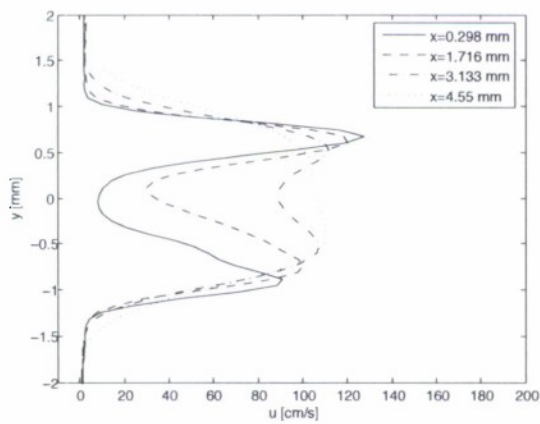
(e) d_i=2.159 cm
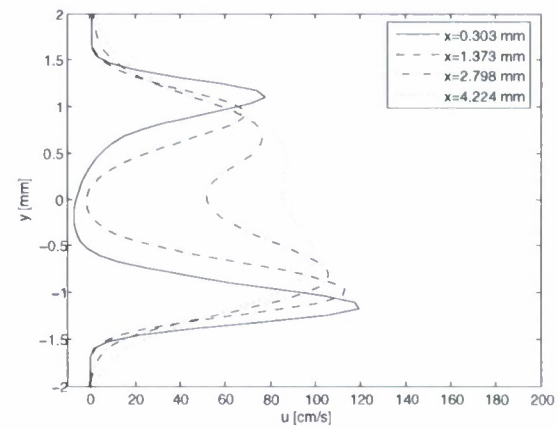
(f) d_i=3.048 cm

Figure 13. Velocity profiles at various downstream x-locations with 100% DC.

(a) d_{in}=1.27 cm   (b) d_{in}=3.048 cm
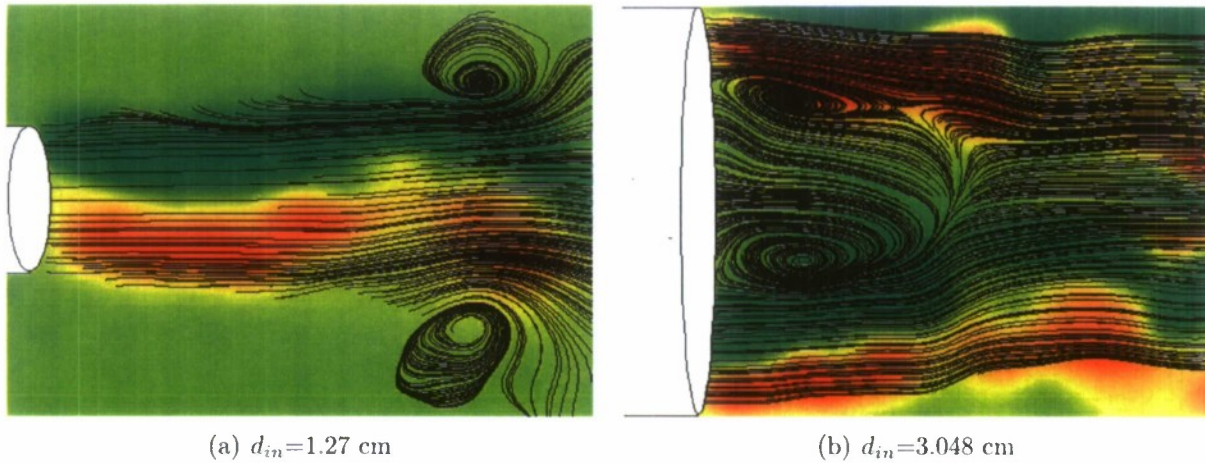
Figure 14. Streamlines for tubes of 1.27 cm and 3.048 cm inner diameters.

(a) t=50.084 s   (b) t=50.632 s   (c) t=51.179 s
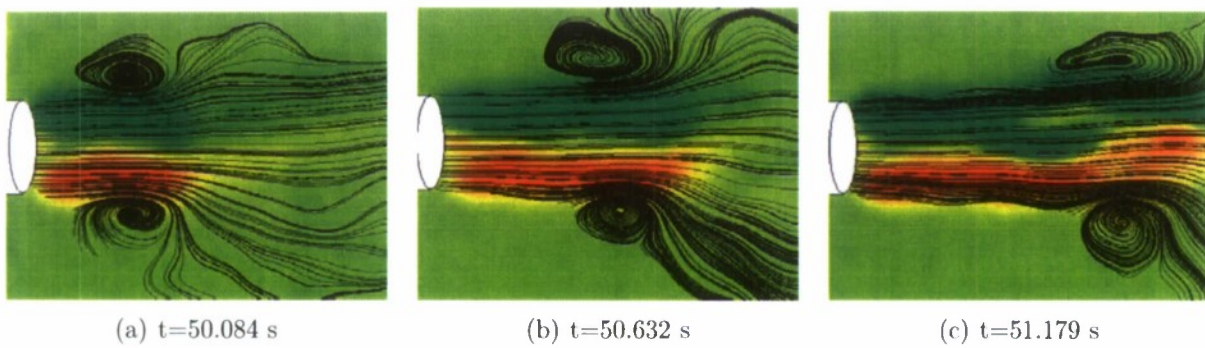
Figure 15. Formation and advection of vortex ring for the 1.27 inner diameter tube.
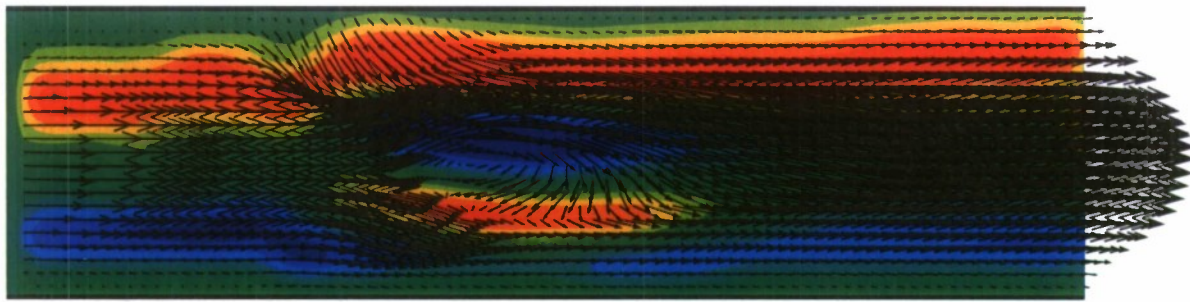
(a) High aspect ratio.
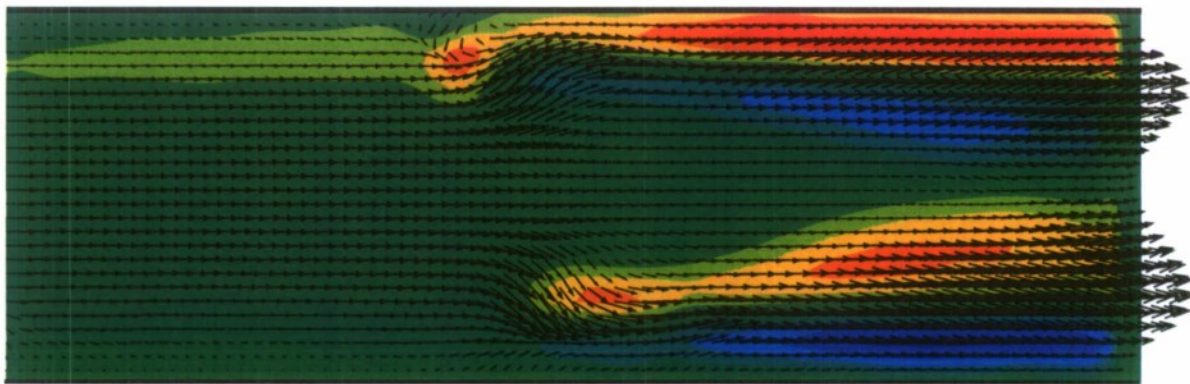
(b) Moderate aspect ratio.
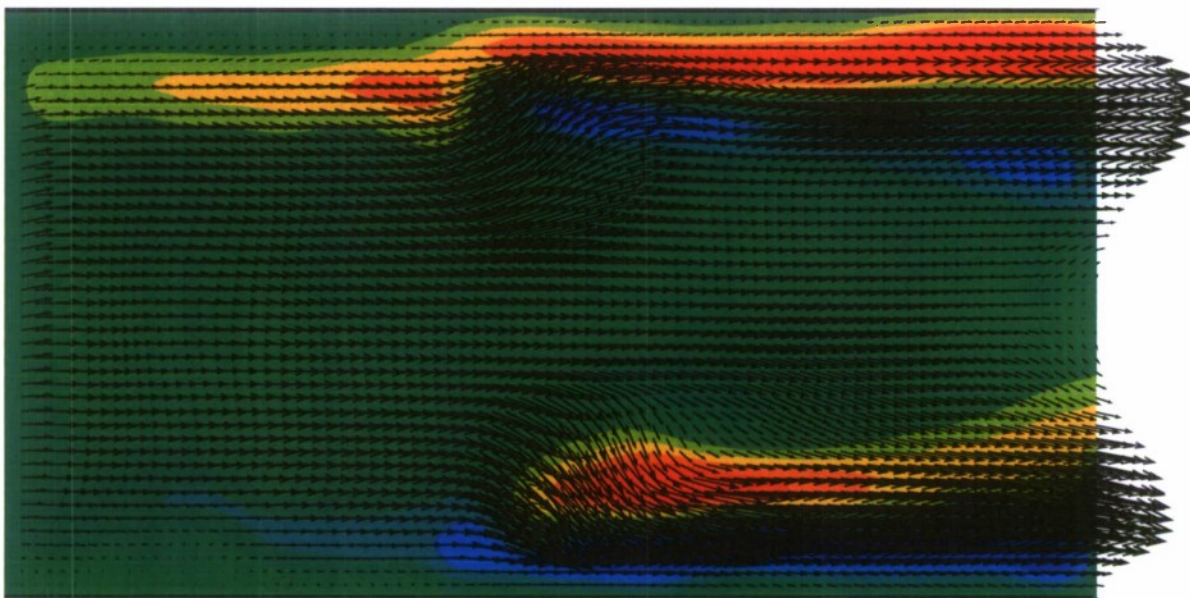
(c) Low aspect ratio.

Figure 16. Interior view of the jet formation using a 2D experimental model.
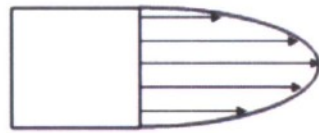
$(l/d_i) = 7.9$
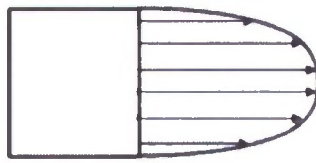
$(l/d_i) = 3.9$
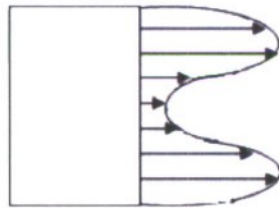
$(l/d_i) = 3.3$
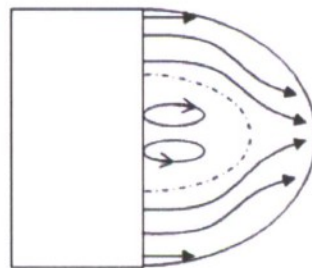
$(l/d_i) = 1.6$

Figure 17. Effect of length-to-diameter ratio on the velocity profiles.

References

[1]Santhanakrishnan, A. and Jacob, J. D., Flow Control with Plasma Synthetic Jet Actuators, J. Phys. D: Appl. Phys., Vol. 40, 2007.

[2]Santhanakrishnan, A. and Jacob, J. D., "On Plasma Synthetic Jet Actuators," AIAA Paper 2006-0317, 44th AIAA Aerospace Sciences Meeting and Exhibit, Reno, NV, Jan. 2006.

[3]Enloe, C. L., McLaughlin, T. E., VanDyken, R. D., Kachner, K. D., Jumper, E. J. and Corke, T. C., "Mechanisms and Responses of a Single Dielectric Barrier Discharge Plasma Actuator: Plasma Morphology," *AIAA Journal*, Vol. 42, No. 3, 2004, pp. 589-594.

[4]Enloe, C. L., McLaughlin, T. E., VanDyken, R. D., Kachner, K. D., Jumper, E. J., Corke, T. C., Post, M. and Haddad, O., "Mechanisms and Responses of a Single Dielectric Barrier Discharge Plasma Actuator: Geometric Effects," *AIAA Journal*, Vol. 42, No. 3, 2004, pp. 595-604.

[5]Labergue, A., Leger, L., Moreau, E. and Touchard, G., "Effect of a Plasma Actuator on an Airflow Along an Inclined Wall: P.I.V. and Wall Pressure Measurements," *Journal of Electrostatics*, Vol. 63, 2005, pp. 961-967.

[6]Roth, J. R., Sherman, D. M. and Wilkinson, S. P., "Boundary Layer Flow Control with a One Atmosphere Uniform Glow Discharge surface Plasma," AIAA Paper 1998-0328, 36th AIAA Aerospace Sciences Meeting and Exhibit, Reno, NV, Jan. 1998.

[7]Corke, T. C., Maltis, E., "Phase Plasma Arrays for Unsteady Flow Control," AIAA Paper 2000-2320, Fluids 2000, Denver, CO, June 2000.

[8]Porter, C. O., Baughn, J. W., McLaughlin, T. E., Enloe, C. L. and Font, G. I., "Temporal Force Measurements on an Aerodynamic Plasma Actuators," AIAA Paper 2006-104, 44th AIAA Aerospace Sciences Meeting and Exhibit, Reno, NV, Jan. 2006.

[9]Lopera, J., Ng, T.T., Patel, M.P., Vasudevan S. and Corke, T.C., "Aerodynamic Control of 1303 UAV Using Windward Surface Plasma Actuators on a Separation Ramp," AIAA Paper 2007-636, 45th AIAA Aerospace Sciences Meeting and Exhibit, Reno, NV, Jan. 2007.

[10]Likhanskii, A.V., Sheneider, M.N., Macheret, S.O. and Miles, R.B., "Optimization of Dielectric Barrier Discharge Plasma Actuators Driven By Repetitive Nanosecond Pulses," AIAA Paper 2007-633, 45th AIAA Aerospace Sciences Meeting and Exhibit, Reno, NV, Jan. 2007.

[11]Abe, T., Takizawa, Y., Sato, S. and Kimura, N., "A Parametric Experimental Study for Momentum Transfer By Plasma Actuator," AIAA Paper 2007-187, 45th AIAA Aerospace Sciences Meeting and Exhibit, Reno, NV, Jan. 2006.

[12]Bolzon, G., Zovatto, L. and Pedrizetti, G., "Birth of Three-dimensionality in a Pulsed Jet Through a Circular Orifice," Journal of Fluid Mechanics, Vol. 493, 2003, pp. 209-218.

[13]Glezer, A. and Amitay, M., "Synthetic Jets," Annual Reviews Fluid Mechanics, Vol. 34, 2002, pp. 503-529.

[14]Sholl, M. and Savaş, O., "A Fast Lagrangian PIV Method for Study of General High-Gradient Flows," AIAA Paper 1997-0493, 35th AIAA Aerospace Sciences Meeting, Reno, NV, Jan. 1997.

[15]Tsuei, L. and Savaş, Ö. "Treatment of Interfaces in Particle Image Velocimetry." *Experiments in Fluids*, **29**, pp. 203–214, 2000.

[16]Harlan, J. and Smith, D., "An Experimental Study of an Annular Jet with Zero Blockage Ratio," *60th Annual Meeting of the American Physical Society Divison of Fluid Dynamics*, Salt Lake City, Utah, November 20, 2007

Part II

High Speed Videogrammetry of Flapping Wings

I. Goals

The goal of this portion of the work is to investigate flapping wing flight and develop facilities and tools to study flexible flapping wing flight at the NAV scale, such as the compliant membrane wings of bats and flying squirrels. The complex fluid-structure interactions present in this type of natural flight provides an interesting problem for scientific study. This portion focuses on this area of natural flight and how to apply it to a man made NAVs.

II. Previous Work

Some of the earliest work performed in developing a flexible flapping wing MAV was done by Jones et al.[1] This study showed that the highest thrust created by the flexible flapping wing was at zero flight velocity. When properly designed and set up, this allowed the vehicle to hover. The amount of thrust created could only overcome the vehicle's drag profile at low flight speeds. They also showed that aeroelastic feathering led to more efficient flapping flight with a significantly larger thrust output. Work has also recently been done studying the effect of flexible airfoils in both fixed and flapping wing flight. Tamai et al. designed a fixed wing system with a flexible latex skin.[2] This system was tested at Reynolds numbers of 70,000. The flexibility of the wing was changed by varying the number of ribs used. PIV tests were then run at several angles of attack and compared with each other. The experiments showed that the flexible wings changed their shape to adapt to the changing airflow. At higher angles of attack, the wings deflected more in order to keep the flow attached longer. A higher L/D was seen for the more flexible wings.

Song and Breuer investigate the effects of aspect ratio and membrane tension of a fixed flexible membrane wing, using latex as well.[3] Using PIV and high speed stereogrammetry, they studied the effects of wing deflection on the flow field. It was shown that the wing actively changes camber based on Reynolds number and angle of attack. The aspect ratio also changed how the wing deflected along its span. Ol et al. performed a study of aeroelastic tailoring of highly flexible wings in flapping flight. The goal of this study was to develop an aeroelastically tailored wing allowing a man-made flapping wing MAV to hover. The study involved several flexible membrane wings with leading edge and diagonal spars. Each set of wings had the same basic layout with an aspect ratio of 2. However, the wings were made different sizes, to determine the effect of span on thin membrane aerodynamics. They discovered that the added degrees of freedom presented by the highly flexible wings can act like a spring when the wings change direction. This can add extra energy to the flow and produce a more useful aerodynamic performance.

Since Ellington's[6] research showed that quasi-steady analysis underpredicts the forces

generated in flapping flight, a large push has been made to understand the effects of unsteady aerodynamics on flapping wings. A breakdown of much of the research being done to study unsteady aerodynamic effects in flapping wing flight is presented by Viieru et al.[5] This paper presents an overview of the work currently being done in the area of low reynolds number aerodynamics, particularly in the fields of flexible fixed wing aerodynamics and unsteady studies in flapping wing aerodynamics. One of the main measures of the degree of unsteadiness in flapping flight is the Strouhal number, defined in Eq. 1 below. In this equation w is the flapping frequency, L is the mean wing chord, and U is the forward flight velocity. The effect of Strouhal number on thrust creation in flapping wing MAVs was investigated by Aditya et al.[7] This work studied at which Strouhal numbers the peak propulsive force occured for various configurations. It showed that the peak forces occur in a Strouhal number range from 0.1 - 0.4. The results also show a correlation between Strouhal number and flight velocity. At higher flight speeds, a lower Strouhal number provides optimum thrust, while at lower flight speeds, a higher Strouhal number is needed. This shows that more unsteadiness is utilized to maintain flight at lower speeds.

$$C_L = \frac{\omega L}{U} \tag{1}$$

Videogrammetry has been shown to be an effective means of measuring deflections in thin membrane structures. Leifer et al. show that a membrane under a 1 Hz oscillation with an amplitude of 1.5 mm can successfully be modeled using high speed videogramme-try.[8] Black et al. discuss a means of studying gossamer sails used in space application using videogrammetry.[9] This is important because the low mass and high flexibility of the structures doesnt allow instrumentation to be mounted on them. In instances such as this, videogrammetry provides an excellent means of studying the motion of the object without changing it. One of the most relevant applications of this technology to the area of flapping wing aerodynamics is being developed by Tian et al. at Brown.[10] This group has developed a high speed videogrammetry system to study live bats flying in a wind tunnel. This allows a study of natural thin-membrane flight in various flight modes. This study reveals that the slower that a bat is flying, the more complex the flapping pattern becomes.

III. Experimental Setup

A. Equipment

The ornithopter is a Flytech design based on a dragonfly. It has two upper wings and two lower wings mounted coincident with each other when viewed from above. In this experiment, however, only the upper wings are used. Only the frame and flapping mechanism from the

original system were used. In the unmodified off-the-shelf design, the ornithopter's flapping propulsion system was controlled via a RC controller with a throttle. The original motor was replaced with a more powerful model in order to increase the maximum flapping frequency that the system could realize. This new motor was relocated to the middle gear of the gearing system from the top gear in order to increase the maximum frequency as well. In order to gain a higher level of control, this motor was connected to a DC power source. The final alteration to the system was stiffening the frame of the mechanism with a .02 inch steel sheet in an effort to minimize inertial forces from non-wing movements. The final flapping device can be seen in Fig. 1 below.
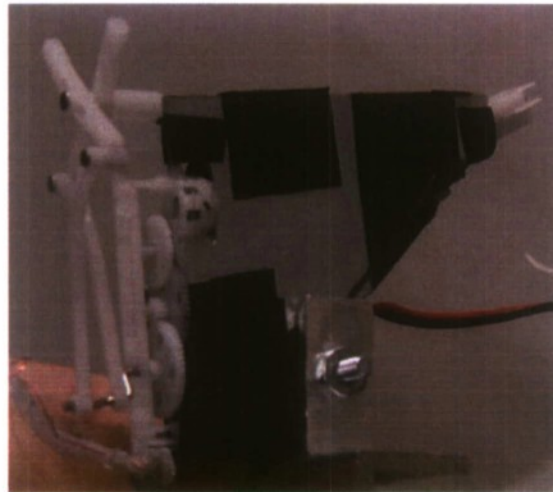
Figure 1. Flapping mechanism.

To test the effects of wings flexibility in flapping wing flight, ten sets of wings of varying flexibility were developed. The wings have a semispan of 73 mm and a chord of 30 mm. The wings have a rigid leading edge with a flexible membrane attached to form the rest of the wing. The stiffening spars are made of .03 inch diameter carbon rods and the membrane is 2 mil polyethylene. Five basic wing skeletal designs were developed, and then constructed using two different methods. In the first method the wing stiffening spars were all attached only to the flexible membrane and allowed to move independently of each other. In the second design method, the stiffening spars were arranged in the same locations on the wing but were attached to each other, causing the wing to be slightly stiffer. The five wing designs as well as the numbering system that they will be referred to with can be seen in Fig. 2 below. To facilitate the videogrammetry measurements, the wings were marked with a grid of fiducial markers. The planform view of this can be seen in Fig. 3 below. The masses of each wing semispan can be seen below in Table 1 within $\pm$ 0.005 g.

A KineOptics Wind Tunnel Balance (WTB) 2.0 was used to measure lift and drag. This balance equips two Sensotec Model 11 250 gram load cells. The ends of each of the directional

Configuration Number	Planform View
1	
2	
3	
4	
5	
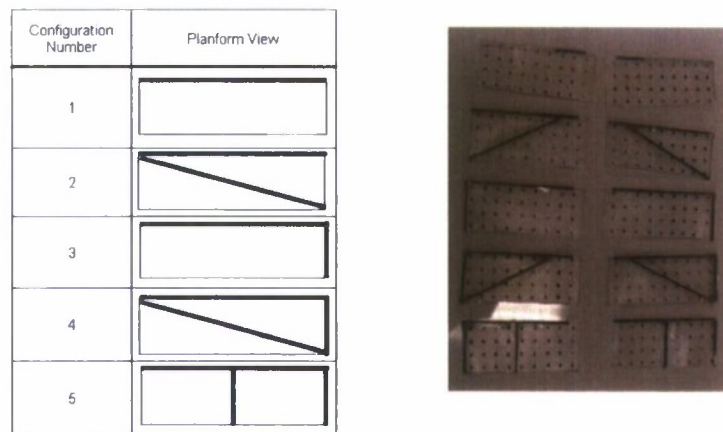
Figure 2. Wing configurations and numbering system.
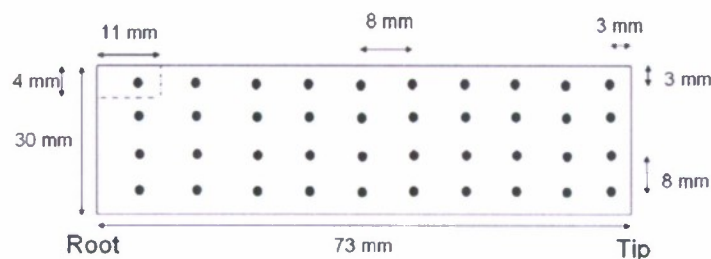
Figure 3. Wing fiducial marking system.

units has a flexure which is designed to transfer the loads to the load cells. Special magnetic rods are attached to the flexures at one end and the load cells at the other. These rods are designed to separate from the load cell to prevent an overload. Fig. 4 shows a side veiw of the balance system. The signal from the load cells was then run through a difference amplifier and the ouput to LabVIEW. LabVIEW data was recorded at a sample rate of 5000 Hz. Data analysis was handled primarily in Matlab and Excel. Two MotionPro X high speed cameras were used to record the wings. The cameras recorded at a frame rate of 1000 Hz. and a resolution of 1280x1024. The cameras were synched to the data via a trigger signal sent out by LabVIEW. Four 750 Watt bulbs provided light for the experiments.

B. Quiescent Flow Testing

Initial tests were performed in a quiescent flow environment. Experiments were run with each of the ten wing sets at five different flapping frequencies at a fixed angle of attack of 14 degrees. The target flapping frequencies were 20, 30, 35, 40, and 45 Hz. An aluminum frame was constructed in order to allow for the easy relocation of the cameras to various vantage points for the videogrammetry analysis. A model of the setup can be seen in Fig. 5 below.

Table 1. Wing mass breakdown.

Configuration No.	Wing Set 1 Mass (g)	Wing Set 2 Mass (g)
1	.325	.390
2	.495	.490
3	.395	.450
4	.425	.585
5	.525	.505
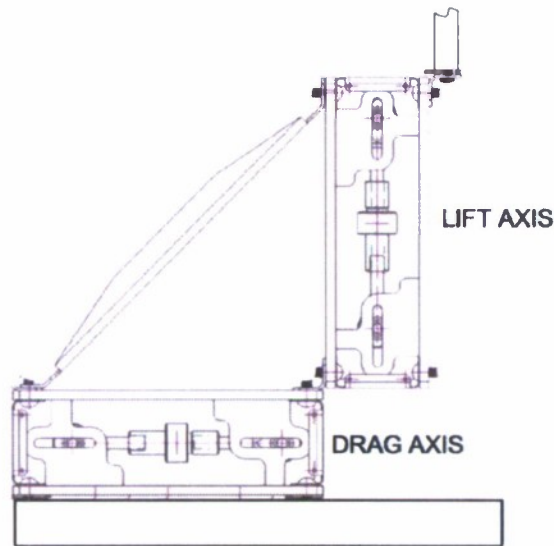
Figure 4. Force Balance Side View.

C. Wind Tunnel Testing

Three of the wing configurations from the quiescent flow tests were then chosen to be tested in a shear/gust tunnel developed in the lab specifically for the testing of MAVs.[11] The tunnel consists of a bank of miniature computer cooling fans assembled in a 10x11 grid. The fans are controlled by a DC voltage input and are set up for multiple rows to be controlled by a single voltage input. The setup allows for banks of 3, 2, 2, and 3 rows to be independently controlled, creating a wind shear. This is shown in Fig. 6a. The fans have 3 1/8 inch diameter blades with 42 CFM a nominal voltage. For these tests, all of the fans are set to 5V, which corresponds to a tunnel velocity of 5.2 m/s. The setup in the tunnel can be seen in Fig. 6b.

Figure 5. Quiescent flow setup.

Gust Tunnel Circuit Diagram
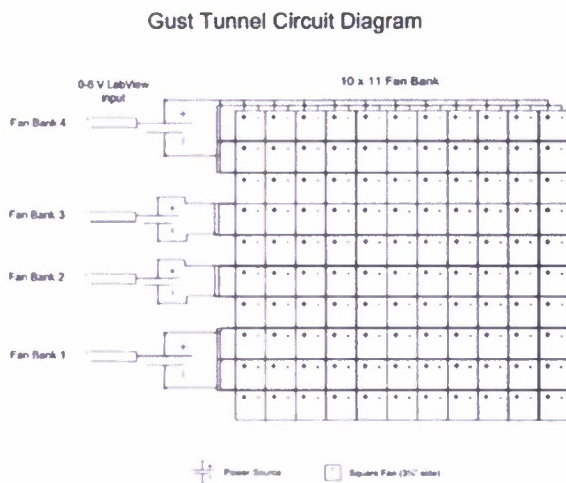
(a) Fan bank control grid.

(b) Model in wind tunnel.

Figure 6. MAV gust/shear tunnel.

IV.   Results

To determine which input voltages to use in order to get the desired frequencies, the device was run unloaded over a range of input voltages. The final input voltages and corresponding unloaded flapping frequencies can be seen in Table 2. The test matrix can be seen in Table 3.

This same numbering system was used for both wing configurations for ease of comparison.

Table 2. Input voltage v. flapping frequency.

Input Voltage (V)	Flapping Frequency (Hz)
5.0	19.23
7.5	29.41
9.0	34.48
10.0	40.00
11.5	45.45

A.   Quiescent Flow Tests

Each of the ten wing sets was tested at five different flapping frequencies. The target frequencies from an unloaded analysis were listed in Table 3 earlier. An analysis of the loaded frequencies revealed that the actual frequency realized by the system is always slightly lower than the target. The actual frequency remains linear and predictable for each wing configuration. Configurations 1 and 2 are the most heavily affected. This can be seen in Fig. 7 below. The chart shows the target frequency on the x-axis and the actual frequency on the y-axis.
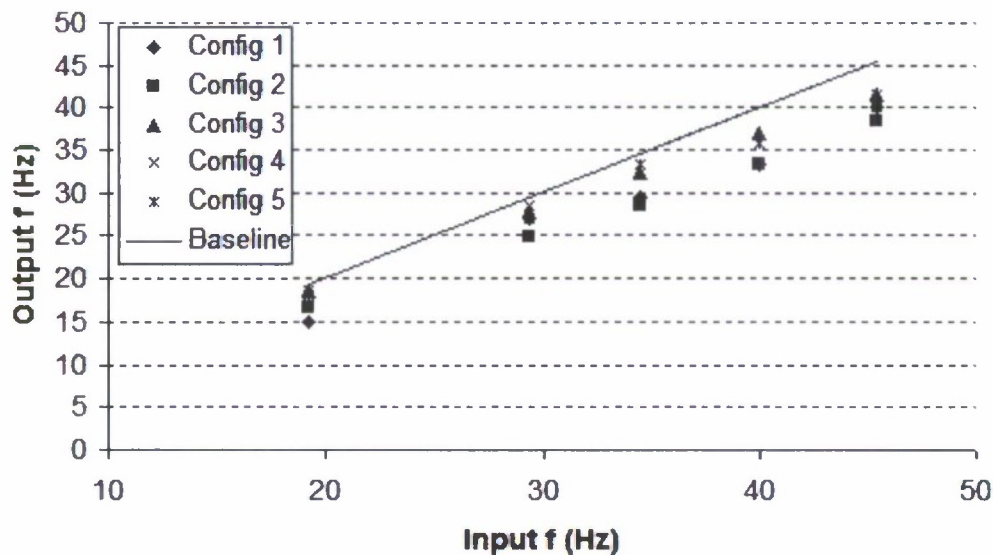
Figure 7. Comparison of target and achieved frequencies.

After the tests were run, the data was analyzed in several different ways. The first was to run it through a an FFT algorithm in MATLAB. This program outputs a power spectrum

Table 3. Test matrix.

Run Num.	Configuration Num.	Flapping Frequency (Hz)
1	1	19.23
2	1	29.41
3a	1	34.48
3b	1	40.00
3	1	45.45
4	2	19.23
5	2	29.41
6a	2	34.48
6b	2	40.00
6	2	45.45
7	3	19.23
8	3	29.41
9a	3	34.48
9b	3	40.00
9	3	45.45
10	4	19.23
11	4	29.41
12a	4	34.48
12b	4	40.00
12	4	45.45
13	5	19.23
14	5	29.41
15a	5	34.48
15b	5	40.00
15	5	45.45

graph which allows an analysis of the dominant frequencies that appear in both the lift and thrust forces. The frequencies that come out of this analysis are almost always either the flapping frequency or some whole number multiple of it. This analysis allows a study of how the wing flexibility affects the aerodynamic forces created during the flapping motion. The next test was to find the average period. This was accomplished using an Excel VBA code. The high speed video of each run was analyzed to find the beginning and end time of the first period. This is input into the Excel code. The first 25 periods are then plotted and compared with each other to make sure that they align properly. The average period of lift and thrust is taken from this analysis. A convergence plot is also checked at this point to make sure that the average data has converged or if more periods are required. An example of the power spectrum is shown below in Fig. 8. Notice that the flapping frequency of 17.025 Hz appears as the dominant frequency, and that there is a small peak at each multiple of that number until the fifth and sixth multiples. These higher frequencies are being excited by the flapping motion. An example of the convergence check is shown in Fig. 9 below. Notice that in this case, convergence is achieved in 15 periods. Finally, an example of the period alignment check is shown in Fig. 10 below. Notice that the periods remain in line with only small variations in time. Also, the higher frequencies that appeared on the FFT analysis are viewable in this average period. All of the above examples are from Run 7 of the second, more stiff, wing set.
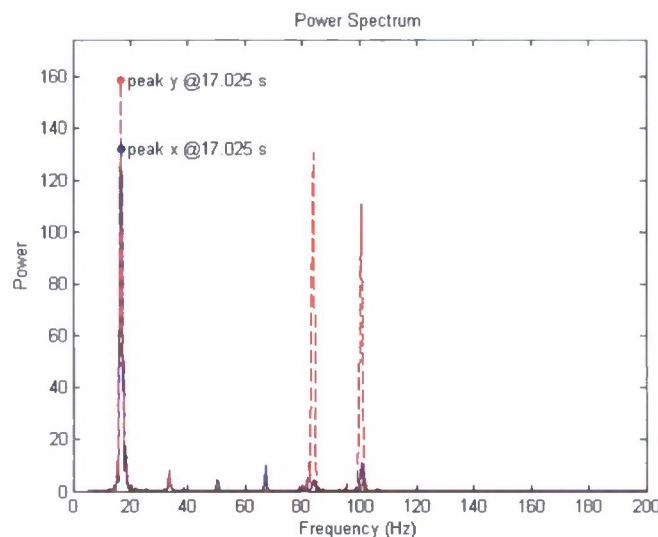
Figure 8. Sample power spectrum.

After the average period is calculated, the time averaged force over the average period is calculated. From this, the nondimensionalized lift and thrust are calculated using Eq. 2. Since this is a static test, the velocity is replaced with wc. The final analysis is removing
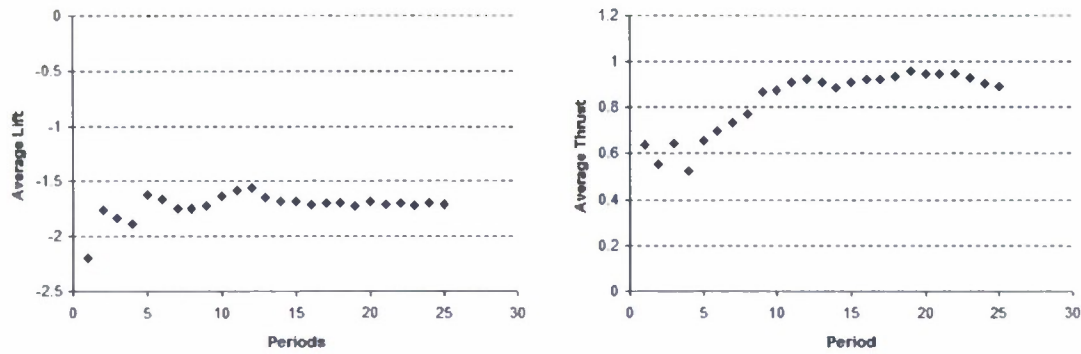
Figure 9. Sample convergence plot.
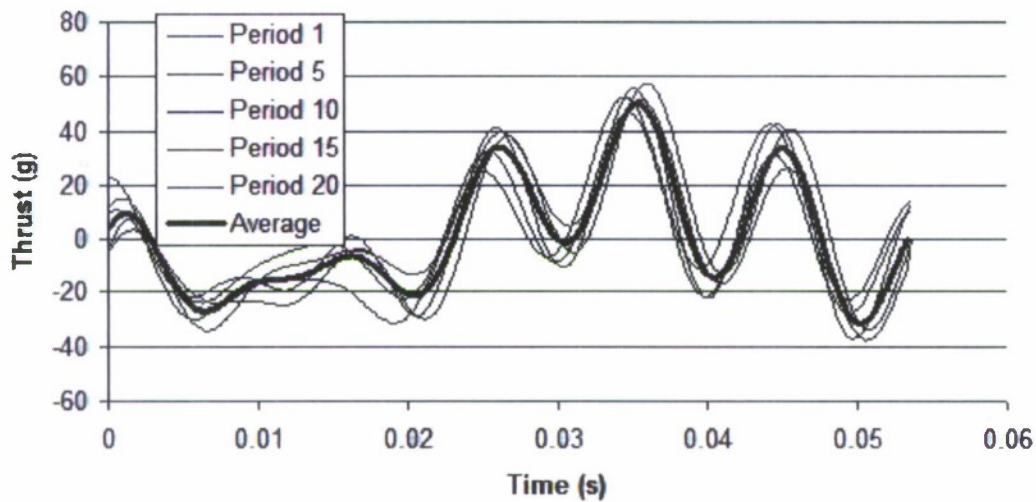
Figure 10. Sample average period check.

the inertial force data from the total force data, leaving only aerodynamic forces. The best way to accomplish this is by using a vacuum chamber to measure the inertial force and subtracting it from the total force. However, without a vacuum chamber to use, the best way is to use Eq. 3. This analysis can only be performed in the lift direction, since the wings are moving in a purely up and down motion. A typical comparison of measured force and aerodynamic force is shown below in Fig. 11.

$$C_L = \frac{2L}{\rho(\omega c)^2 S} \tag{2}$$

$$L = F_{meas} - md[\ddot{\Theta} sin\Theta + \dot{\Theta}^2 cos(\Theta)] \tag{3}$$
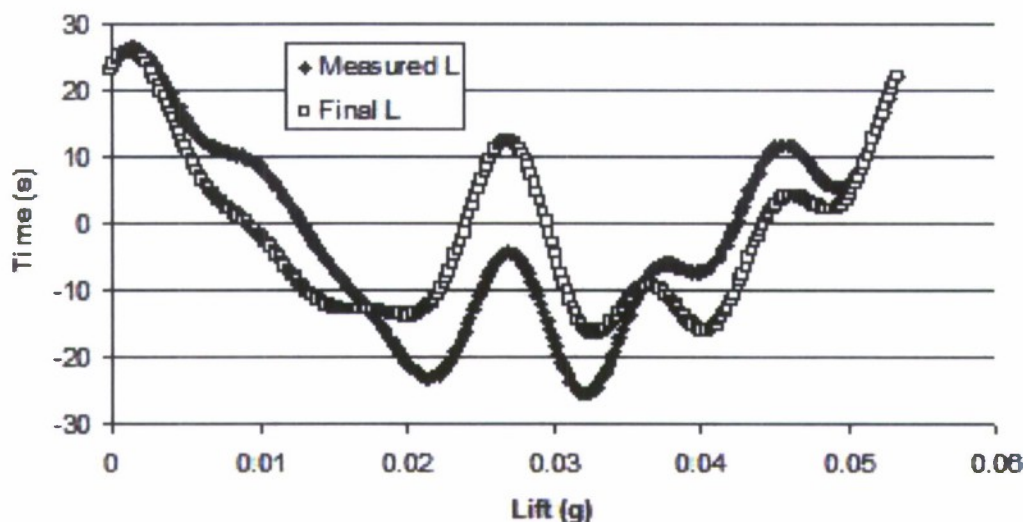
Figure 11. Measured lift v. aerodynamic lift.

After the time averaged lift and thrust coefficients were calculated, they were plotted against each other for comparison. The lift coefficients for wing set one are shown below in Fig. 12a and the thrust coefficients are shown in Fig. ??b. The lift and thrust coefficients for wing set two are shown below in Fig. 13a and Fig. 13b respectively. From this data, in wing set one, the lift data for configurations 1, 2, and 4 appear to be fairly linear with a few outliers. Only configuration 1 appears to consistantly have a positive lift. This could be from its ability to 'feather' during the upstroke, reducing negative lift. The thrust data appears to be more linear, but also more negative. For the lift data from wing set two, configurations 2, 3, and 5 appear to be linear, with configurations 1, 2, and 3 being mostly positive.

The final analysis performed was to analyze the runs using videogrammetry analysis. This analysis was performed using the PhotoModeler Video package contained within the photogrammetry software suite Photomodeler Pro. The goal of this analysis is to learn how the varying flexibility of the wings affects the aerodynamic forces measured. Fig. 14 below shows results from videogrammetry analysis of one period of a run of wing configuration 1. Notice the large deflections seen in the wing as it reaches its reversal points. This large deflection presents a problem to videogrammetry analysis. If the deflections are too large, it isn't possible to keep the points nearest the corner in view of both cameras throughout the entire flapping cycle. This program also outputs a text file of the 3-D location of each point at each moment in time. Fig.19 below shows the results of a MATLAB analysis of the results of this videogrammetry output. It shows a comparison of each of the 30 points with

each other in each of the three dimensions. It can be seen from looking at these figures that the wing doesn't deflect uniformly.

(a) C_L. (b) C_T.
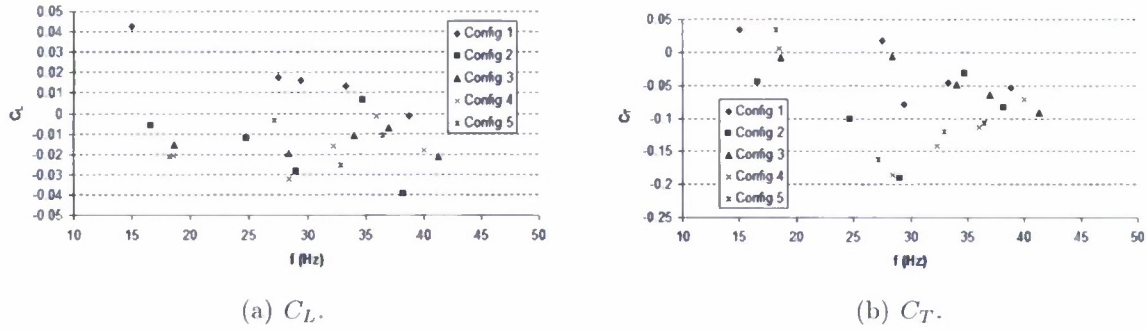
Figure 12. C_L and C_T v. f for gust/shear tunnel tests.

(a) C_L. (b) C_T.
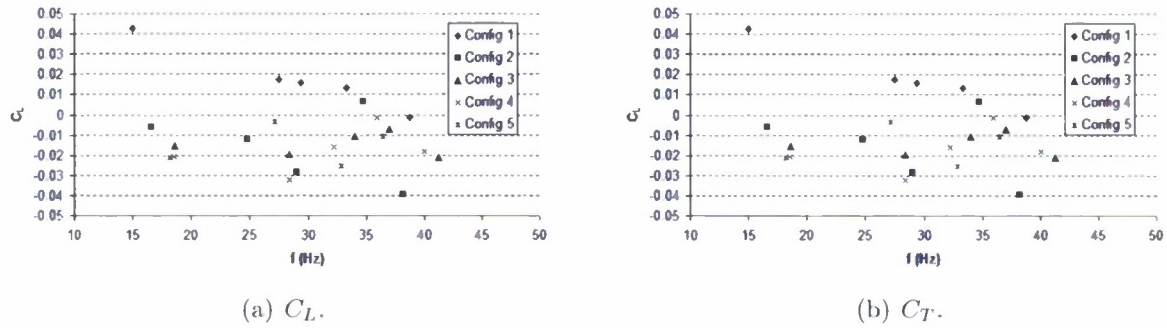
Figure 13. C_L and C_T v. f for gust/shear tunnel tests.

B. Wind Tunnel Tests

From analyzing the results of the quiescent tests, the decision was made to test configurations 1, 2, and 3 from wing set two in the wind tunnel. The tunnel was operated at a velocity of 5.2 m/s. The test matrix is shown in Table 4 below. Planform views of the three configurations used can be seen in Fig. 16. Before testing in the wind tunnel, the motor attachment was rebuilt to prevent slipping under high loads. This allowed the target frequency to be reached more accurately than in the quiescent flow tests. The comparison can be seen in Fig. 17 below.

Fig. 18a shows the nondimensionalized lift versus the flapping frequency for the wind tunnel tests, and Fig. 18b shows the nondimensionalized thrust. These values were obtained by taking the time averaged force over 25 flapping cycles and nondimensionalizing using Eq. 4 below. Inspection of these figures shows that the three wing sets are relatively similar at the lower flapping frequency. It can be inferred from this that flexibility effects are more prevalent at higher flapping frequencies. This can be seen by comparing Fig. ??a and Fig. ??b. From

| (a) t=0 s. | (b) t= 0.01 s. | (c) t= 0.02 s. | (d) t= 0.03 s |

| (e) t= 0.04 s | (f) t=0.05 s. | (g) t= 0.06 s | (h) t=0.07 s. |
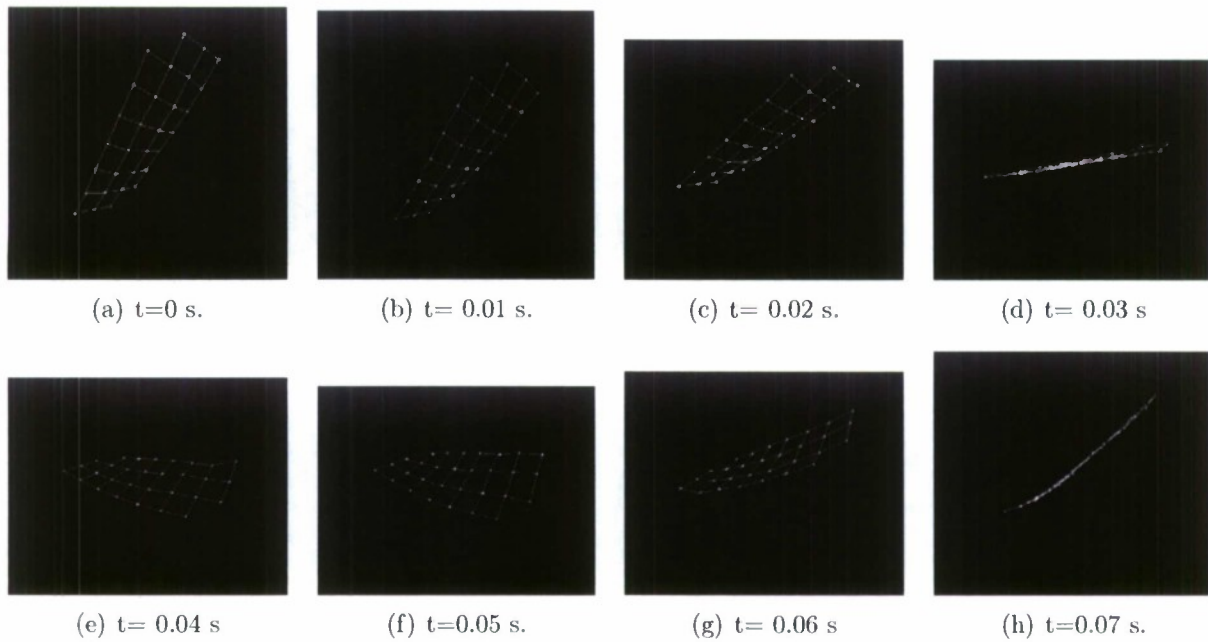
Figure 14. 3-D plots from videogrammetry analysis.

| (a) X-direction. | (b) Y-direction. | (c) Z-direction. |
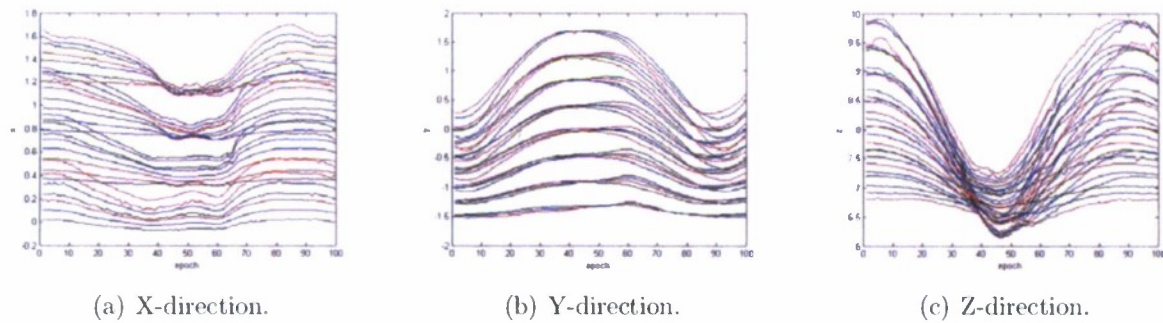
Figure 15. Plots of individual fiducial markers v. time in each dimension.

this it can be seen that at the higher flapping frequencies, the flapping frequency dominates. However, at lower flapping frequencies, several other frequencies appear in the data. From a look at the lift data, it appears that Configuration 2 is the superior design. This configuration consistently has a higher value of lift when compared with the other two configurations. When looking at the thrust data, it becomes apparent that a lower angle of attack might be needed to produce the necessary thrust for forward flight. This setup cannot produce sufficient thrust to overcome the drag inherent in the system.

$$C_L = \frac{2L}{\rho V^2 S} \tag{4}$$

Table 4. Test matrix.

Run Num.	Configuration Num.	Flapping Frequency (Hz)
1	1	19.23
2	1	29.41
3	1	34.48
4	1	40.00
5	1	45.45
6	2	19.23
7	2	29.41
8	2	34.48
9	2	40.00
10	2	45.45
11	3	19.23
12	3	29.41
13	3	34.48
14	3	40.00
15	3	45.45

Figure 16. Planform view of wings used in wind tunnel tests.

V.   Conclusions

Ten different designs of flexible membrane flapping wings were tested in a quiescent flow situation at five different flapping frequencies. The results of these tests show that flexibility and frequency both have a large impact on the aerodynamic forces created by flapping wings. In a static situation both lift and thrust appear to decrease with increased flapping frequency. Only in the case of the stiffest of the wing configurations was a marked positive slope realized.
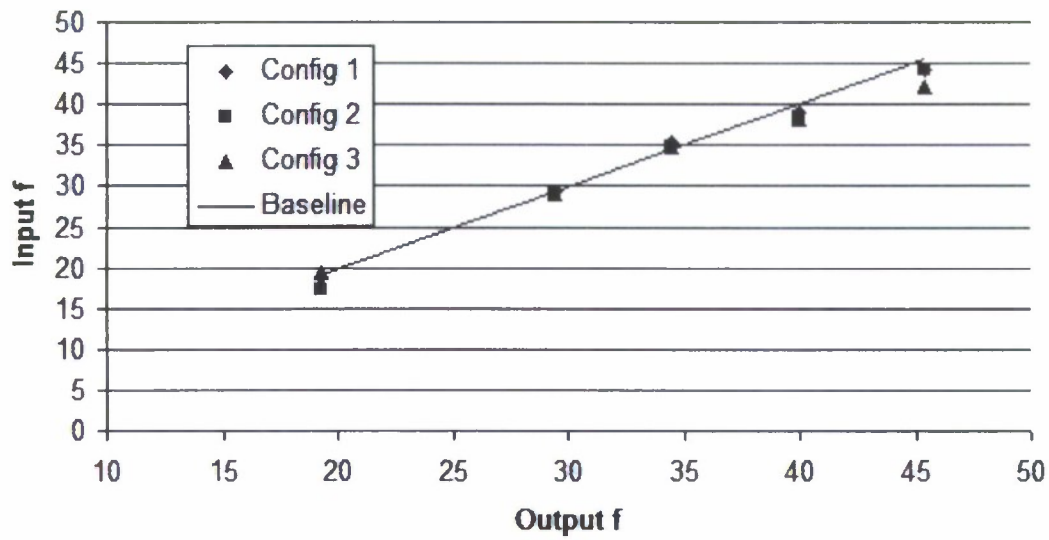
Figure 17. Comparison of target and achieved frequencies in the wind tunnel.
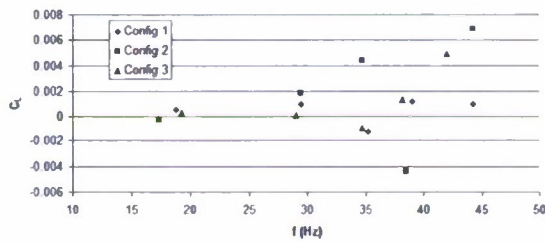
(a) C_L.
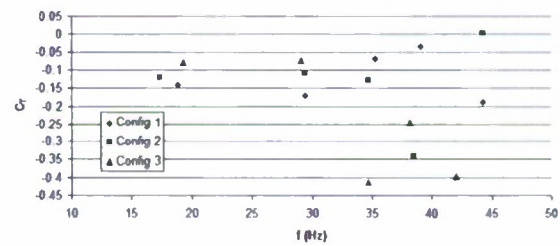
(b) C_T.

Figure 18. C_L and C_T v. f for gust/shear tunnel tests.
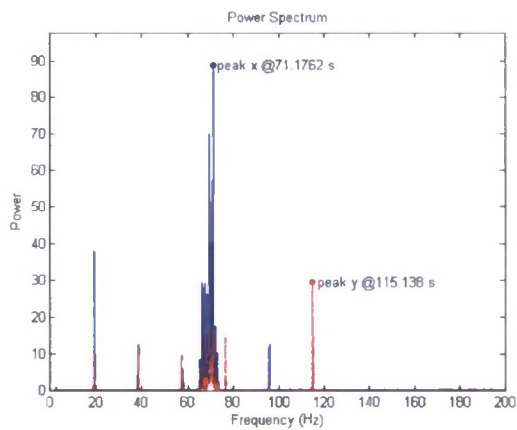
(a) 20 Hz.
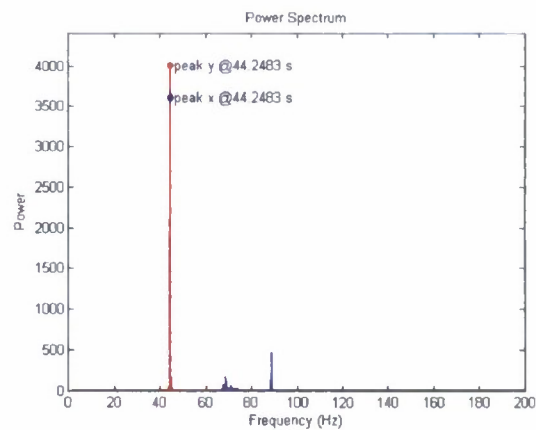
(b) 45 Hz.

Figure 19. Power spectrum for configuration 1.

The less flexible wings seem to be able to have positive lift by being able to avoid negative lift during the upstroke.

Three of the ten wing designs were then tested in a wind tunnel at a velocity of 5.2 m/s. From this data two main conclusions can be drawn. The first is that Configuration 2 of wing set 2 is the most promising of the wing designs. The second is that the higher flapping frequencies provide better lift and thrust results in a more consistent manner than the lower frequencies.

References

[1]Jones, K.D., Duggan, S.J., and Platzer, m.F., "Flapping-Wing Propulsion for a Micro Air Vehicle," Proceedings of 39th Annual Aerospace Sciences Meeting and Exhibit, Reno, Nevada, 8-11 January 2001.

[2]Tamai, M., Murphy, J.T., and Hu, H., "An Experimental Study of Flexible Membrane Airfoils at Low Reynolds Numbers", AIAA 2008-0580, 46th AIAA Aerospace Sciences Meeting and Exhibit, Reno, Nevada, 7- 10 Jan. 2008.

[3]Song, A. and Breuer, K., "Dynamics of a Compliant Membrane as Related to Mammalian Flight," AIAA 2007-68061, 45th AIAA Aerospace Sciences Meeting, Reno NV 2007.

[4]Ol, M., Parker, G., Abate, G., and Evers, J., "Flight Controls and Performance Challenges for MAVs in Complex Environments," AIAA Guidance, Navigation, and Control Conference and Exhibit, Honolulu, Hawaii, 18-21 August 2008.

[5]Viieru, D., Tang, J., Lian, Y., Liu, H., and Shyy, W., "Flapping and Flexible Wing Aerodynamics of Low Reynolds Number Flight Vehicles," 44th AIAA Aerospace Sciences Meeting and Exhibit, Reno, Nevada, 9-12 January 2006.

[6]Ellington, C.P., "The Aerodynamics of Hovering Insect Fight. I. The Quasi-steady Analysis," Philosophical Transactions of the Royal Society of London, Series B, Vol. 305, Feb. 1984, pp. 1-15.

[7]Aditya, K. and Malolan, V., "Investigation of Strouhal Number Effect on Flapping Wing Mico Air Vehicle,""45th AIAA Aerospace Sciences Meeting and Exhibit, Reno, Nevada, 8-11 January 2007.

[8]Leifer, J., Black, J.T., Smith, S.W., Ma, N., and Lumpp, N.K., "Measurement of In-Plane Motion of Thin-Film Structures Using Videogrammetry," Journal of Spacecraft and Rockets, Vol. 44, No. 6, 2007, pp. 1317-1325.

[9]Black, J.T., Pappa, R.S., "Photogrammetry and Videogrammetry Methods for Solar Sails and Other Gossamer Structures," Proceedings of 45th AIAA/ASME/ASCE/AHS/ASC Struct., Struct. Dyn. and Mater. Conference, 2004, pp. 1671-1681.

[10]Tian, X., Iriarte-Diaz, J, Middleton, K, Galvao, R, Israeli, E, Roemer, A, Sullivan, A, Song, A, Swartz S. and Breuer, K. "Direct measurements of the kinematics and dynamics of bat flight." Bioinspir. Biomim., 1 S10-S18. 2006.

[11]Johnson, E. and Jacob, J. D. "Development and Testing of a Gust/Shear Testing for NAVs and MAVs."' AIAA-2009-064, 47th AIAA Aerospace Sciences Meeting and Exhibit, Orlando, FL, 5-8 January 2009.

Part III

Gust/Shear Tunnel for NAVs

I. Goals

The overarching goal of this portion of the effort is to leverage aspects of the low Re aerodynamics in the context of fluid-structure interactions, including gusts, to design devices for controllability in such environments. The current paper presents the development and testing of a wind tunnel designed to study M/NAV flow physics. The tunnel is designed to approximate flow fields encountered by M/NAV in urban and indoor environments, where gusts and shears can have large changes in magnitude at the vehicle scale. This is particularly important on M/NAVs with flexible or flapping wings.[3] As a mission scenario, the tunnel was designed to replicate flow fields found in a typical building. Due to pressure differences, large velocity differences can exist across entrances into a building, as shown in Fig. 1a. As a baseline, entrances into OSU's Engineering North (EN) were used. Constant velocities up to 4.5 m/s are possible and these trend higher upon opening and closing of the building doors. The velocity at the indoor causeway entrance between EN and ATRC are shown in Fig. 1b. Velocities up to 3 m/s are encountered at the doorway itself decaying to 0 away from the door with gusts over 1 m/s and shears over 10 m/s/m.

(a) Gust encountered in building entrance scenario.   (b) Sample data from building causeway.
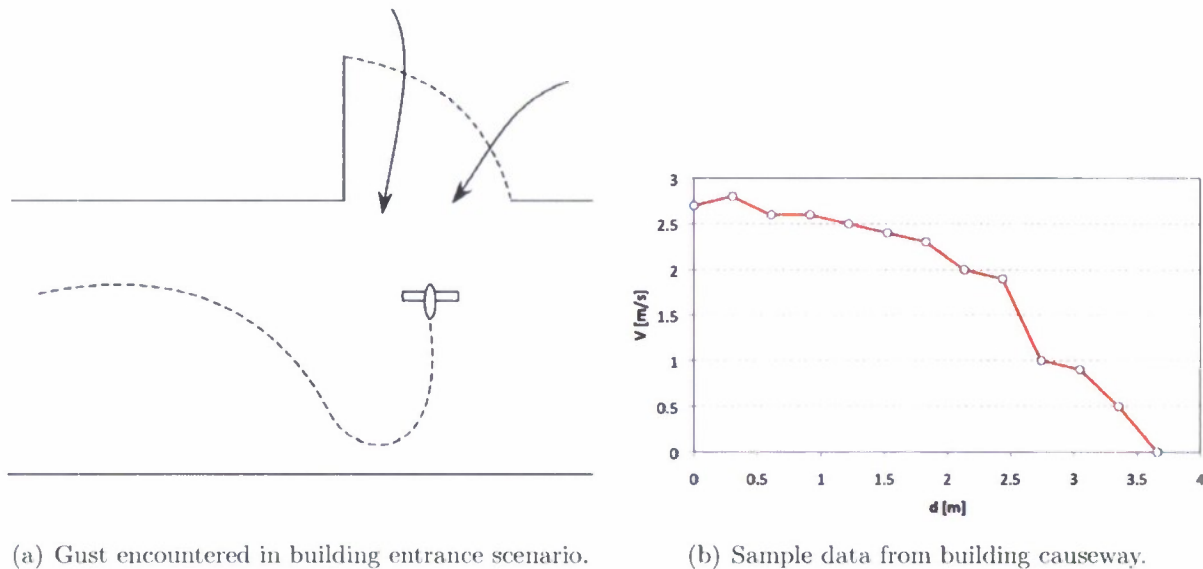
Figure 1. Flow fields encountered at the M/NAV scale..

The M/NAV gust & shear wind tunnel (GST) has been developed using a bank of computer fans that is controlled in arrays allowing both gusts and shears to be generated in the test section. The current paper investigates the development and use of the GST for the study of flight dynamics and wing deformation on micro and nano air vehicles (MAV and NAV, respectively). Topics include the tunnel design, tunnel steady and unsteady flow characteristics, comparable MAV and NAV flight environments, and sample results from testing of both fixed and flexible wing M/NAVs.

II. Background

The qualitative aerodynamic characteristics of low Re flows are vastly different than those normally seen in typical aircraft applications.[4] Mueller and DeLaurier provide an excellent review of aerodynamic issues encountered at low speeds.[5] Slight changes in the flow speed can have large effects on the flow over a given airfoil, most notably severe changes in L/D ratio. The wing shape can be specifically tailored for a certain Re, but designing for a larger range of Re will degrade performance for a specific wing velocity. Two classes of aircraft fly in the low to moderate Re range: Micro Aerial Vehicles (MAVs) and Unmanned Aerial Vehicles (UAVs or RPVs). In the former case, Re may range from $10^4 - 10^5$ and lower if hovering/loitering vehicles are considered. In the latter case, Re typically increases from 10^5 upwards to 10^6 and higher for the larger faster aircraft. Due to the nature of these vehicles, the technology described herein is well suited for MAV and UAV application inasmuch as the Re range of these vehicles fall into the current capabilities ($Re/c < 4 \cdot 10^3/\text{m}$).

Sub-scale air vehicles such as MAVs often have the disadvantage of lower lift capabilities due to reduced size but increased weight penalties due to a minimum size of control surfaces. The size limit of MAVs are typically given as less than 15 cm in maximum length.[1,3] For a standard wing planform, this gives a span of $b = 15$ cm. If a moderate aspect ratio of 4 is assumed and the vehicle is to move at a relatively slow speed, say <10 m/s, an estimate for even high lift coefficients results in lift forces on the order of 0.5 N (0.1 lbs.) or less. This weight leaves little room for equipment, let alone the vehicle structure and powerplant itself. And if the vehicle were to encounter a gust in the same direction as flight, maneuvering becomes difficult requiring an advanced control system or inherent stability. Since working NAVs have yet to be realized in the field, issues such as safety, reliability, robustness, affordability, packaging and other operational factors need to be addressed as well.

Mueller et al. addressed many issues encountered when measuring forces at low speeds, noting limitations of the facilities is the key concern.[6] Mueller also developed a low force balance for measurements at low Re and showed that reliable and accurate measurements are possible.[7] Many recent papers have examined the flow fields encountered by M/NAVs, and Ol et al. provide an excellent review of the current state-of-the-art.[8] Notable is the interest in coupling force measurements (lift and drag) with quantitative observations of the both the wake and wing surface. The latter is particular important for flexible structures. Examples at this scale are shown in Fig. 2.

There is a need to measure the impact of wind gust and shear on the performance of MAVs. Typical wind tunnels provide test data at very low turbulence levels and steady unidirectional profiles while most gust or shear tunnels are designed for the study of high
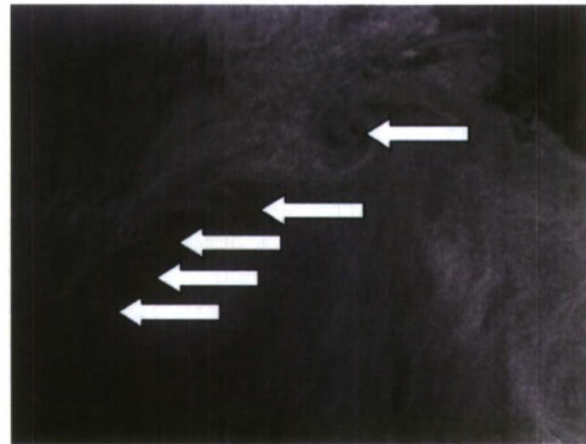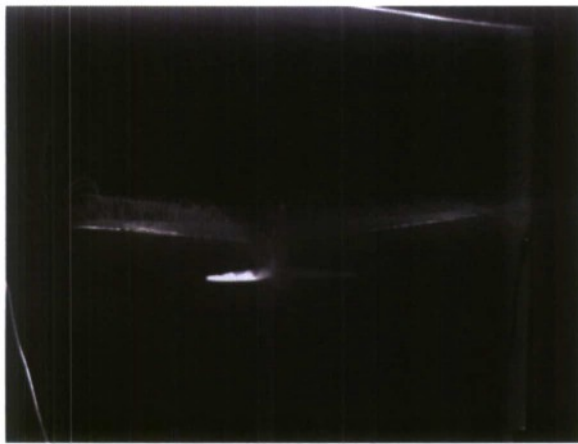
(a) Smoke wire flow visualization on fixed wing MAV.

(b) Raw PIV from flapping wing wake survey showing location of multiple wing tip vortices.

Figure 2. M/NAV flow fields.

speed effects. However, the importance of gust and shear effects on vehicle performance increases as the vehicle size and speed decrease. In particular, gust time scales become increasingly important at small scales, since the gust velocities are on the order of the vehicle flight speeds. Thus, characterization of the test section gust response times are particularly important.Since gusts can be monotonically increasing, single perturbations, or oscillatory in nature, all of these types of gust should be measured and quantified. The turbulent scales of most relevance to the control of MAV flight is on the order of the wing chord and span.[10] Production of both transverse and longitudinal gusts is highly desirable. While shears are less important, they still play a role and will be examined as well. The importance of shear effects are illustrated in Fig. 3, where both shear gradients in various terrains and energy harvesting arise as issues needing characterization. In urban environments, the decisive determinant of the vertical profile of the wind speed is the respective terrain roughness.
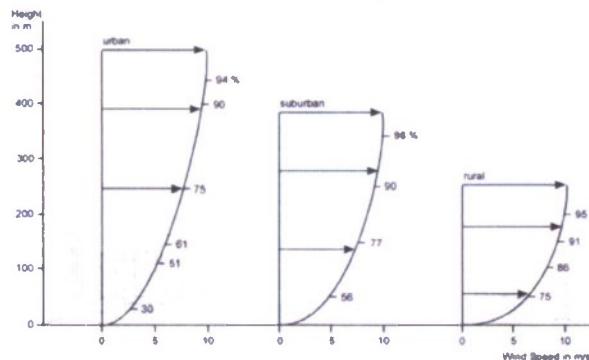
(a) Shear profiles in various terrain.[9]
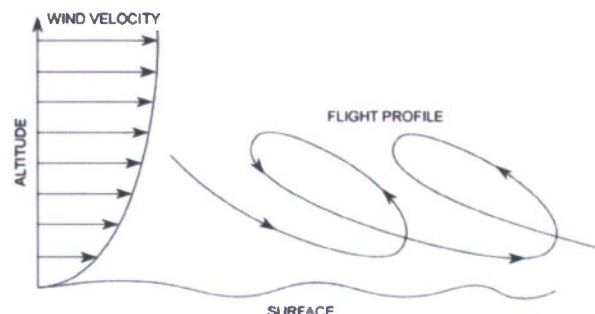
(b) Dynamic soaring.

Figure 3. Shear profiles.

Most previous gust tunnel designs have been developed at large scales to properly scale aeroelastic effects on the aircraft and great care is usually taken to replicate the amplitude and frequency of a typical gust encounter. Multiple methods have been developed, including moving the aircraft itself in relation to the surrounding flow, oscillating test section walls or the inlet section, oscillating airfoil arrays upstream of the test section and jet flaps.[11-13] Jet flaps have been found to be particularly effective due to the rapid response time allowing high frequency wave forms with different patterns.[14] However, most of these lack the ability to generate shear flows with large velocity variations across the test section while at the same time generating gusts. They are also expensive to develop.

In order to combat these issues, the gust and shear tunnel discussed herein (GST) was developed specifically for M/NAV research. The tunnel concept is based on ones developed by numerous educational groups due to its inexpensive design and large test section. Some examples are shown in Fig. 4 where tunnels of a similar design are seen at the Strategic Air Command Museum (though the exhibit was no longer in rotation at the time of this writing) and the University of Kentucky. In the current implementation, the array of computer fans is controlled in a series of banks instead of with a single input, allowing the fans to be independently controlled.

(a) SAC museum tunnel.   (b) University of Kentucky tunnel.

Figure 4.   GST progenitors.

III.   Experimental Setup

The M/NAV GST is designed from a bank of fans consisting of miniature surplus computer cooling fans. The fans used herein are Comair Rotron DC fans with a maximum input power of 6.2 W (0.52 A at 12V). Each fan is 80 mm square and the banks are arranged such that multiple rows (2 or 3) are controlled with a single voltage input. This schematic shown in Fig. 5a. While this has many disadvantages in terms of maximum velocity and response

time, the cost is very low. The current fans have 3 1/8 inch diameter blades with 42 CFM at nominal voltage, providing flow speeds sufficient for the study of vehicles at NAV and lower MAV flight speeds. The response times of these fans are limited, but the cost is low (99¢ per fan). The current fan bank with a 11x10 array arrangement is shown in Fig. 5b. This results in a test section cross section of approximately 1x1 meter. A 1 inch deep flow straightener with 1/8 inch diameter cells is placed immediately downstream of the fans. No other flow conditioners are currently used. Four Kepco RKW 12-27K programmable power supplies are used to control banks of 3, 2, 2, and 3 rows of fans. The power supplies output a a DC voltage of 12V with a 5V input, or 14V at 6V, and have a 1 ms response time. The fan bank power supply input voltages are controlled by a NI USB-6265 data acquisition unit and a LabVIEW program shown in Fig. 6. The tunnel has a maximum velocity of 5 m/s with a sensitivity of 0.42 m/s/V with no flow straightener and slightly less when the straightener is present. The tunnel calibration with the fan input signal is shown in Fig. 7a.
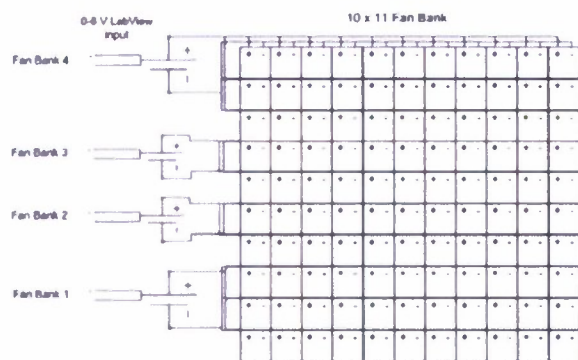
(a) Fan bank schematic.

(b) Fan bank.

Figure 5. GST fan bank.
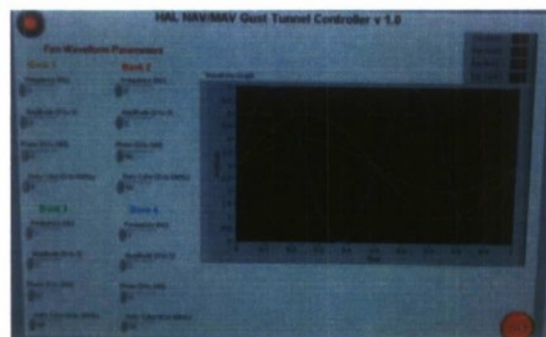
Figure 6. GST control panel.

Hot-wire measurements are made using a single component Auspex 5 micron diameter

hot-wire connected to a Dantec MiniCTA. Data was sampled using the NI DAQ system discussed above at 10 kHz. The hot-wire calibration and comparison with two separate turbometers is shown in Fig. 7e.

(a) Fan calibration (without straightener).

(b) Probe comparison (with straightener).
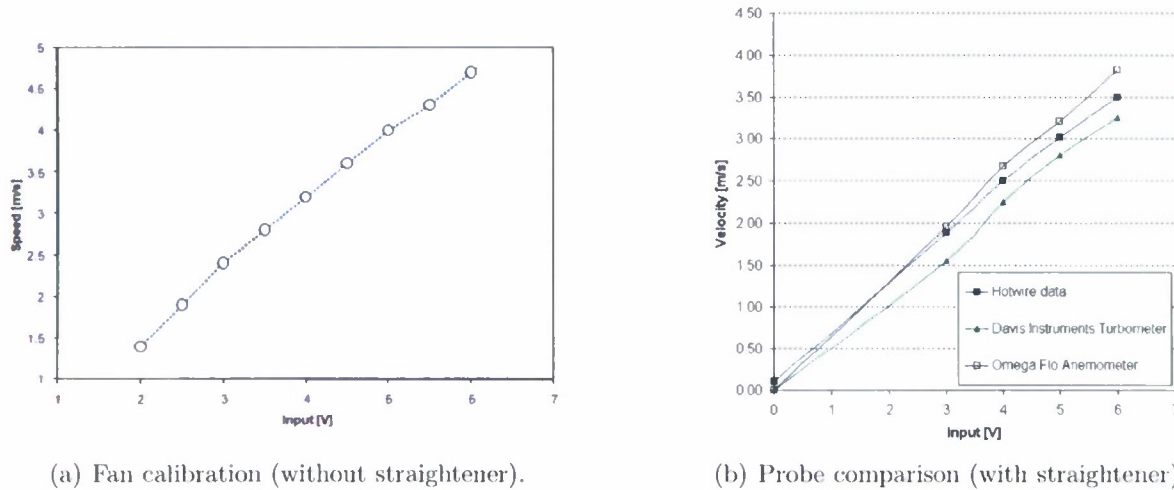
Figure 7. Experimental arrangements.

For PIV measurements, the flow is seeded with smoke particles on the order of 1 micron in diameter. A 2-D light sheet is projected in the vertical plane using a Big Sky Nd:YAG laser.A Quantum Composer 9518+ pulse generator is used to time the lasers in synchronization with a Redlake Megaplus CCD camera. The vertical field of view is approximately 10 cm with a resolution of 100 pixels/cm. Epix frame grabbing hardware and software is used to acquire binary image pairs. For each run, 196 image pairs were captured at a rate of approximately 15 Hz and these images were processed using the algorithm described below. The velocity and vorticity fields obtained in post-processing were then averaged over the data set. The PIV algorithm utilizes the wall adaptive Lagrangian particle-tracking algorithm (WaLPT) developed by Sholl and Savaş.[15] This algorithm treats the seeding as fluid particles and determines their translations and deformations. Fluid parcels registered by CCD pixels are advected with individually estimated velocities and total accelerations. A standard DPIV algorithm is employed to determine the initial velocity field, and the routines in WaLPT allow for highly accurate measurement of the velocities near surfaces by mirroring the flow about the wall using an image parity exchange routine.[16] Velocity and vorticity are calculated as part of the PIV algorithm and scaled accordingly; vorticity is determined spectrally and does not suffer from typical numerical differentiation problems.

A KineOptics Wind Tunnel Balance (WTB) 2.0 is used to measure lift and drag. This balance equips two Sensotec Model 11 250 gram load cells. The ends of each of the directional units has a flexure which is designed to transfer the loads to the load cells and special magnetic rods are attached to the flexures at one end and the load cells at the other. If

too much force is applied, the rods are designed to separate from the load cell to prevent an overload on the cell. Fig. 8a shows a model mounted on the balance system. The signal from the load cells was then run through a difference amplifier and the ouput to LabVIEW and recorded at a sampling rate of at least 5000 Hz. Data analysis was handled primarily in MATLAB and Excel. For flapping and flexible wing observations, two MotionPro X high speed cameras are available with frame rates up to 1000 Hz and a resolution of 1280x1024. The cameras are synched to the balance via a trigger signal sent by LabVIEW. These can also be used to track positions of models in free flight (Fig. 8b).

(a) Model on lift and drag balance.

(b) Model in free flight.
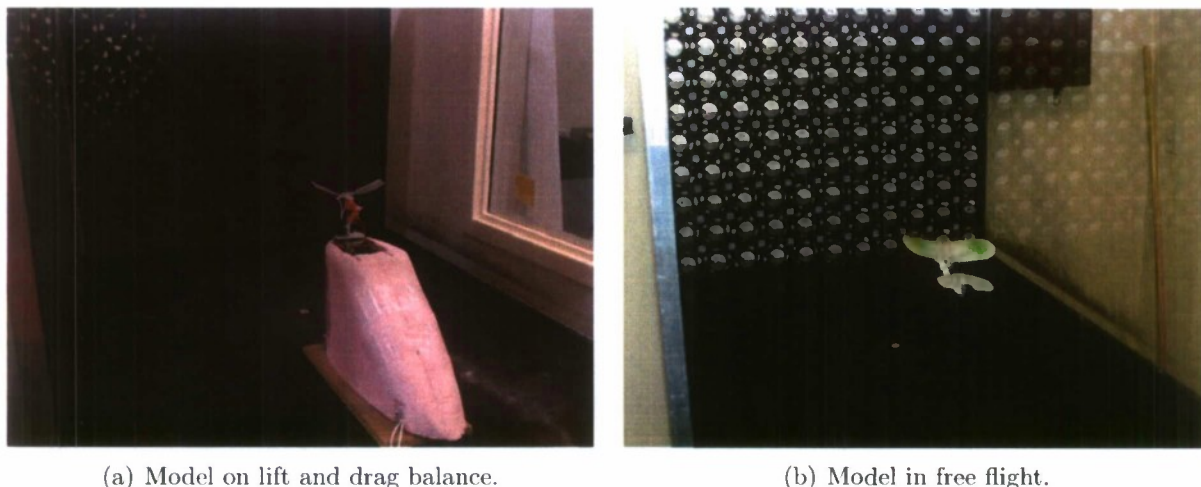
Figure 8. Models in GST.

IV. Results

The impact of the flow straightener on the tunnel flow is shown in Fig. 9. Fig. 9a shows the contour with no straightener, which results in a region of faster flow near the bottom of the tunnel with a large shear region near the top of the tunnel. The addition of the straightener as shown in Fig. 9b provides a more uniform flow but shifts the boundary region to the bottom of the tunnel. Thus, the addition of the straightener provides some improvement, but can be disregarded in many cases if necessary.

Characterization of the tunnel results are shown starting in Fig. 10. Each plot shows the fan bank input signal with the tunnel response using the hot-wire mounted in the tunnel center. Ramp response is shown in Fig. 10a where an input rate of 2 V/s ramps the input signal from 0 to 6 V in 3 seconds. This rate provides the maximum tunnel response time from quiescent flow to maximum velocity and shows the effect of various transient inputs on the tunnel test section velocity. Fig. 10b shows the comparable decay when the tunnel is running at maximum velocity and input is turned off. Note that the DC motors do not
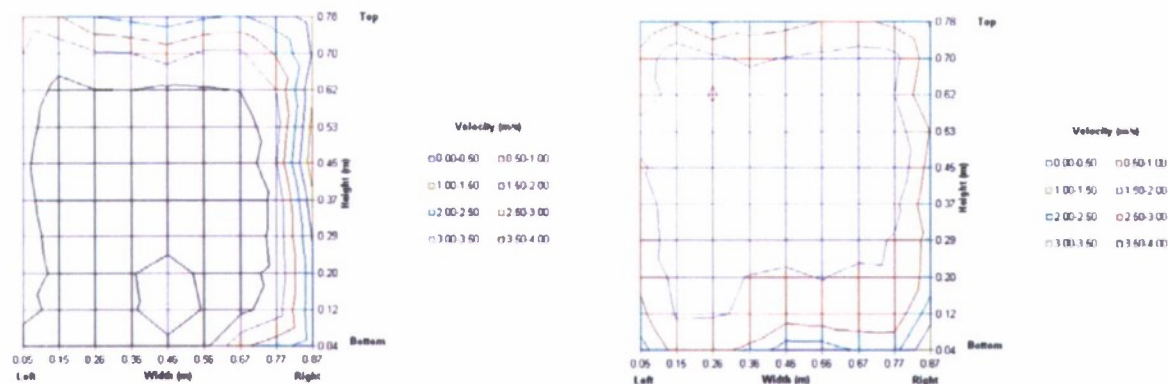
(a) Without straightener.　　　(b) With straightener.

Figure 9.　Effect of flow straightener.

brake hence do not respond rapidly in the negative direction. It takes approximately 14 s for the tunnel to decay to a quiescent level. Fig. 11 shows sample time responses of the tunnel to a gust input. Starting at a 3V input signal, an input pulse up to the maximum of 6V is applied for a set period then returning to 3V. Figs. 10 and 11 have incorrect formulas yielding slightly higher velocity values. However, compared with recent test data they also are higher because of no flow straightner in those tests.
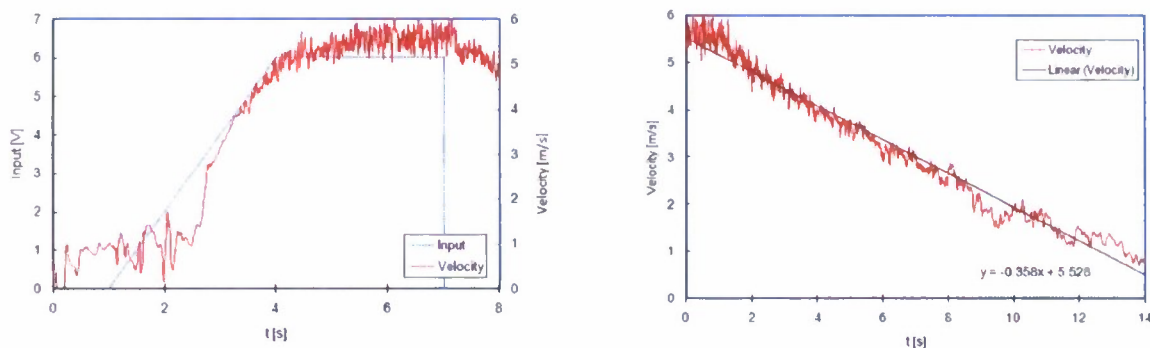
(a) Three-second ramp　　　(b) Decay from maximum output

Figure 10.　Ramp and decay response.

Figs. 12 through 15 show the tunnel response to various sharp edged gust inputs. Fig. 12a shows the tunnel response to a gust starting at 0 input and with a maximum 6V input peak applied for 0.5 s (0-6-0). Note that the maximum tunnel velocity is not reached and the decay time is longer than the time domain shown. Likewise, Fig. 12b repeats this run but for a 1 s duration gust. A peak velocity of 2.5 m/s is reach just after the gust is tuned off. Fig. 12c and 12d repeat this for 2 and 4 s, respectively. Fig. 12c shows that the peak
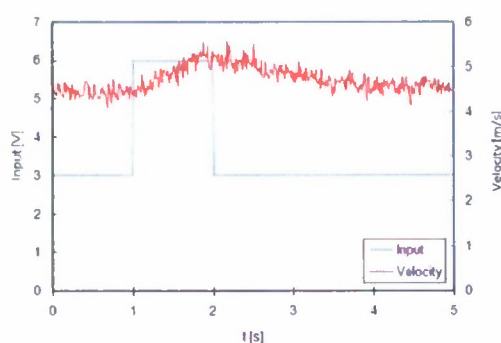
(a) 1 second pulse up.
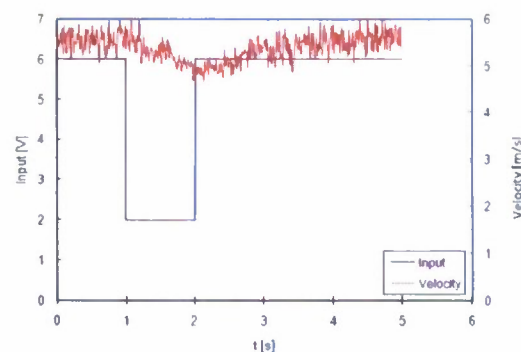
(b) 1 second pulse down.
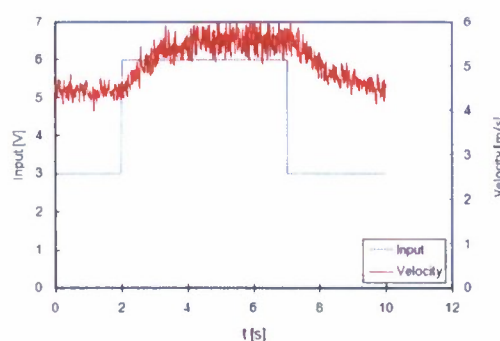
(c) 5 second pulse up.

Figure 11. Sample time response.

velocity is reached just prior to removal of the gust input. Fig. 13 repeats this procedure but for a gust with 3-6-3 top-hat profile. Similar results are achieved. Fig. 14 and 15 examine negative longitudinal gusts with the same gust duration with amplitudes of 6-0-6 and 6-3-6, respectively. In the 6-0-6 case, the gust velocity is not reached in any of the cases, due to the long decay time, but the 6-3-6 reaches the desired gust velocity after approximately 1.5 s as seen in Fig. 15c.

Figs. 16 through 19 show the tunnel response to various ramp gust inputs. Ramp times range from .38 s to 3 s and are repeated for the 0-6-0, 3-6-3, 6-0-6, and 6-3-6 input amplitudes. Note that in all cases, the gust amplitude is reached between 1.5 and 3 s except in the 6-0-6 case (Fig. 18d).

Fig. 20 shows results for coupled fan banks for generating shear profiles while Fig. 21 shows shear profiles for 10 different input cases. Measurements were made using a turbometer fixed in the tunnel center and moved vertically. In Fig. 20, the banks are either on (5V input) or off (0V input). Banks are either driven independently (Fig. 20a), in pairs of two (Fig. 20b), in isolated pairs (Fig. 20c), or in triplets (Fig. 20d). It can be observed

that a wide range of distinct shear flows are possible. Note that in some cases, the flow is reversed at the test location. Allowing the banks to vary continuously from 0-5V increases the range substantially. Some of these possible shears are shown in Fig. 21, where banks are allowed to have constant input values from anywhere between 0 and 6V. The most linear shear (Fig. 21c) is acheived by using non-linear fan input values of 5-6-4-3. All other shears exhibit non-monotonic behavior and are characterized by a distinct peak away from the tunnel wall. In all cases, the maximum shear achieved is approximately 25 m/s/m.

Complex flow fields can be generated by independently controlling the fan banks with different frequencies. Frequency input can be determined via Fourier transform and the resulting sinusoidal input signals fed into the fan banks. Two samples are shown in Fig. 22, one with a higher frequency than the other. While the lower frequency results in a higher mean velocity, it also generates larger scale (temporal and spatial) gusts. Thus, given enough banks, arbitrary flow fields can be generated from user data.

PIV results are shown in Figs. 23 and 24. In Fig. 23, the background velocity for a 10 cm x 10 cm area is shown for a 5V input (approximately 4 m/s). An instantaneous velocity fields is shown in Fig. 23a and the average velocity field is shown in Fig. 23b. RMS velocity and velocity magnitude are shown in Fig. 23c and Fig. 23d, respectively. The typical velocity fluctuations are on the order of 20 cm/s or approximately 5% of the mean flow. Results for a toy MAV are shown in Fig. 24. The vehicle is a remote control biplane model with a span of 21 cm and MAC of approximately 5.5 cm and a pusher propeller with a diameter of 6.5 cm. The total vehicle mass is 6.40 g. The vehicle is mounted at an angle of attack of approximately 10°. The plots show the instantaneous and average velocity fields, respectively, of the wake vortex 26 cm behind the starboard wing. In Fig. 24a, both of the vortex from the upper and lower wing are clearly visible. The merger is unsteady and on average a single vortex is seen (Fig. 24b). The tip vortex from the tail is clearly seen in the lower left corner of the plot. In both cases, note the wake vortex dominates over the background flow. Fig. 25 shows lift and drag data from the same model using the tunnel balance with first a ramp flow (0 to 3 s) and then two 1 s gusts separated by 7 s. Velocity is measured using hot-wire. Lift tracks the gusts while the drag, while reactive, is not as responsive to the gust input.

V.   Summary

A simple gust/shear tunnel was constructed of multiple independently controlled fan banks and examined for use in testing M/NAVs. Tunnel characteristics are presented for both gust and shear flows and sample data for typical MAVs is presented. While the individual gust responses are low, these can be supplemented by combing multiple frequencies to produce high frequency flow fields with small spatial scales. Some of the advantages of

the tunnel include

- Low cost

- Simple construction

- Reconfigurable design

- Arbitrary wave form

- Multiple phases between banks

- Uniform flow capability

However, in the current incarnation, there are numerous disadvantages. These include

- Fan frequency response $< \mathcal{O}(1 \text{ Hz})$

- High turbulence $\mathcal{O}(1\text{-}5\%)$

- Smallest spatial scale limited to fan size for uniform gusts

Improvements to the design include the use of more fan banks. This requires more independent power supplies and output channels, but is conceptually possible down to individual fans. Faster response fans such as servo motor driven fans would improve the gust response time, but would also increase the tunnel cost. However, this would result in more realistic flow fields. In the future, we will also be investigating the impact of turbulence damping screens on the flow field.

References

[1]McMichael, J. M. and Francis, M. S. "Micro Air Vehicles - Toward a New Dimension in Flight," DARPA, 1997.

[2]DARPA BAA06-06 PIP, Nano Air Vehicle Program, 2006.

[3]Shyy, W. and Smith, R. "A Study of Flexible Airfoil Aerodynamics with Application to Micro Aerial Vehicles," AIAA 97-1933, *28th AIAA Fluid Dynamics Conference*, June, 1997.

[4]Mueller, T. J. (ed.), *Low Reynolds Number Aerodynamics*, Springer-Verlag, New York, 1989.

[5]Mueller, T. J. and DeLaurier, J. D. "Aerodynamics of Small Vehicles," *Annual Review of Fluid Mechanics*, Vol. 35, Jan. 2003, pp. 89–111.

[6]Mueller, T. J., Batill, S., Brendel, M, Perry, M., Bloch, D., Huber, A., Bastedo, W., O'Meara, M., and Schmidt, G. "Low Reynolds Number Wind Tunnel Measurements: The Importance of Being Earnest," *Aerdynamics at Low Reynolds Numbers*, October 15-18, 1986.

[7]Mueller, T. J. "Aerodynamic Measurements at Low Reynolds Numbers for Fixed Wing Micro-Air Vehicles," *Development and Operation of UAVs for Military and Civil Applications*, VKI, Belgium, September 13-17, 1999.

[8]Ol, M., Parker, G., Abate, G., and Evers, J. "Flight Controls and Performance Challenges for MAVs in Complex Environments," AIAA-2008-6508, AIAA Guidance, Navigation and Control Conference and Exhibit, Honolulu, Hawaii, August 18-21, 2008.

[9]Baumbach, G. 1991, *http://www.stadtentwicklung.berlin.de/umwelt/umweltatlas/ed403_01.htm*, retrieved June 4, 2008.

[10]Milbank, J., Loxton, B., Watkins, S., and Melbourne, W.H., "Replication of Atmospheric Conditions for the Purpose of Testing MAVs – MAV Flight Environment Project: Final Report," USAF Project No: AOARD 05-4075, 2005.

[11]Mitchell, C.G.B., "Assessment of the Accuracy of Gust Response Calculations by Comparison with Experiments," *Journal of Aircraft*, Vol. 7, March 1970, pp. 117-125.

[12]Gilman, J. Jr. and Bennett, R. M., "A Wind Tunnel Technique for Measuring Frequency Response Functions for Gust Load Analyses," *Journal of Aircraft*, Vol. 3, June 1966, pp. 535–540.

[13]Barlow, J. B., Rae, W. H., and Pope, A. "Low-Speed Wind Tunnel Testing," Wiley-Interscience, 3rd ed., 1999.

[14]Viets, H., Ball, M., and Piatt, M. "Experiments in a Subscale Pilot Gust Tunnel," *AIAA J.*, Vol. 19, No. 6, pp. 820–824, 1981.

[15]Sholl, M. and Savaş, Ö., "A Fast Lagrangian PIV Method for Study of General High-Gradient Flows," AIAA Paper 1997–0493, 35th AIAA Aerospace Sciences Meeting, Reno, NV, Jan. 1997.

[16]Tsnei, L. and Savaş, Ö. "Treatment of Interfaces in Particle Image Velocimetry." *Experiments in Fluids*, **29**, pp. 203–214, 2000.

(a) 0.5 sec   (b) 1 sec   (c) 2 sec   (d) 4 sec
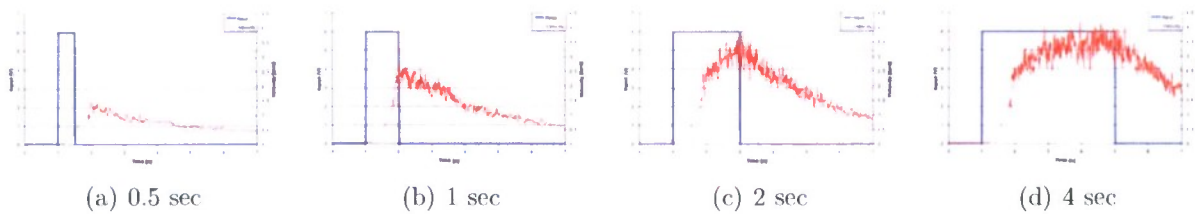
Figure 12. Variable gust for 0,6,0 V input.

(a) 0.5 sec   (b) 1 sec   (c) 2 scc   (d) 4 sec
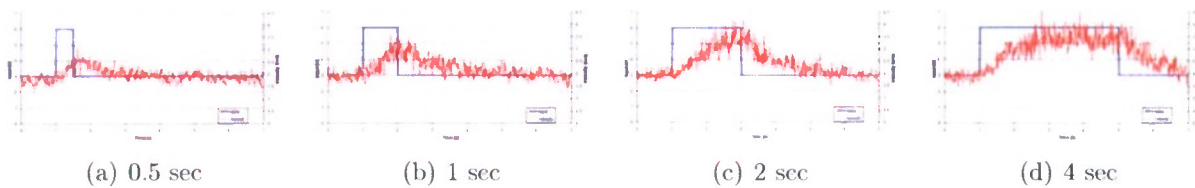
Figure 13. Variable gust for 3,6,3 V input.

(a) 0.5 scc   (b) 1 sec   (c) 2 sec   (d) 4 sec
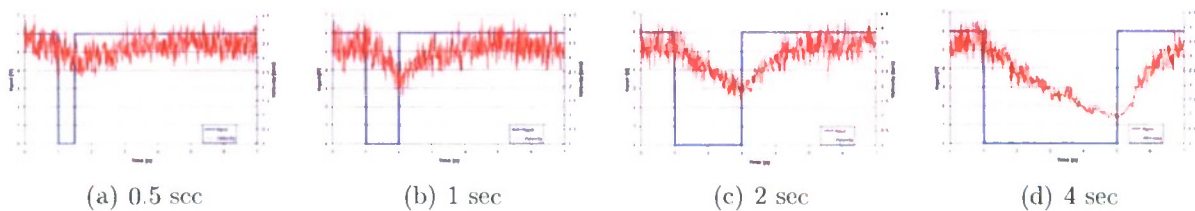
Figure 14. Variable gust for 6,0,6 V input.

(a) 0.5 sec   (b) 1 sec   (c) 2 sec   (d) 4 sec
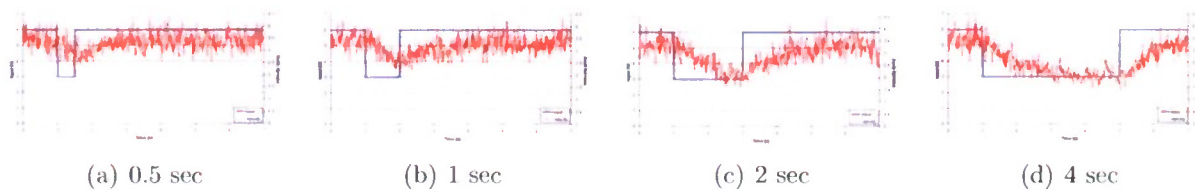
Figure 15. Variable gust for 6,3,6 V input.

(a) 0.38 sec   (b) 0.75 scc   (c) 1.5 sec   (d) 3 sec
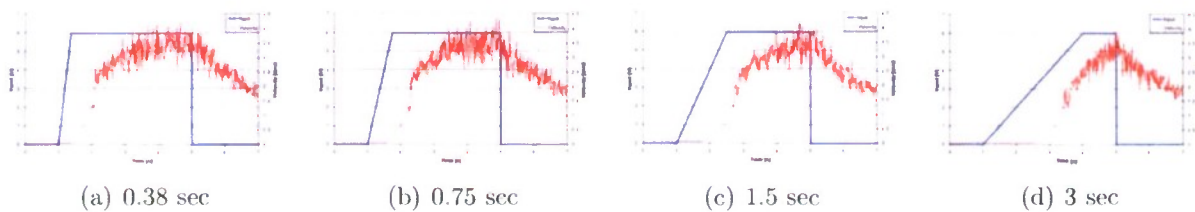
Figure 16. Variable ramps for 0,6,0 V input.

(a) 0.38 sec   (b) 0.75 sec   (c) 1.5 sec   (d) 3 sec
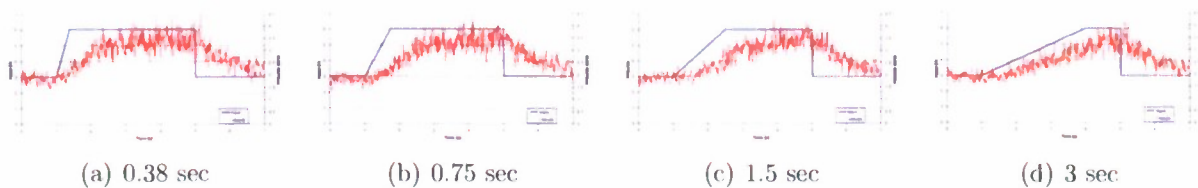
Figure 17. Variable ramps for 3,6,3 V input.

(a) 0.38 sec   (b) 0.75 sec   (c) 1.5 sec   (d) 3 sec
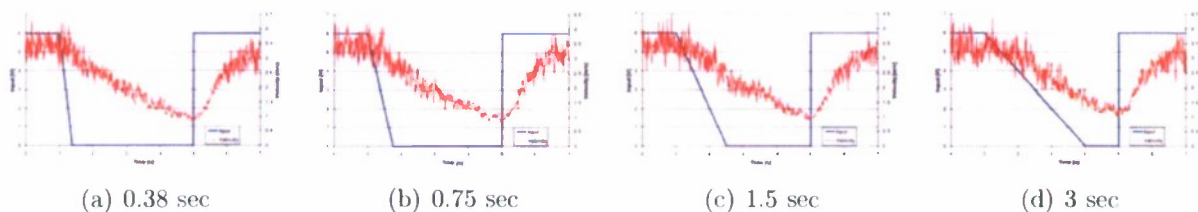
Figure 18. Variable ramps for 6,0,6 V input.

(a) 0.38 sec   (b) 0.75 sec   (c) 1.5 sec   (d) 3 sec
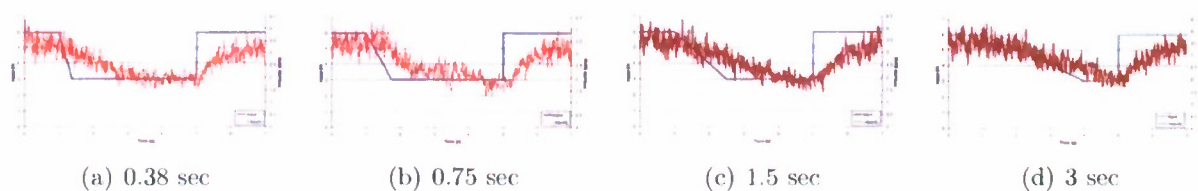
Figure 19. Variable ramps for 6,3,6 V input.

(a) Single Banks   (b) Coupled Banks   (c) Isolated Pairs   (d) Triple Banks
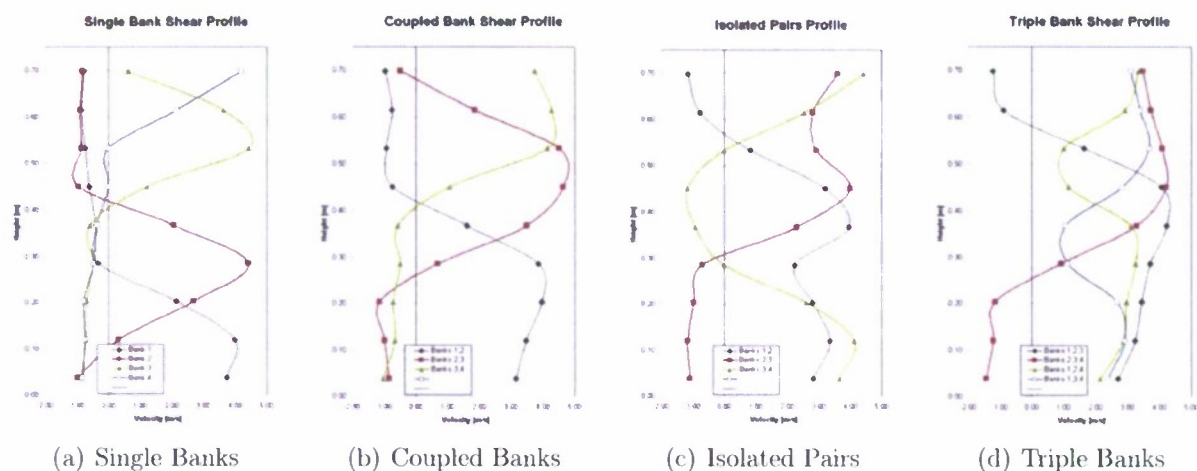
Figure 20. Multiple shears profiles for varying 0,5 V input.
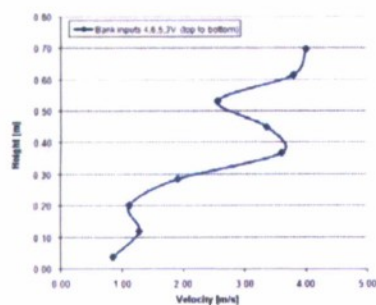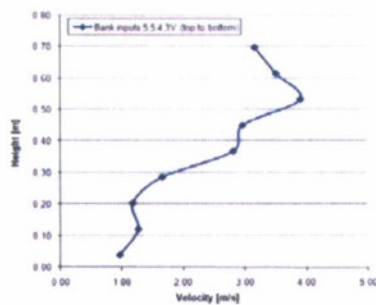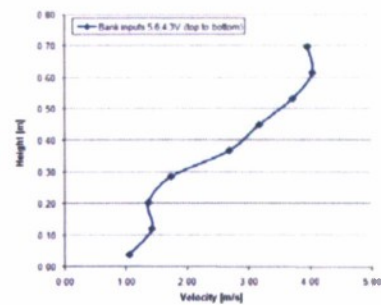
(a) Case 1   (b) Case 2   (c) Case 3
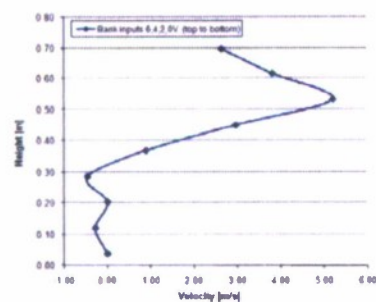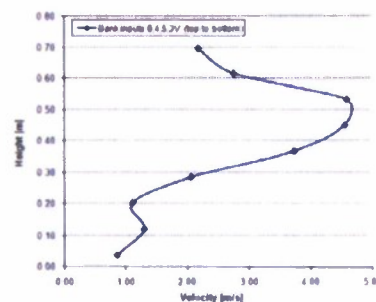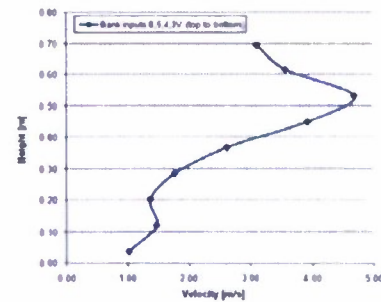
(d) Case 4   (e) Case 5   (f) Case 6
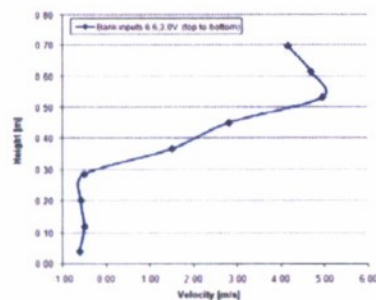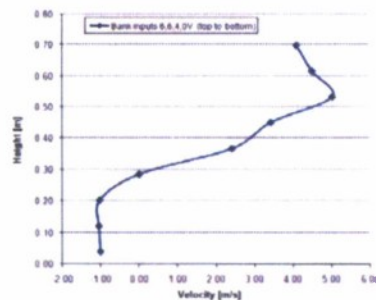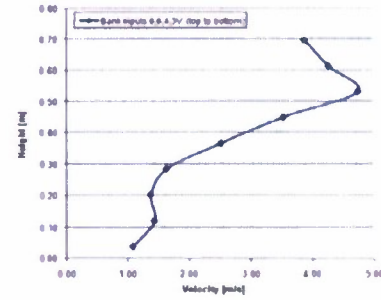
(g) Case 7   (h) Case 8   (i) Case 9
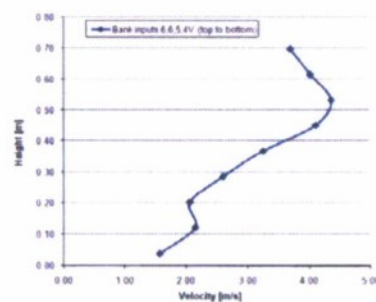
(j) Case 10

Figure 21. Shear profile simulation.
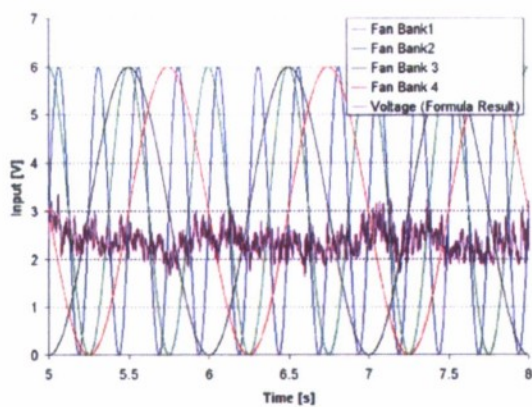
(a) Variable frequency input, high frequency.
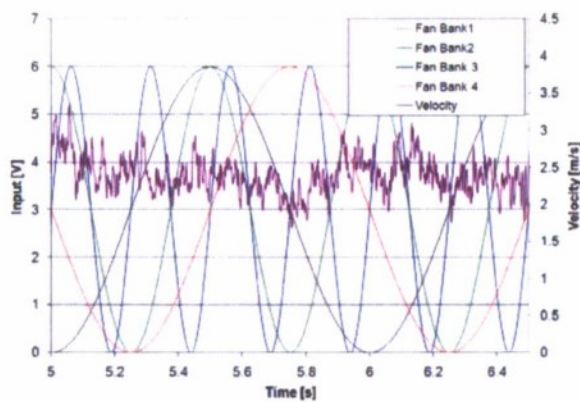
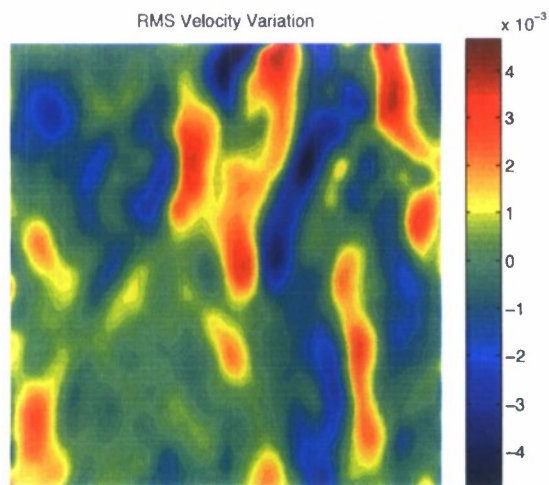(b) Variable frequency input, low frequency.

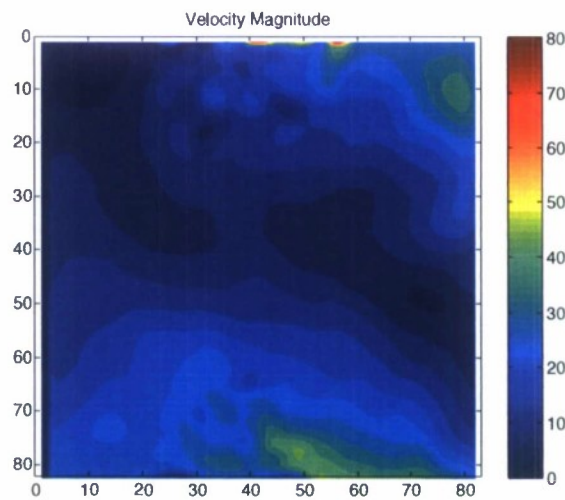Figure 22. Variable frequency input and generation of complex flow fields.
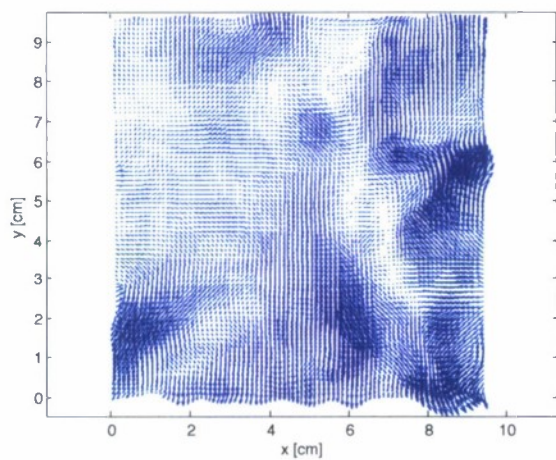
(a) Instantaneous velocity.
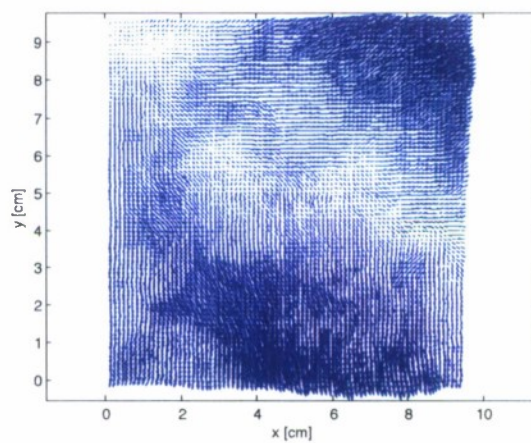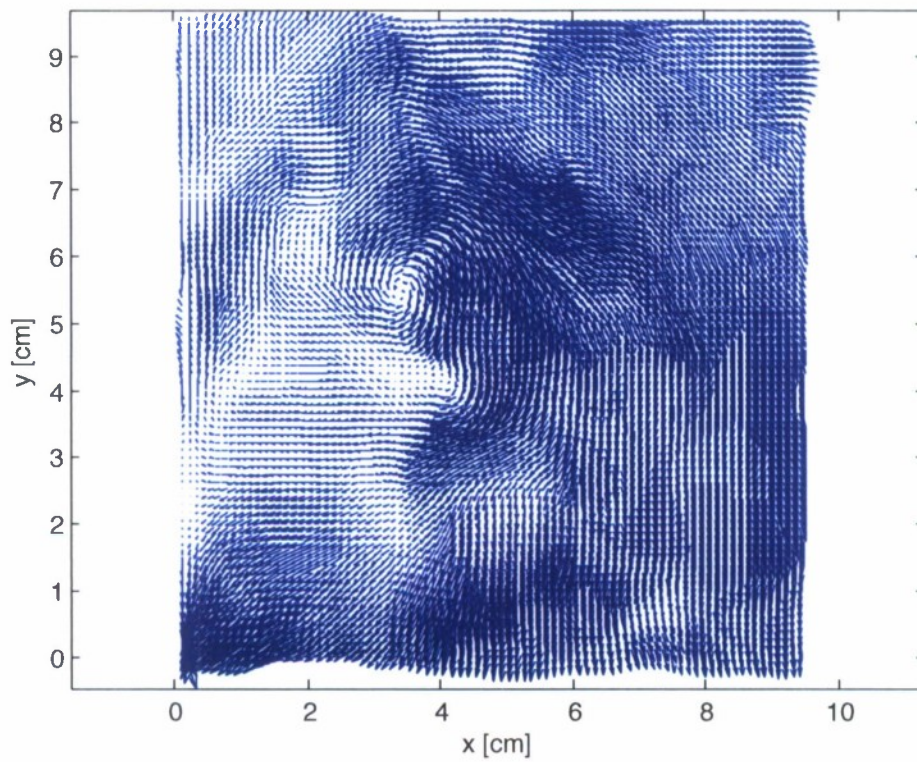

(b) Median velocity.
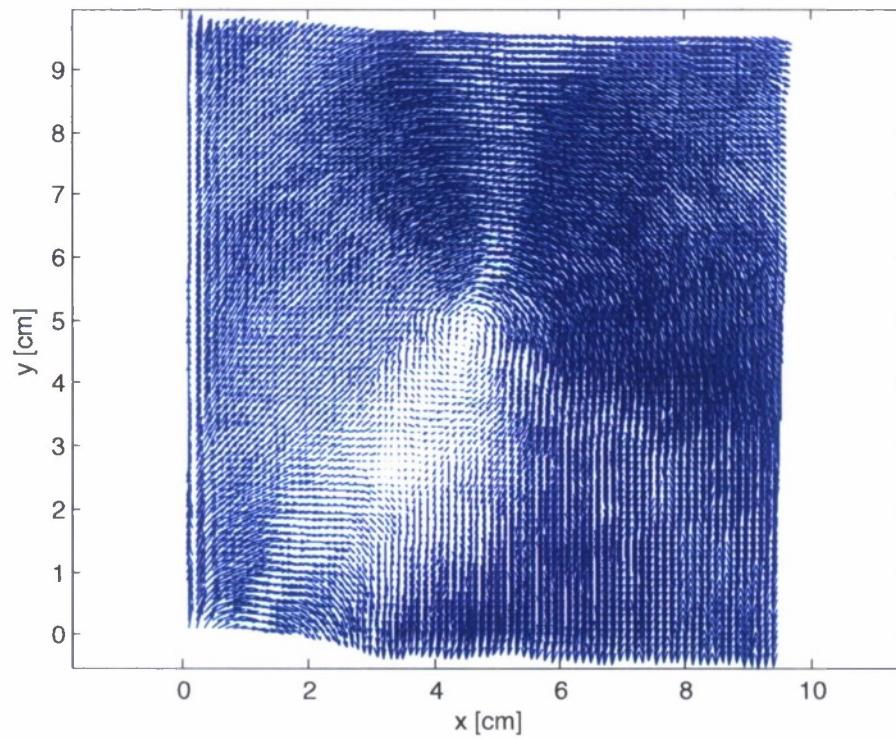

(e) RMS velocity.

(d) Velocity magnitude.

Figure 23. Background field.

(a) Instantaneous velocity.
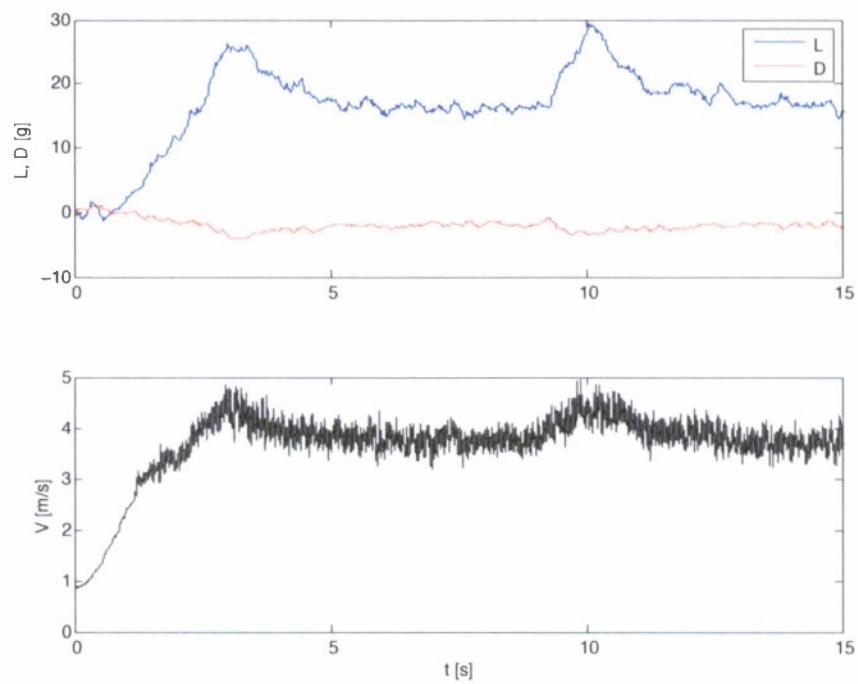

(b) Median velocity.

Figure 24. Tip vortex of MAV biplane.

Figure 25. Lift and drag data of MAV model.